INFORMATION TO USERS

This manuscript has been reproduced from the microfilm master. UMI films the text directly from the original or copy submitted. Thus, some thesis and dissertation copies are in typewriter face, while others may be from any type of computer printer.

The quality of this reproduction is dependent upon the quality of the copy submitted. Broken or indistinct print, colored or poor quality illustrations and photographs, print bleedthrough, substandard margins, and improper alignment can adversely affect reproduction.

In the unlikely event that the author did not send UMI a complete manuscript and there are missing pages, these will be noted. Also, if unauthorized copyright material had to be removed, a note will indicate the deletion.

Oversize materials (e.g., maps, drawings, charts) are reproduced by sectioning the original, beginning at the upper left-hand corner and continuing from left to right in equal sections with small overlaps. Each original is also photographed in one exposure and is included in reduced form at the back of the book.

Photographs included in the original manuscript have been reproduced xerographically in this copy. Higher quality 6" x 9" black and white photographic prints are available for any photographs or illustrations appearing in this copy for an additional charge. Contact UMI directly to order.

UMI

A Bell & Howell Information Company
300 North Zeeb Road, Ann Arbor MI 48106-1346 USA
313/761-4700 800/521-0600

Université d'Ottawa • University of Ottawa

Physical Optics Analysis of Electrically Small Slot-Fed Substrate Lens Antennas

by

Joey R. Bray, B.A.Sc.

A thesis submitted to the
School of Graduate Studies and Research
in partial fulfillment of the requirements for the degree of

Master of Applied Science
in Electrical Engineering

Ottawa-Carleton Institute for Electrical and Computer Engineering
School of Information Technology and Engineering
Faculty of Engineering
University of Ottawa

May 1998

ABSTRACT

With the current explosion of microwave wireless communication systems comes the need to produce low cost miniaturized components. Integrated antennas, such as planar microstrip-fed patches and slots, are a promising means of combining the antenna function with the associated transceiver circuitry. However, these antennas suffer from a bi-directional radiation pattern, power loss via substrate modes, a broad radiation pattern, or a combination of the above. To correct these problems, a dielectric lens of hemispherical shape, or slight variation thereof, can be placed directly upon the planar antenna, forming what is called a Substrate Lens Antenna (SLA). At sub-millimeter-wave frequencies, a SLA becomes unattractive because its diameter is typically larger than a free-space wavelength. Such lenses become heavy, bulky and expensive as the operating frequency is reduced. This thesis investigates electrically small, slot antenna fed, SLAs operating at 10 GHz in an attempt to facilitate the integration of these devices.

This work begins by summarizing the current state of SLA technology. Various feed antennas and substrate lens geometries are reviewed, along with the latest SLA simulation techniques. It is shown that a ray optics approach is the most popular technique for simulating electrically large SLAs.

Analytical issues concerning the use of electrically small lenses are then considered. Of primary concern is the effect of placing the lens inside the near-field region of the slot antenna: an issue that is never a factor when electrically large lenses are used. Another concern is the validity of the ray approximation that is commonly used in SLA analysis. With these issues in mind, several analysis methods are evaluated as candidates for an improved simulation technique. After selecting the hybrid Physical Optics (PO) technique, this newly developed simulator is used to predict the radiation performance of electrically small SLAs. The limitations of this improved simulator are also examined.

An experimental study is conducted to gather empirical data on slot-fed SLAs at 10 GHz. A microstrip coupled slot antenna is designed to serve as the feed antenna for several lenses of decreasing electrical length. Impedance and radiation pattern measurements of these SLAs are then conducted and the latter are compared to the simulator's predicted patterns. Reasonable agreement is found between the two but discrepancies are found to exist between the measured SLA input impedance and the theory that governs it. It is concluded that electrically small SLAs demonstrate improved radiation characteristics over simple slot radiation and that the hybrid PO simulation performs well. A more exhaustive study of electrically small SLA input impedance is recommended as future work to allow the full characterisation of these radiators.

Acknowledgments

I wish to express my sincerest gratitude to my thesis supervisor, Prof. Langis Roy, for his guidance, assistance and support during my Master's degree studies at the University of Ottawa.

I gratefully acknowledge the Natural Sciences and Engineering Research Council of Canada, the University of Ottawa, and Dr. L. Roy for providing the financial support for this work.

I wish to sincerely thank Dr. A. Attipiboon, from the Communications Research Centre, for his encouraging words and helpful initial discussions. Many thanks are extended to Mr. D. Roscoe, formerly of the CRC, for his helpful discussions and for overseeing the manufacturing of the dielectric lenses and slot antennas. Much appreciation is expressed towards Dr. P. Berini at the University of Ottawa for his technical expertise and for our fruitful discussions. I would further like to thank Mr. A. LeHénaff at the University of Ottawa for his time and efforts throughout the measurements stage of this work.

Kudos go out to my colleagues for their camaraderie, good humour and assistance along the way. Many thanks to: Ms. A. Blais, Mr. D. Cayer, Mr. G. Kongara, Ms. K. Lévis, Mr. L. Nguyen, Mr. M. Ouellette, Mr. W. Robbins, Mr. V. Stratton, and Ms. X. Tian. And of course, I would like to express a special thank you to Elaine Bailey for her kindness, understanding and support.

It is with the deepest gratitude that I thank the members of my family, who have been dearly missed throughout these years, for their unwavering and continued support of my endeavours.

Dedicated to my parents, Joanne and Robert, and to my sister Lisa.

Table of Contents

1. Introduction 1

1.1 Background 1

1.2 Thesis Objectives and Motivation 3

1.3 Thesis Contribution 5

1.4 Thesis Organisation 5

2. Review of Substrate Lens Antenna and Dielectric Resonator Antenna Technology 7

2.1 Planar Antennas on Dielectric Substrates 7

2.2 Substrate Lenses - Background 10

2.3 A Review of Dielectric Resonator Antennas 17

3. Analysis Methods 20

3.1 Existing Analysis Methods for SLAs 20

3.2 Limitations of the Hybrid GO Analysis Method and Improvements 21

3.3 Propagator Candidates 22

3.3.1 Fourier Optics: A Scalar Wave Theory 22

3.3.2 Spectral Domain Method 25

3.3.2.1 Fourier Optics - A Special Case of the Spectral Domain Method 27

3.3.3 Physical Optics Method 27

3.3.4 Moment Method Solutions for DRAs 29

3.4 Propagator Selection 31

4. Physical Optics Hybrid Simulation Technique 33

4.1 Physical Optics Derivation of the Free-Space Dyadic Green's Functions 33

4.2 Hybrid Analysis Using PO Illumination 36

4.3 Limitations of the Hybrid Analysis 38

4.4 Slot Currents 39

4.5 Minimum Lens Radius Analysis 40

4.5.1 Validity of the Fresnel Equations 41

4.5.2 Wave Vector Direction Ambiguity 41

4.5.3 First Test Case 42

4.5.4 Second Test Case 43

4.5.5 Comparative Results 54

4.5.6 Conclusion - Range of Validity 56

5. Simulation Results 57

5.1 Comparison Between Closed-Form and Physical Optics Lens Illuminations for a Double-Slot Array 57

5.2 Validation of the Hybrid Simulation Technique 60

5.3 Comparison Between the Radiation Patterns of Double Slot-Fed SLAs that are Illuminated by Closed-Form Equations and Physical Optics 61

5.4 Comparison Between the Radiation Patterns of Single Slot-Fed SLAs that are Illuminated by Closed-Form Equations and Physical Optics 63

5.5 Directivity of Single Slot-Fed Lenses 65

5.6 Reflection Loss Analysis 68

5.7 First Reflection Effects 77

5.8 Simulation Results - Conclusion 88

6. Experimental Design and Measurements 89

6.1 Feed Antenna Design 89

6.1.1 Design of the Free-Space Slot Antenna 89

6.1.2 Design of the Scaled Slot Feed Antenna 96

6.2 Lens Design and Test Jig Design 100

6.2.1 Lens Design 100

6.2.2 Test Jig Design 102

6.3 Free-Space Slot Measurements 104

6.4 Radiation Pattern Perturbation of the Lens Holders 106

6.5 Substrate Lens Antenna Measurements 107

6.5.1 Self-Impedance De-embedding of the Free-Space Slot (Reverse Modeling) 109

6.5.2 Slot Lens Antenna Radiation Patterns 113

6.6 SLA Measurements Conclusion 121

6.6.1 Impedance 121

6.6.2 Front to Back Ratios (F/B) 121

6.6.3 Pattern Directivity 122

7. Thesis Summary and Future Work 124

8. Appendix A: Fourier Optics Related to the Spectral Domain Method 128

9. Appendix B: Physical Optics Derivations 131

10. Appendix C: Paraxial Approximation of the Far-Field 137

11. Appendix D: Shifting the Impedance Reference Plane 140

12. References 141

List of Figures

Figure 1: Ray Approximation of Substrate Modes 8

Figure 2: (a) Slot Coupling to Substrate Modes, (b) Front and Back Radiated Power as a Function of the Substrate Thickness (*h*) 8

Figure 3: Radiation Patterns for a Slot Antenna on a Dielectric Substrate 9

Figure 4: Refraction of the Rays by a Substrate Lens 11

Figure 5: Hyperhemispherical Lens with an Objective Lens 12

Figure 6: Elliptical Lens Refraction 13

Figure 7: Extended Hemispherical Lens 14

Figure 8: Required Geometry for Elliptical Lens Synthesis 15

Figure 9: Extended Hemisphere Approximation of an Ellipse 16

Figure 10: Elliptical and Synthesized Elliptical Lens Surfaces for $\varepsilon_r = 10$ 16

Figure 11: Slot-Coupled DRA on a Ground Plane 18

Figure 12: Slot Antenna Geometry 24

Figure 13: Hybrid Analysis Geometry 36

Figure 14: Dielectric-to-Air Boundary 37

Figure 15: Directional Error Caused by the Ray Approximation 42

Figure 16: Case I, Electric and Magnetic Field Components, $R_{lens} = 5.6\lambda_0$, $L_E = 0$ 44

Figure 17: Case I, Electric and Magnetic Field Components, $R_{lens} = 1.0\lambda_0$, $L_E = 0$ 46

Figure 18: Case I, Electric and Magnetic Field Components, $R_{lens} = 0.5\lambda_0$, $L_E = 0$ 48

Figure 19: Case I, Electric and Magnetic Field Components, $R_{lens} = 0.25\lambda_0$, $L_E = 0$ 49

Figure 20: Case II, Electric and Magnetic Field Components, $R_{lens} = 3\lambda_0$, $L_E = 0$ 51

Figure 21: Case II, Electric and Magnetic Field Components, $R_{lens} = 0.5\lambda_0$, $L_E = 0$ 52

Figure 22: Case II, Electric and Magnetic Field Components, $R_{lens} = 0.3\lambda_0$, $L_E = 0$ 53

Figure 23: Maximum Radial Component as a Percentage of the Maximum Transverse Component vs. the Normalized Lens Radius 55

Figure 24: Double-Slot Geometry 58

Figure 25: E- and H-plane Illuminations from a Double-Slot Array 59

Figure 26: Simulated Radiation Patterns for a Closed-Form Illuminated $5.6\lambda_0$-radius Elliptical Lens 60

Figure 27: Radiation Patterns for a Double-Slot Fed $1\lambda_0$-radius Elliptical Extension Lens 61

Figure 28: Radiation Patterns for a Double-Slot Fed $0.5\lambda_0$-radius Elliptical Extension Lens 62

Figure 29: E- and H-plane Illuminations from a Single Slot 63

Figure 30: Radiation Patterns for a Single Slot-Fed $1\lambda_0$-radius Elliptical Extension Lens 64

Figure 31: Radiation Patterns for a Single Slot-Fed $0.5\lambda_0$-radius Elliptical Extension Lens 64

Figure 32: Sampling Scheme for Directivity Calculations 66

Figure 33: Directivity of Single Slot Fed SLAs, $\varepsilon_r = 10$ 67

Figure 34: Reflection and Transmission Coefficients for $\varepsilon_r = 10$ 69

Figure 35: Reflection Loss versus Extension Length for $R_{lens} = 1\lambda_0$ and $\varepsilon_r = 10$ 70

Figure 36: Launch Angle and Incident Angle Geometry 71

Figure 37: (a) Incident Angle and (b) Reflection Coefficients for $R_{lens} = 1\lambda_0$, $\varepsilon_r = 10$, and $L_E = 8$ mm 71

Figure 38: (a) Incident Angle and (b) Reflection Coefficient for $R_{lens} = 1\lambda_0$, $\varepsilon_r = 10$, and $L_E = 10$ mm 72

Figure 39: (a) Incident Angle and (b) Reflection Coefficient for $R_{lens} = 1\lambda_0$, $\varepsilon_r = 10$, and $L_E = 13$ mm 72

Figure 40: (a) Incident Angle and (b) Reflection Coefficient for $R_{lens} = 1\lambda_0$, $\varepsilon_r = 10$, and $L_E = 15$ mm 73

Figure 41: Reflection Loss Curves for Four Lens Radii, $\varepsilon_r = 10$ 74

Figure 42: Normalised Reflection Loss Curves, $\varepsilon_r = 10$ 74

Figure 43: Reflection Loss for Various Lens Permittivities 75

Figure 44: Reflection Loss at the Elliptical and Hyperhemispherical Extension Lengths 76

Figure 45: Flux Tube Definition 78

Figure 46: Lens Meshing 78

Figure 47: Flux Tube Variation after Reflection 79

Figure 48: Lens Geometry in the ϕ-plane Viewed From Lens Apex 80

Figure 49: Theta-Plane Reflection 80

Figure 50: Theta-plane Geometry 81

Figure 51: Reflection Geometry 82

Figure 52: Roots When the Reflection Point is on the Cylinder 83

Figure 53: Flux Tube Criteria 84

Figure 54: Geometry for the Calculation of the Secondary Tube's Area at the Lens Surface 84

Figure 55: First Reflection's Effect on the Radiation Pattern of a $3\lambda_0$-radius Hyperhemispherical Lens 86

Figure 56: Primary and Secondary Ray Locations 87

Figure 57: Microstrip Coupled Slot Antenna Geometry 89

Figure 58: Power Fraction Coupled to Substrate Modes as a function of h/λ_0 on Silicon or GaAs 90

Figure 59: Equivalent Circuit of the Microstrip Coupled Slot 91

Figure 60: Open-Circuited Stub Reactance 91

Figure 61: Simulated Input Impedance Versus Stub Length for a Microstrip Coupled Slot 93

Figure 62: Least Squared Error Curve Fitting of the Slot and Open Stub Reactance 94

Figure 63: (a) Impedance vs. Slot Width on the Smith Chart at 10 GHz, (b) Impedance vs. Frequency for $W_S = 0.07$ cm 95

Figure 64: Substrate Lens Geometry 96

Figure 65: Photographs of the Manufactured Lenses 102

Figure 66: Photographs of the Experimental Antenna Substrate and Lens Assemblies 103

Figure 67: Measured Free-Space Slot Input Impedance 104

Figure 68: Co-polarised Free-Space Slot Radiation Patterns 105

Figure 69: Cross-polarised Free-Space Slot Radiation Patterns 105

Figure 70: Large Lens Holder Perturbation Effects 106

Figure 71: Small Lens Holder Perturbation Effects 107

Figure 72: (a) Measured Scaled Slot Free-Space Impedance and (b) Short-Circuited Impedance ... 108

Figure 73: Measured Input Impedance Schematic 109

Figure 74: De-embedded Impedance of the Free-Space Slot 110

Figure 75: Wide-Band De-embedding of the Free-Space Slot 112

Figure 76: E- and H-plane Radiation Patterns, 90 mm Radius Hyperhemispherical SLA 114

Figure 77: E- and H-plane Radiation Patterns, 30 mm Radius Hyperhemispherical SLA 115

Figure 78: E- and H-plane Radiation Patterns, 22.5 mm Radius Lens, 7.75 mm Extension 116

Figure 79: E- and H-plane Radiation Patterns, 15 mm Radius Lens, 3.175 mm Extension 117

Figure 80: E- and H-plane Radiation Patterns, 10 mm Radius Hyperhemispherical SLA 118

Figure 81: E- and H-plane Radiation Patterns, 7.5 mm Radius SLA, 3.8 mm Extension 119

Figure 82: E- and H-plane Radiation Patterns, 7.5 mm Radius SLA, 3.3 mm Extension 119

Figure 83: E- and H-plane Radiation Patterns, 7.5 mm Radius SLA, 2.9 mm Extension 120

Figure 84: E- and H-plane Radiation Patterns, 7.5 mm Radius SLA, 2.3 mm Extension 120

Figure 85: E- and H-plane Measured Cross-Polarisation Radiation Patterns,
90 mm Radius Hyperhemispherical SLA 121

Figure 86: Far-field Approximation Geometry 137

Figure 87: Cascaded Two-Port and One-Port 140

List of Tables

Table 1: Documented Extended Hemispherical SLA Permittivities, Frequencies, and Sizes 19

Table 2: Documented Hemispherical DRA Permittivities, Operating Frequencies, and Sizes 19

Table 3: Double Slot Array Parameters 43

Table 4: Single Slot Antenna Parameters 50

Table 5: Reflection Losses at Important Extension Length Values, $\varepsilon_r = 10$ 75

Table 6: Reflection Losses at Important Extension Lengths for Four Lens Permittivities 76

Table 7: Simulated Input Impedance Versus Stub Length 93

Table 8: Simulated Input Impedance vs. Slot Width for $L_S = 0.7$ cm, $L_o = W_S/2$ and $f = 10$ GHz 95

Table 9: Simulated Input Impedance vs. Frequency for $L_S = 0.7$ cm, $W_S = 0.07$ cm and $L_o = W_S/2$. 95

Table 10: Hyperhemispherical Lens Specifications at 10 GHz 101

Table 11: Empirical Extension Lengths for the 7.5 mm Radius Lens 101

Table 12: Approximate F/B Ratios of the Measured SLAs 122

List of Acronyms

AF	array factor
DR	dielectric resonator
DRA	dielectric resonator antenna
F/B	front-to-back ratio
E-field	electric field
E-plane	plane containing the electric far-field vector
GaAs	gallium arsenide
GO	geometrical optics
H-field	magnetic field
H-plane	plane containing the magnetic far-field vector
IC	integrated circuit
PO	physical optics
RL	reflection loss
Si	silicon
sinc(x)	"sinc" function: sin(x)/x
SLA	substrate lens antenna
TE	transverse electric
TE-POL	transverse electric polarisation
TM	transverse magnetic
TM-POL	transverse magnetic polarisation
VSWR	voltage standing wave ratio

Glossary

$\underline{0}$	the null dyadic (a null 3x3 matrix)
$\underline{1}$	the unit dyadic (the unity 3x3 matrix)
a	minor axis of an ellipse
A	any function
$\underline{A}$	any dyadic
b	major axis of an ellipse
c	geometrical focus of an ellipse
d	empirical lens scaling factor; or spacing between radiating elements
D	largest dimension of an aperture; or diameter of a lens
D_0	maximum directivity of an antenna, often simply called the directivity
E	scalar electric field in units of [V/m]
E_0	maximum magnitude of the electric field
E_a	scalar electric field inside an aperture
$E_{a\eta}$	scalar electric field in the η direction inside an aperture
$E_{a\xi}$	scalar electric field in the ξ direction inside an aperture
E_r	magnitude of the electric field in the radial direction
E_x	magnitude of the electric field in the x direction
E_y	magnitude of the electric field in the y direction
E_z	magnitude of the electric field in the z direction
E_ϕ	magnitude of the electric field in the ϕ direction
E_θ	magnitude of the electric field in the θ direction
$\vec{E}^{FF}$	far-field electric field vector
$\vec{E}^{PO}$	electric field vector calculated using Physical Optics
$\vec{E}_{rad}$	radial electric field vector
$\vec{E}_S$	electric field vector in the slot or aperture
$\vec{E}_e$	electric field vector due to an electric source current
$\vec{E}_f$	vector of the electric field that has been reflected from an interface
$\vec{E}_i$	vector of the electric field that is incident upon an interface
$\vec{E}_m$	electric field vector due to a magnetic source current
$\vec{E}_t$	vector of the electric field that has been transmitted through an interface
$\vec{E}_{transv}$	electric field vector that is transverse to the direction of propagation
$\vec{E}_{//i}$	vector of the incident electric field that is parallel to the plane of incidence
$\vec{E}_{\perp i}$	vector of the incident electric field that is perpendicular to the plane of incidence
$\vec{\mathcal{E}}$	electric field vector including both the space and time phasors
f	frequency in cycles per second [Hz]
f_x	x component of the wave amplitude vector
f_y	y component of the wave amplitude vector
$\vec{f}$	vector of the reflected ray's direction of propagation; or wave amplitude vector
$F(\theta,\phi)$	normalised radiation intensity in spherical coordinates, in units of [W/sr]
$\mathcal{F}_{2D}$	two-dimensional Fourier Transform
$\mathcal{F}_{2D}^{-1}$	inverse two-dimensional Fourier Transform
g(R)	free-space scalar Green's function
G	any dyadic Green's function

$\underline{G_{EJ}}$	dyadic Green's function relating the electric field to the electric source current
$\underline{G_{EM}}$	dyadic Green's function relating the electric field to the magnetic source current
$\underline{G_{HJ}}$	dyadic Green's function relating the magnetic field to the electric source current
$\underline{G_{HM}}$	dyadic Green's function relating the magnetic field to the magnetic source current
H	scalar magnetic field in units of [A/m]
H_r	magnitude of the magnetic field in the radial direction
H_x	magnitude of the magnetic field in the x direction
H_y	magnitude of the magnetic field in the y direction
H_z	magnitude of the magnetic field in the z direction
H_ϕ	magnitude of the magnetic field in the ϕ direction
H_θ	magnitude of the magnetic field in the θ direction
$\bar{H}_e$	magnetic field vector due to an electric source current
$\bar{H}^{FF}$	far-field magnetic field vector
$\bar{H}_m$	magnetic field vector due to a magnetic source current
$\bar{H}^{PO}$	magnetic field vector calculated using Physical Optics
h	thickness of the substrate; or hypotenuse of a right triangle
i	index into an array
$\bar{i}$	vector of the incident ray's direction of propagation
j	index into an array; or imaginary number ($\sqrt{-1}$)
$\bar{J}$	electric current density vector, in units of [A/m^2]
$\bar{J}_S$	electric surface current, in units of [A/m]
k	wavenumber
$\bar{k}$	wavevector
$\bar{k}_{local}$	wavevector of a localised plane wave
L_E	length of the cylindrical lens extension, also known as the extension length
L_o	length of the open-circuited microstrip stub
L_o'	length of the open-circuited microstrip stub destined for use with the lenses
L_S	length of the slot
L_S'	unscaled length of the slot antenna destined for use with the lenses
L_S''	scaled length of the slot antenna destined for use with the lenses
M	an integer
$\bar{M}$	magnetic current density vector, in units of [A/m^2]
$\bar{M}_S$	magnetic surface current, in units of [A/m]
N	an integer
n	refractive index ($\sqrt{\varepsilon_r}$), dimensionless
$\bar{n}$	normal vector
$\hat{n}$	unit normal vector
P	point in three-dimensional space; or power in watts [W]
P_{rad}	total radiated power, in watts [W]
$\hat{P}_{//}$	unit vector that is parallel to the plane of incidence
$\hat{P}_\perp$	unit vector that is perpendicular to the plane of incidence
r	spherical radial coordinate
$\bar{r}$	vector from the origin to an observation point
$\bar{r}'$	vector between a source point and the origin
R	scalar distance between an observation point and a source point ($\lvert\bar{r} - \bar{r}'\rvert$)
R_{DRA}	radius of a hemispherical dielectric resonator antenna

R_{IN}	input resistance
R_{IN}'	unloaded input resistance of the unscaled slot destined for use with the lenses
R_{lens}	radius of a lens
R_{SLOT}	self-resistance of the slot antenna
$\bar{R}$	vector from a source point to an observation point ($\bar{r} - \bar{r}'$)
$\hat{R}$	unit vector from a source point to an observation point
$\underline{\hat{R}\hat{R}}$	matrix multiplication of $\hat{R}$ with itself, yielding a dyadic
s_{11}	scattering parameter (also s_{12}, s_{21}, and s_{22})
t	time
$\bar{t}$	vector of the transmitted ray's direction of propagation
u	an independent variable
U	scalar field magnitude
U_{max}	maximum radiation intensity, in units of watts per steradian [W/sr]
V'	volume containing all of the sources
W_S	width of the slot
W_S'	unscaled width of the slot antenna destined for use with the lenses
W_S''	scaled width of the slot antenna destined for use with the lenses
W_T	width of the microstrip transmission line
x	Cartesian coordinate
x'	distance in x between source point and origin; or parametric equation coordinate
$\hat{x}$	unit Cartesian coordinate
X_{IN}	input reactance
X_{IN}'	unloaded input reactance of the unscaled slot destined for use with the lenses
x_f'	parametric equation coefficient
x_p'	distance in x to the intersection point of the incident ray and the hemisphere
x_{p2}'	distance in x to a second intersection point of the incident ray and the hemisphere
X_{SLOT}	self-reactance of the slot antenna
X_{SLOT}'	unloaded self-reactance of the unscaled slot destined for use with the lenses
X_{STUB}	reactance of the open-circuited microstrip stub
X_{STUB}'	reactance of the open-circuited microstrip stub destined for use with the lenses
y	Cartesian coordinate
y'	distance in y between a source point and the origin
$\hat{y}$	unit Cartesian coordinate
z	Cartesian coordinate
z'	distance in z between source point and origin; or parametric equation coordinate
z_f'	parametric equation coefficient
z_p'	distance in z the intersection point of the incident ray and the hemisphere
z_{p2}'	distance in z to a second intersection point of the incident ray and the hemisphere
$\hat{z}$	unit Cartesian coordinate
Z_0	wave impedance in free-space
Z_C	characteristic transmission line impedance
Z_d	wave impedance in a dielectric
Z_{DIPOLE}	input impedance of a printed dipole antenna
Z_{IN}	input impedance
Z_S	self-impedance of the slot antenna
Z_{SLOT}	also the self-impedance of the slot antenna
Z_{SP}	impedance taken at the slot plane
β	phase constant; or auxiliary angle
β_1	auxiliary angle
β_2	auxiliary angle
γ	auxiliary angle
Γ	reflection coefficient

Γ_{SP}	reflection coefficient taken at the slot plane
$\Gamma_{//}$	reflection coefficient, parallel polarisation
$\Gamma_{\perp}$	reflection coefficient, perpendicular polarisation
$\delta(r)$	impulse function
Δ	distance between a spherical wave and a plane
Δd	one-dimensional distance interval
ΔL_o	shift in the reference plane of the open-circuited microstrip stub
ΔS	two-dimensional surface area
$\Delta\phi$	increment size in ϕ direction
$\Delta\theta$	increment size in θ direction
ε	permittivity, ($\varepsilon_r\varepsilon_0$) in units of [F/m]
ε_0	permittivity of free-space (8.854e-12 [F/m])
ε_{cap}	relative permittivity of the quarter-wave matching cap layer used on lenses
ε_{eff}	effective relative permittivity of a transmission line
ε_m	mean relative permittivity, also known as the mean dielectric constant
ε_r	relative permittivity, also known as the dielectric constant
ϕ	spherical coordinate
η	coordinate in a two-dimensional plane
ξ	coordinate in a two-dimensional plane
λ	any wavelength in general
λ_0	wavelength in free-space
λ_d	wavelength in a dielectric medium
λ_g	guided wavelength in a transmission line
λ_m	mean wavelength
μ	permeability, ($\mu_r\mu_0$) in units of [H/m]
μ_0	permeability of free space (4πe-7 [H/m])
μ_r	relative permeability
θ	spherical coordinate
θ_B	Brewster angle
θ_c	critical angle for total internal reflection
θ_i	angle subtended between the incident ray and the normal vector
θ_f	angle subtended between the reflected ray and the normal vector
θ_t	angle subtended between the transmitted ray and the normal vector
ρ_e	electric volume charge density, in units of [C/m^3]
ρ_m	magnetic volume charge density, in units of [C/m^3]
$\tau_{//}$	transmission coefficient, parallel polarisation
$\tau_{\perp}$	transmission coefficient, perpendicular polarisation
ω	angular frequency in units of [rad/s]

1. Introduction

1.1 Background

The recent and projected deployments of various millimeter wave systems have resulted in an increased demand for high performance millimeter wave antennas. Among these are ground-based systems such as LMCS and LMDS, space-based systems such as Celestri and Teledesic, and applications such as intelligent vehicles.

LMCS (Local Multipoint Communications System) is the proposed Canadian Ka-band ground-based wireless telecommunications system, in which subscribers are offered a high-speed digital data downlink and a lower speed uplink. Some of the possible applications for this service include: access to the internet, interactive television broadcasts, voice, and messaging. LMDS, (where the D stands for Distribution), is a similar Ka-band system that is currently deployed in certain U.S. markets to provide wireless "cable" television services. The Celestri System is Motorola's proposed space-based broad-band communications system. Designed to link Geosynchronous- and Low-Earth Orbit (GEO and LEO) space networks with terrestrial networks, this system will also provide high-speed, two-way subscriber services at Ka-band frequencies. Teledesic also plans to offer similar services using LEO satellites. Possible services include: access to the internet, high-quality voice, video conferencing, and broadcasting. Finally, intelligent vehicles will use millimeter wave sensors in collision avoidance radar systems.

What all of these systems have in common is the need for low cost, low loss, light weight, directive, mobile antennas operating in the Ka and millimeter wave frequency bands.

These requirements can all be met by bringing the antenna closer to the transceiver electronics. The most obvious way to achieve this is to use some type of planar antenna that can be directly

integrated with the circuit board. Slot and patch antennas are the two strongest candidates due to their simple geometry. A tremendous amount of work has been done on patch-based structures; therefore this work is limited to the study of slot-based configurations. The slot antenna's radiation characteristics are greatly improved by using a dielectric lens.

Two distinct classes of dielectric-loaded slot antennas, both identical in shape and form, have classically been analysed using very different techniques. These antennas consist of a slot in the metal backing of a substrate upon which is placed a hemispherical block of low-loss dielectric material. Depending on the electrical size of this dielectric block, the antennas belong either to the class of radiators known as hemispherical Dielectric Resonator Antennas (DRA), or to the class of radiators known as Substrate Lens Antennas (SLA). If the hemisphere's radius is larger than a free-space wavelength, the ensemble is a SLA; whereas if it is approximately one half of a guided wavelength, the ensemble is a DRA.

Substrate lenses have been developed in an effort to improve the performance of planar substrate antennas that have bi-directional radiation patterns. By mimicking a semi-infinite dielectric half space, a high permittivity lens can render the slot's radiation pattern almost unidirectional. Furthermore, a substrate lens can reduce the amount of radiation that is lost due to coupling to substrate modes. Substrate modes are defined as leakage due to radiation that is trapped within the confines of the substrate. At lower microwave frequencies, however, the advantages of using a substrate lens come at a price, as the physical size of the lens becomes bulky and inconvenient.

The development of DRAs, on the other hand, has been based on the theory of dielectric resonators. These resonators are commonly used in filtering circuit applications. DRAs assume various shapes, including cylinders, rectangular cubes, and hemispheres. By coupling radiation to one of the known modes of the resonator, this circuit element can become an efficient radiator.

In addition to the previously mentioned features of substrate lenses, a hemispherical lens can be used to focus energy on or from the slot radiator; that is, the lens can increase the antenna's directivity. This is achieved by inserting a cylinder of the same dielectric material between the slot and the hemisphere. In fact, by properly choosing the thickness of the cylindrical extension, the directivity of the antenna can be increased to values that approach the diffraction limit of the structure, that is, its theoretical maximum. Such structures have never been studied as DRAs, which typically have very broad radiation patterns.

The numerical analysis of a SLA is much simpler than the numerical methods that are required for a DRA. Due to the larger size of the lens, ray optics can be used to predict the SLA's radiation pattern. This simple analysis also borrows from work that has been done for planar antennas on semi-infinite dielectric substrates, allowing the designer to use simple closed form expressions to scale the size and the impedance of an existing free-space planar antenna for use with a dielectric lens. No simple scaling equations exist for converting a free-space antenna to a DRA.

1.2 Thesis Objectives and Motivation

The original goal of this project was to use a dielectric substrate lens to improve the radiation performance of a novel 30 GHz gallium arsenide monolithic active slot antenna. This antenna suffers from a broad, bi-directional radiation pattern, making it a suitable candidate for a lens. A significant portion of the previous work that was done on this active antenna focuses on the development of a computer program that can predict the input impedance of the slot antenna as a function of its length, width, and feed position. Using an electrically large lens would allow the use of simple closed-form equations to scale the impedance and length of the slot antenna. However, the question of a suitable lens size cannot be answered. The existing circuit is monolithic, so a small physical lens size is desired. Also, if these active elements are to be used in a fully scanning array, the distance between the elements would be restricted to one half of a free-space wavelength,

again requiring a small lens. However, as previously stated, substrate lens radii have typically been larger than a free-space wavelength. Surprisingly, little research has been done on electrically small lenses.

Another option would be to replace the slot with a DRA. However, it would be counter-productive in this case since the goal is to build upon the previous work that has been done on the active slot: using a DRA would require the removal of the computer program that calculates the input impedance of the active slot antenna.

Thus, the goal of this project is the study of electrically small substrate lenses with slot feed antennas, electrically small meaning that the lens radius is smaller than a free-space wavelength.

More specifically, the first objective of this thesis is to determine the structure's limit of operation, as a lens, as its physical size is reduced. This involves verifying the validity of the equations that are used to scale an antenna's size and input impedance when a free-space antenna is to be fitted with an electrically large lens.

The second objective is to determine the effects of reducing the lens size on a SLA's radiation pattern. This will be done both experimentally and analytically. The current technique that is used to simulate and to predict a SLA's radiation pattern uses many far-field approximations; approximations that must surely fail as the size of the structure is reduced. Therefore, the third objective of the thesis is to predict this failure and to develop a more robust simulation technique that can be used for electrically small lenses.

The fourth and final objective of this thesis is to point out similarities that exist between DRAs and SLAs.

1.3 Thesis Contribution

Very little work has been done on electrically small lenses. Indeed, these structures seem to fall between the categories of DRAs and SLAs. At the very least, this work will provide experimental measurements of small substrate lenses fed by slot antennas. Similar data is currently lacking in the literature.

This thesis will also provide an improved simulation technique that can be used for electrically small lenses, extending the size range of SLAs that can be accurately simulated. The work will also examine the limits of the existing simulation techniques for substrate lenses.

By analysing small lenses, a lower size limit will be established for SLAs. This will allow designers to reduce the physical size of their lenses, leading to more cost-effective and compact designs.

Finally this work represents the first attempt to bridge the theoretical gap that exists between SLAs and hemispherical DRAs, two classes of antennas that require different analyses and yet share the same shape and construction.

1.4 Thesis Organisation

The second chapter of this thesis, entitled "Review of Substrate Lens Antenna and Dielectric Resonator Antenna Technology", revisits and expands the topics that were briefly covered in the introduction. The chapter opens by examining the disadvantages of certain planar substrate antennas, which includes the slot antenna. The review then shifts to the development and to the use of lenses as solutions to these problems. The various shapes that these lenses may assume, and the effects of those shapes are then studied. Chapter Two concludes with a survey of DRA technology.

The foundations of the subject having been laid out, Chapter Three, "Analysis Methods", begins by examining the existing methods that are used to simulate SLAs numerically. The anticipated failure of these methods is then explained for the case of small lenses. New simulator requirements are described, and several analysis alternatives are explored as possible candidates to be used in a new simulator. The third chapter ends by justifying the selection of the Physical Optics method as the analysis technique to be used in the new simulator.

Chapter Four, "Physical Optics Hybrid Simulation Technique", is devoted to the development of the simulator. The theory of Physical Optics is explained in detail, and a step-by-step outline of the hybrid analysis technique is given. The chapter concludes by analysing the limitations of the new simulator.

Simulation results are presented in Chapter Five. Published results for a double slot-fed SLA are duplicated and serve to validate the new simulator. Next, the simulator is used to predict the failure of the existing simulation technique for small SLAs. Simulated results are then given for the 10 GHz single slot-fed SLAs that are to be experimentally measured. The directivities of slot-fed SLAs are calculated and a reflection loss analysis is performed.

Chapter Six deals with the experimental aspects of this thesis. First, the design of the slot antenna, lenses, and test jig are described. The chapter closes with the presentation and the analysis of the experimental measurements of the slot-fed SLAs.

Conclusions are drawn in the seventh and final chapter of this thesis, and future work is also outlined therein.

2. Review of Substrate Lens Antenna and Dielectric Resonator Antenna Technology

Before undertaking the analysis of SLAs, it is necessary to provide some background material. This chapter begins by describing the disadvantages of certain antennas printed on dielectric substrates. The chapter then explains how dielectric lenses are used to circumvent these antennas' problems. The characteristics of the main lens types are presented, and the chapter closes with a summary of hemispherical DRAs.

2.1 Planar Antennas on Dielectric Substrates

The past two decades have seen an explosion in the number of technical articles devoted to the study of printed circuit antennas. These antennas are also known as *integrated circuit (IC) antennas* and *planar antennas on substrates*. A thorough review of the literature up to 1992 has been compiled by Rebeiz [1]. Among the plethora of designs falling into this category are: microstrip patches, printed dipoles, slots, vees, folded slots, spiral antennas, and bowtie antennas. The literature abounds with examples of these and no attempt is made to summarize all of them here. Several excellent references may be found in [1-4].

Many advantages are inherent to IC antennas, such as: low weight, conformity to a given surface, low cost, and ease of monolithic integration. These antennas are particularly well suited to millimeter and sub-millimeter wave applications, where the small dimensions and relatively high ohmic losses make standard free-space antennas, such as horns, impractical.

Along with the advantages of IC antennas, one must be aware of certain caveats that are also inherent to this type of antenna. For example, many IC antennas printed on thick substrates radiate most of their power into the dielectric. For slot antennas, the ratio of the power radiated into the dielectric to that radiated into the air is $\varepsilon_r^{3/2}$:1, where ε_r is the permittivity of the substrate [2].

To further hamper the antenna's performance, most of the power radiated into the dielectric can become trapped therein due to strong coupling to surface modes, which are also known as substrate modes [2,4,5]. A ray approximation of this power loss phenomenon is shown below, where θ_c is the critical angle for total internal reflection of the rays.

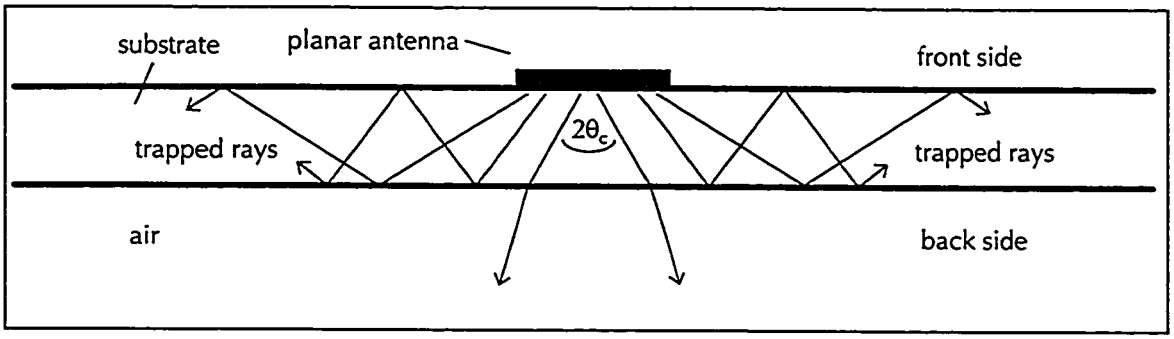

Figure 1: Ray Approximation of Substrate Modes

Substrate mode coupling for resonant printed dipoles [6], microstrip patches [5], and elementary dipoles and slots [4] has been calculated. The power coupling to substrate modes for elementary slots on silicon or gallium arsenide is shown in Figure 2a [4]. Note that the power is normalized to the total power that the slot radiates in free-space.

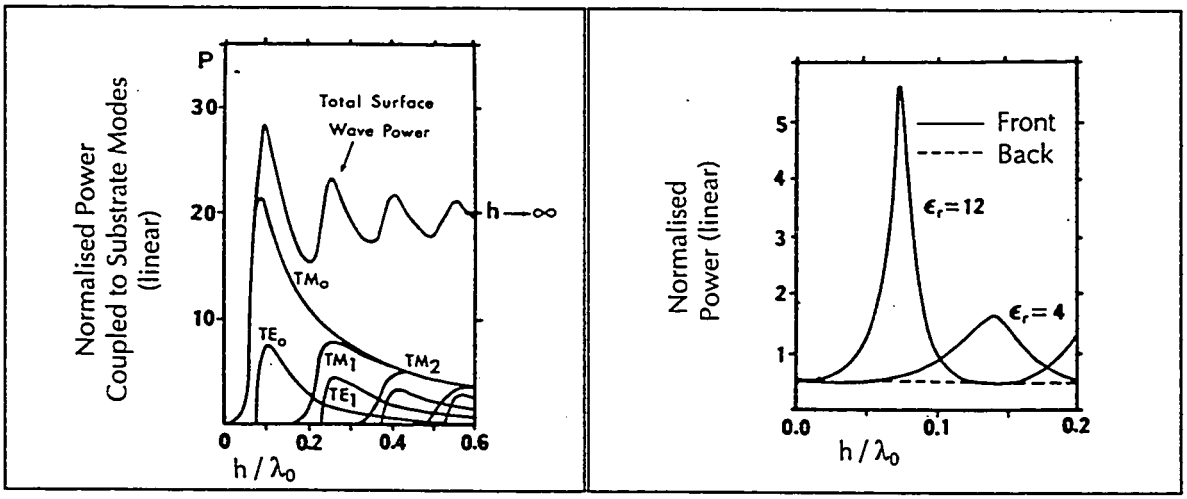

Figure 2: (a) Slot Coupling to Substrate Modes,
(b) Front and Back Radiated Power as a Function of the Substrate Thickness (*h*)

Figure 2b shows the normalized power radiated through the dielectric side of the substrate and into the air (back side) and the power radiated directly into the air (front side) versus the substrate thickness. The ratio of these is also known as the Eront to Back ratio, symbolized by F/B. Referring to Figure 2a, for low loss operation, the substrate thickness for slots should be less than $0.04\lambda_0$ [1]. At millimeter wave frequencies and above, this translates into impractically thin substrates. Indeed, for the active slot antenna that serves as the motivation for this thesis [7], the gallium arsenide substrate is thinned to h = 90 μm ($0.009\lambda_0$), resulting in a very fragile chip. Such fragility is an obvious impediment to higher yields. Thinning the substrate also reduces the F/B ratio of the antenna, as shown in Figure 2b above. Figure 3 shows the calculated front and back patterns of an elementary slot antenna on two different substrates [2].

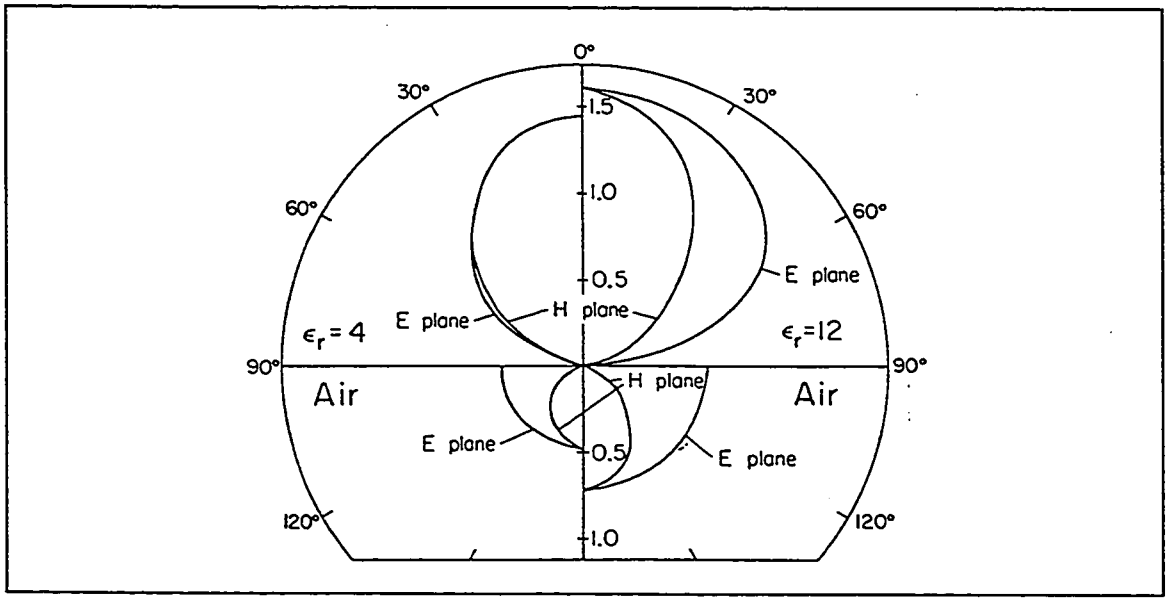

Figure 3: Radiation Patterns for a Slot Antenna on a Dielectric Substrate
Left: $\varepsilon_r = 4$, $h = 0.10\lambda_0$. Right: $\varepsilon_r = 12$, $h = 0.04\lambda_0$. (Linear Gain Radial Coordinate)

It is of interest to note that the substrate mode losses are not shown in the patterns of Figure 3. This power loss is only evident when the gain of the antenna is measured directly. The figure shows that the F/B ratio is approximately 3.3 dB for $\varepsilon_r = 12$. Even if the antenna was operated at $h/\lambda_0 = 0.075$, where the maximum F/B ratio of $\log(5.75/0.5) \approx 10.6$ dB is achieved (Figure 2b), the antenna would still suffer from a significant amount of gain loss due to substrate mode coupling (Figure 2a).

Referring again to the active slot antenna of [7], its relatively low ratio of $h/\lambda_0 = 0.009$ confirms the fact that it is radiating bi-directionally (F/B ≈ 0 dB).

Although in practice *resonant* slots are used instead of elementary slots, the gain and pattern of resonant half-wave antennas do not differ greatly from those of elementary antennas [3,4]. Figure 2a and Figure 2b therefore serve as helpful guides for designing integrated circuit antennas.

Thus far it has been shown that very thin substrates are desired. Another way to avoid the presence of the problematic substrate modes is by making the substrate thickness infinite ($h \rightarrow \infty$). Integral equation formulations for resonant printed dipoles [8], slots [9], dipoles and slots [3], and folded-slots [10] on dielectric half spaces have been solved, yielding the ideal self impedance and radiation characteristics of these antennas.

2.2 Substrate Lenses - Background

An infinite dielectric half-space can be synthesized by using a lens of the same permittivity attached to the antenna substrate, hence the name "substrate lens". By doing so, the power coupling to substrate modes is eliminated. As illustrated in Figure 4, the rays now approach the interface at almost normal incidence, thereby eliminating total internal reflections.

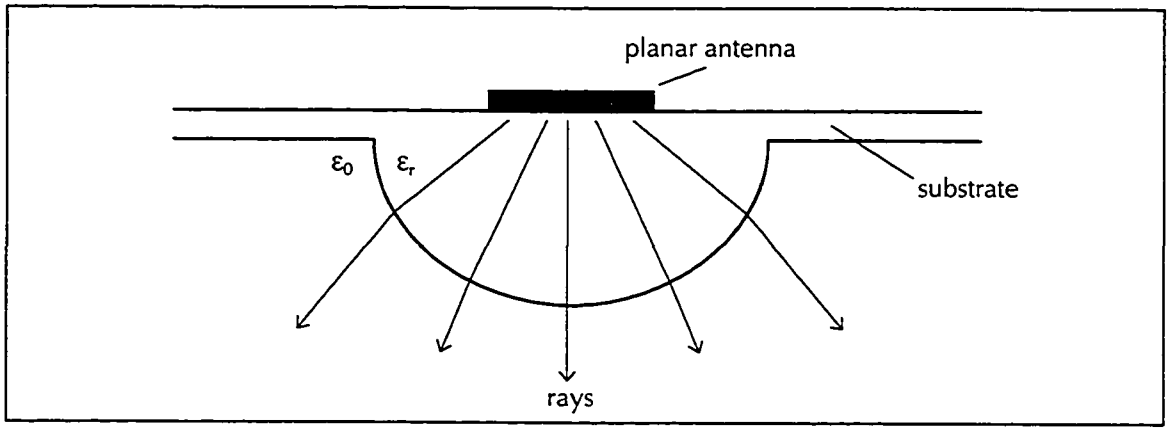

Figure 4: Refraction of the Rays by a Substrate Lens

The disadvantages of the substrate lens are those of any system using refractive optics: absorption losses and reflection losses at the dielectric-to-air interface. The former becomes significant only at relatively high frequencies (millimeter and sub-millimeter wavelengths) [11]. Reflection loss[†] at the interface can be quite significant for semiconductor lenses if they are not fitted with a matching layer [12-14]: the reflection loss at normal incidence is 1.55 dB for silicon (30% reflected power) and 1.67 dB for gallium arsenide (32% reflected power).

It is possible to reduce the reflection loss to negligible values by covering the lens with a quarter-wave matching cap layer. The permittivity of the cap is chosen as $\varepsilon_{cap} = \sqrt{\varepsilon_r}$, where ε_r is the permittivity of the lens. Polyethylene and polystyrene have been used on silicon lenses [12,14]. Although the permittivities of 2.25 for polyethylene and 2.54 for polystyrene are not perfect matches for silicon ($\varepsilon_{cap} = \sqrt{11.7} = 3.42$), these materials have the advantage of being easily fitted to the lens by thermal molding. The resulting mismatch for polyethylene has been estimated to produce a reflection loss of 0.2 dB (4.5% reflected power).

[†] reflection loss is defined as $-10\log_{10}\left(1-\Gamma^2\right)$, where the reflection coefficient is $\Gamma = \dfrac{\sqrt{\varepsilon_r}-1}{\sqrt{\varepsilon_r}+1}$.

Documented lenses assume various shapes, including hemispheres [15-17], hyperhemispheres [18-20], ellipsoids [21,22], and extended hemispheres [13,14,23-35]. The performance of these four basic types will be briefly compared.

Hemispherical lenses do not refract the rays from the feed antenna and therefore do not increase the gain of the corresponding radiation pattern. No refraction occurs because the rays emanating from the feed antenna are spherically divergent and arrive with normal incidence at the lens-to-air interface.

A hyperhemispherical lens is a sphere that has been truncated at a distance R_{lens} / n further from the sphere's center [2], where R_{lens} is the radius of the sphere and n is its refractive index. If an optical system is designed such that all of the rays are focused to a point, the addition of a properly designed hyperhemispherical lens will cause the rays to focus at the base of the lens, as shown in Figure 5. For this reason, hyperhemispherical (and hemispherical) lenses are usually paired with objective lenses when they are used in imaging systems. The refraction of the hyperhemispherical lens increases the gain of the feed antenna by a factor of n^2 [1].

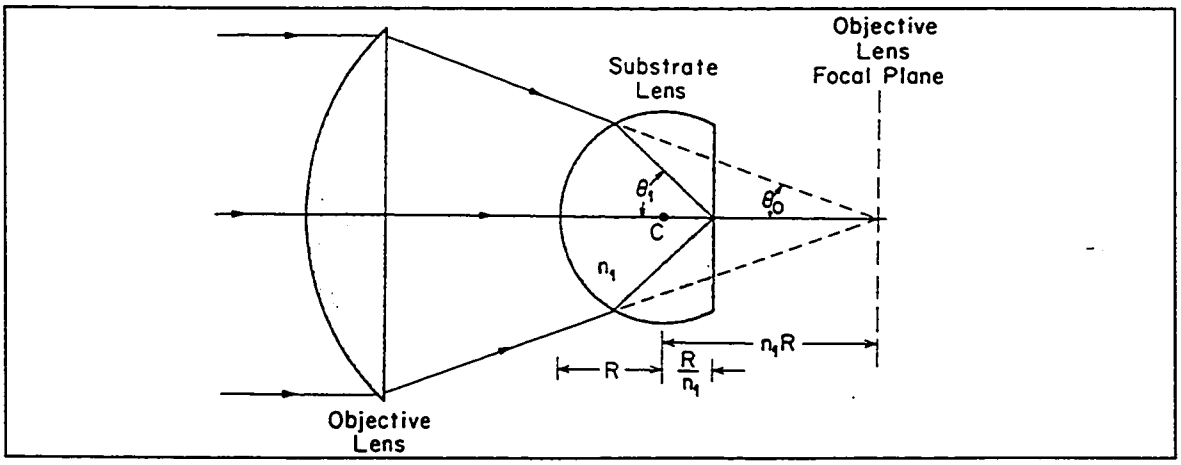

Figure 5: Hyperhemispherical Lens with an Objective Lens

Elliptical lenses are ellipsoids that have been truncated at the focus that is furthest from the lens aperture. The latter can also be made the focal point of the lens, as illustrated in Figure 6. For the

optical focus of the ellipse to correspond to its geometrical focus, the lengths of the major and minor axes of the ellipse are chosen as a function on the refractive index of the material. The exact relation is given later in this section. The elliptical lens focuses a plane wave to a point (and vice-versa), giving the lens an infinite magnification [1]. As a result, the feed antenna's radiation pattern will be diffraction limited by the aperture of the lens, which is its theoretical maximum [13].

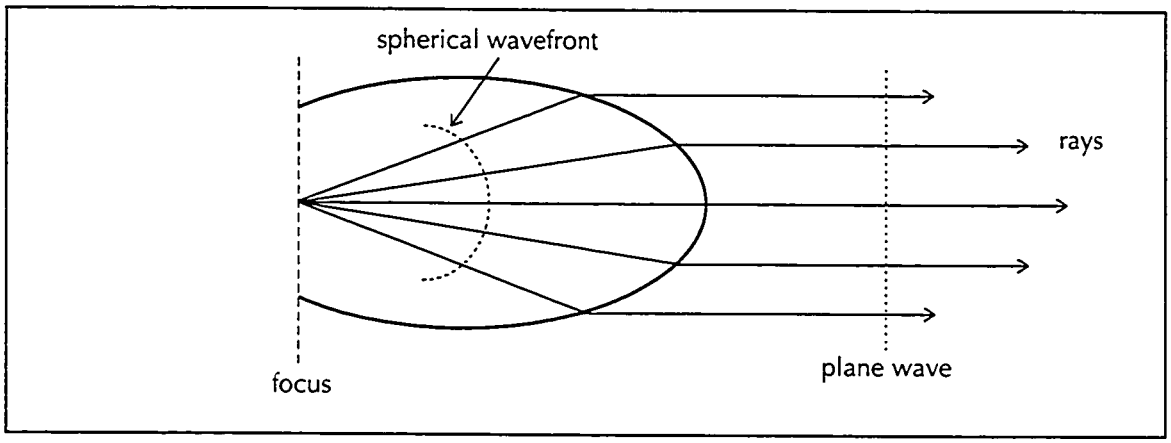

Figure 6: Elliptical Lens Refraction

Canonical elliptical and hyperhemispherical lenses are challenging structures to manufacture. However, they can be approximated by using *extended hemispherical lenses* [13]. An extended hemispherical lens consists of a hemisphere that has one or several cylindrical slabs appended to its flat side, as shown in Figure 7. The total length of the cylinder is called the *extension length* (L_E).

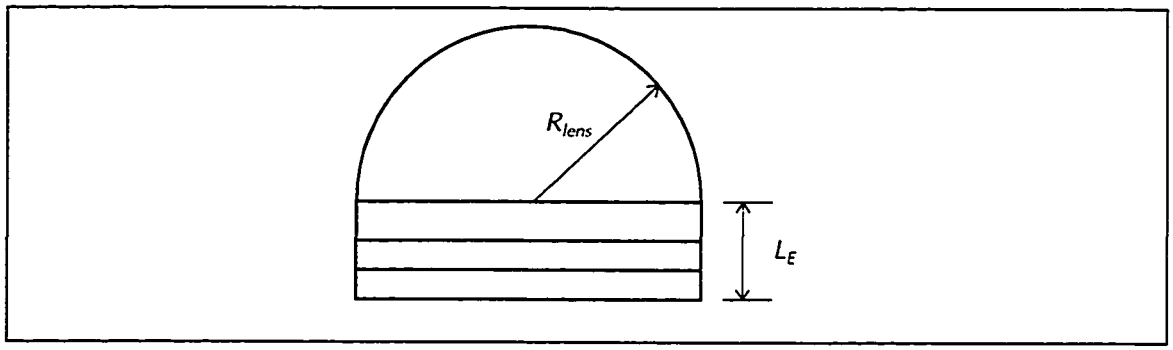

Figure 7: Extended Hemispherical Lens

To synthesize a hyperhemispherical lens, the extension length is simply chosen as $L_E = R_{lens} / n$ [2]. The extension length that is required to synthesize an elliptical lens is computed using a simple algorithm [13], although other methods do exist [23]. The equation for an ellipse in the *xy*-plane is:

$$\left(\frac{x}{a}\right)^2 + \left(\frac{y}{b}\right)^2 = 1, \tag{2-1}$$

where *a* has been chosen as the minor axis, and *b* is the major, meaning that the ellipse is longer along the y-axis than it is along the x-axis.

The ellipse's geometrical foci are located at $\pm c$, defined as:

$$c = \sqrt{b^2 - a^2}\,. \tag{2-2}$$

It is also known from optics that for a given index of refraction *n*, the eccentricity of the ellipse such that the geometrical focus becomes the optical focus is [36]:

$$eccentricity = \frac{\sqrt{b^2 - a^2}}{b} = \frac{1}{n}. \tag{2-3}$$

From these two equations, one finds that:

$$b = \frac{a}{\sqrt{1 - \frac{1}{n^2}}} \quad \text{and} \quad c = \frac{b}{n} = \frac{a}{n\sqrt{1 - \frac{1}{n^2}}} = \frac{a}{\sqrt{n^2 - 1}}. \tag{2-4}$$

The geometry is shown in Figure 8.

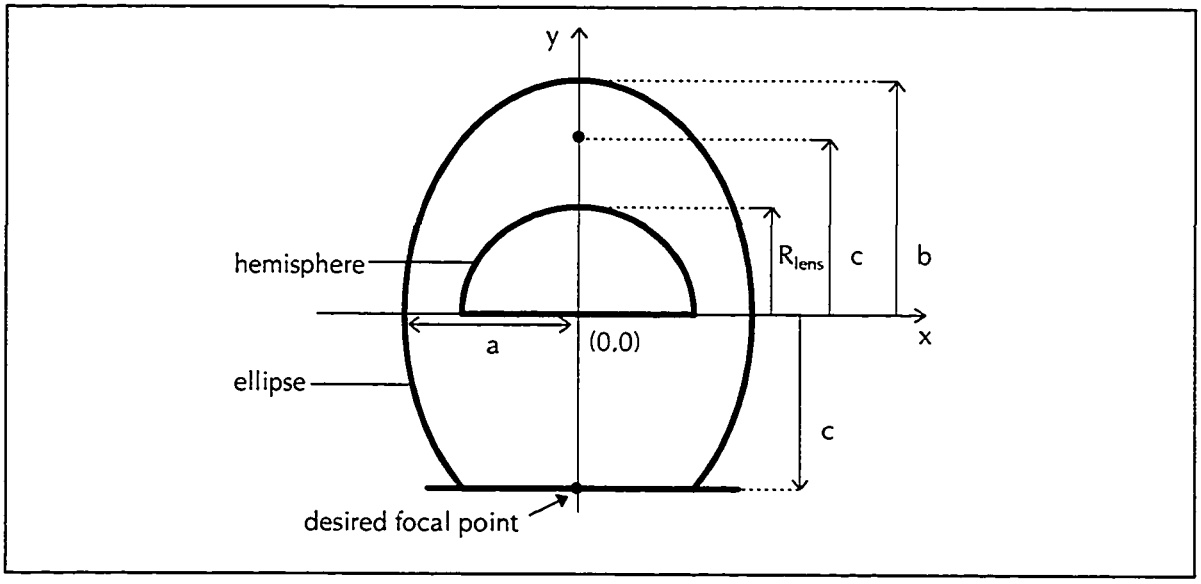

Figure 8: Required Geometry for Elliptical Lens Synthesis

Let a hemisphere of radius R_{lens} also be centered at the origin and defined by the equation:

$$x^2 + y^2 = {R_{lens}}^2 \ , \ y \geq 0 . \tag{2-5}$$

To approximate the ellipse, the hemisphere is shifted up vertically by L_E so that its zenith coincides with that of the ellipse. The distance from an ellipse's zenith to its more distant focus is $b + c$, therefore the extension length must be $L_E = b + c - R_{lens}$. If both the hemispherical lens radius and the refractive index are given, the only independent variable is the minor axis of the ellipse, a. The latter is adjusted so that the elliptical and hemispherical surfaces have the closest match at the aperture. This usually occurs for a very close to R_{lens}, so a is expressed as a fraction of the lens radius: $a = dR_{lens}$. The three remaining variables become:

$$b = \frac{dR_{lens}}{\sqrt{1-\frac{1}{n^2}}} \ , \quad c = \frac{dR_{lens}}{\sqrt{n^2-1}} \ , \text{ and } \quad L_E = b + c - R_{lens} = dR_{lens}\left(\frac{1}{\sqrt{1-\frac{1}{n^2}}} + \frac{1}{\sqrt{n^2-1}} - 1\right). \tag{2-6}$$

Referring to Figure 9 below, the extended hemisphere becomes a very good geometrical approximation to an elliptical lens at high dielectric constants ($\varepsilon_r > 10$) [13].

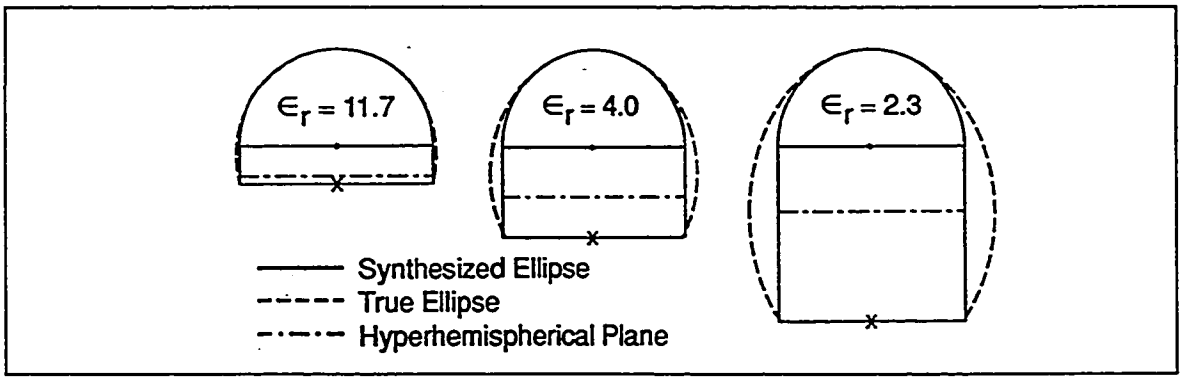

Figure 9: Extended Hemisphere Approximation of an Ellipse

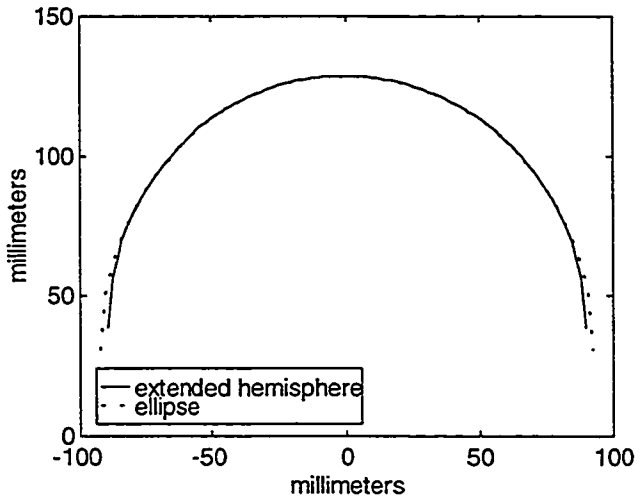

Figure 10: Elliptical and Synthesized Elliptical Lens Surfaces for $\varepsilon_r = 10$

The synthesis is repeated for a lens radius of $R_{lens} = 90$ [mm] and a lens permittivity of $\varepsilon_r = 10$. The closest surface match is obtained for $d = 1.03$ and is depicted in Figure 10. The corresponding elliptical extension ratio is $L_E / R_{lens} = 0.4290$.

Summarizing the discussion in this section, the advantages of using a substrate lens are three-fold:

1. By varying the shape of the lens, the pattern gain can be increased up to the diffraction limit of the lens aperture.
2. By simulating a dielectric half-space, the front-to-back ratio is improved to $\varepsilon_r^{3/2}$:1 for slots.
3. Again, by simulating a dielectric half-space, substrate modes are suppressed.

2.3 A Review of Dielectric Resonator Antennas

A dielectric resonator (DR) consists of a high permittivity, three dimensional dielectric structure that is electromagnetically coupled to a microwave circuit [37]. The shape and size of the dielectric is chosen so that it supports specific resonant modes to which energy is coupled [38]. If the permittivity of the DR is high (~100), its required physical size is very small relative to a free-space wavelength. The resulting electromagnetic field outside the DR is quasistatic and very little radiation occurs. Dielectric resonators are therefore good energy storage devices.

By lowering the permittivity ($5 \leq \varepsilon_r \leq 20$), the DR becomes an efficient radiator [39]. The Dielectric Resonator Antenna (DRA) is an attractive radiator at millimeter wave frequencies, since the lack of metallic surfaces (excepting the supporting ground plane) reduces conductor losses. Indeed, measured radiation efficiencies greater than 98% have been reported [40]. DRAs can be cylindrical [39,41-44], rectangular [45,46], hemispherical [47-51], or half-cut cylinders [52,53]. Energy is coupled directly into the DRA by using either probe, microstrip, or slot excitation. In fact, slot-coupled hemispherical DRAs [48,51] have exactly the same geometry as hemispherical Substrate Lens Antennas (SLAs).

Interestingly, the radiation pattern of a slot-coupled hemispherical DRA resonating at its fundamental TE_{111} mode [48] closely resembles the radiation pattern of a slot antenna [54], which is the expected result if this geometry is analysed using ray optics: the hemispherical lens does not alter the slot's radiation pattern because it does not refract the rays. Note that this is an observation only: it will be shown later that ray optics cannot be used to analyse DRAs. It is also interesting to note that the input impedances of the slot-coupled DRAs in [48] are somewhat similar to the input impedances of slot antennas on semi-infinite dielectrics [3], although the resonances are not identical.

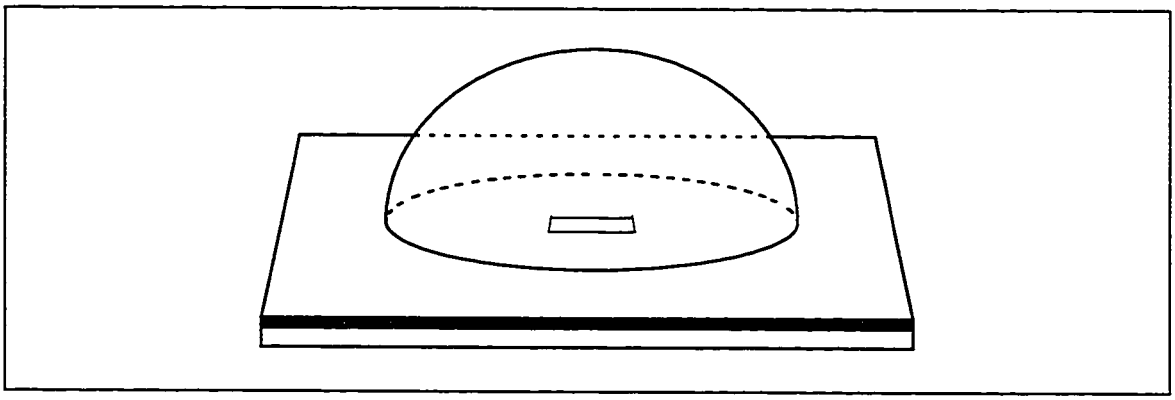

Figure 11: Slot-Coupled DRA on a Ground Plane

The primary differences that exist between DRAs and SLAs are: their physical size, their radiation pattern, and the methods used to analyse them. Lenses are usually made electrically large so that the ray approximation that is used in their analysis is valid. By varying the extension lengths of SLAs, the gain of their radiation patterns can be increased. By contrast, hemispherical DRA radiation patterns are typically quite broad. Table 1 lists several extended hemispherical lenses used with various feed antennas. The variable '*distance*' is computed as the sum of the lens' extension length and of the lens' radius ($L_E + R_{lens}$), and the variable λ_d is the wavelength inside the dielectric: $\lambda_d = \frac{\lambda_0}{\sqrt{\varepsilon_r}}$. Observe that the dielectric-to-air interface is generally several wavelengths away from the radiator.

Reference	Lens Permittivity	Frequency [GHz]	$(distance)/\lambda_0$	$(distance)/\lambda_d$
[34]	11.7	20	0.847	2.90
[19]	3.8	100	1.63	3.18
[32]	11.7	100	2.29	7.82
[18]	11.7	10	4.03	8.77
[23]	3.8	115	4.07	7.94
[25]	11.7	94	5.12	17.5
[14]	11.7	250	5.71	19.5
[13]	11.7	246	7.81	26.7
[16]	2.13	50	8.33	12.16

Table 1: Documented Extended Hemispherical SLA Permittivities, Frequencies, and Sizes

Table 2 lists various parameters of published probe- and slot-coupled hemispherical DRAs. The radius of the hemisphere, R_{DRA}, is chosen so that only the fundamental mode is excited within the structure. This radius, which is typically a fraction of a wavelength away from the radiating element, is much smaller than that of an SLA.

Reference	DRA Permittivity	Frequency [GHz]	R_{DRA} / λ_0	R_{DRA} / λ_d
[48]	6.49	1.375	0.136	0.347
[55]	9.8	3.57	0.150	0.464
[48]	8.9	1.835	0.155	0.463
[51]	9.5	5.5	0.160	0.480
[47]	8.9	1.89	0.161	0.480

Table 2: Documented Hemispherical DRA Permittivities, Operating Frequencies, and Sizes

DRA analysis relies on a moment method solution to an integral equation formulation that will be explained in a later section. It is well worth noting that ray optics are never used to study DRAs, as the small electrical size of the DRA prohibits the use of ray approximations.

3. Analysis Methods

In this chapter, existing analysis methods for SLAs are reviewed. The limitations of the Geometrical Optics hybrid method are exposed and compared to the requirements for simulating electrically small SLAs. An improved simulation technique is required, and various analysis methods are studied as possible candidates for use in the new simulator. The chapter concludes by revealing the selected analysis method.

3.1 Existing Analysis Methods for SLAs

Analytical methods for simulating SLAs are recent developments [2,13,18,23,24]. Most consist of a hybrid Geometrical Optics (GO) approach in which the first step is the illumination of the inner surface of the lens. Ray tracing is used for this purpose, where the strength of the rays is weighted by the feed antenna's known electric far-field pattern. Next, this electric field is decomposed into its TE and TM modes at the lens-to-air boundary. The Fresnel transmission and reflection formulae [56] are then applied at this boundary to obtain the reflected and transmitted electric fields. Finally, the transmitted electric field is converted into equivalent sheet currents [57,pp.575-580] on the outside of the lens, allowing the far-field pattern of the SLA to be calculated using standard far-field integration over the lens' outer surface. This last step constitutes the "hybrid" part of the GO method.

Filipovic *et al.* [13] use the hybrid GO technique to study extended hemispherical lenses fed by a double slot antenna array. The elements are intended for use in a quasi-optical [58,59] focused beam imaging array operating at 246 GHz. The emphasis of the paper is therefore placed on analysing the Gaussian beam coupling efficiency [1,p.1766] of the antenna. Raman and Rebeiz [25] use the same technique to study extended hemispherical lenses fed by slot-ring antennas and arrays.

Büttgenbach [23] uses a ray tracing technique to analyse extended hemispherical lenses fed by a spiral antenna, but details concerning the analysis method are not disclosed. The device is slated for use as a radio telescope receiver imaging array element operating at 115 GHz.

Masarweh *et al.* [18] and Sherer [60] have investigated hyperhemispherical lenses for 10 GHz slot ring mixers. Their analysis approach is slightly different from the one previously described. Although the fields transmitted through the lens are again determined by ray tracing, the exiting rays are subsequently traced to a plane situated at the apex of the lens. In doing so, the SLA is reduced to an equivalent aperture antenna. A spectral domain Fourier-transform [57,pp.620-625] is then applied to the aperture fields to obtain the antenna's far-field radiation patterns.

3.2 Limitations of the Hybrid GO Analysis Method and Improvements

There are several factors restricting the use of the hybrid GO analysis method. First among these is that the far-field radiation pattern of the feed antenna must be known to properly weight the rays illuminating the lens. The use of this *a priori* knowledge restricts the designer's choice of feed antennas to those that have been analytically or numerically solved.

Second, the lens illumination technique must surely fail as the physical dimensions of the lens are reduced. As the radius of the lens is decreased, the far-field pattern of the feed antenna no longer accurately describes the radiation arriving on the inside surface of the lens. Phase, amplitude, and vector orientation errors are expected to become prominent as the lens-to-air boundary enters the near-field region of the feed antenna.

The third restriction of the GO hybrid technique is that it ignores the energy that is internally reflected at the lens-to-air boundary. This reflected power is often quoted as a reflection loss and subsequently ignored. Although the reflection can be reduced by covering the lens with a quarter-

wave matching layer [12], the reflected power will always affect the radiation pattern of the SLA to a certain degree. Some of the reflected radiation will be absorbed by the feed antenna through reaction, but the remainder must eventually exit the lens at some other point, thereby modifying the radiation pattern in an unpredictable way. Lenses with no matching layer are the most prone to these errors.

The first two restrictions of the hybrid GO technique can be lifted by improving the method that is used to illuminate the lens. What is required is to replace the simple ray tracing by a multi-purpose field propagator that is flexible enough to accommodate variations of:

- the type of feed element,
- the physical orientation of the feed element, and
- the number of feed elements and their array configurations.

This propagator should output precise field values, including amplitude, orientation and phase, regardless of the radial distance from the feed elements. In other words, it must be valid in both the near- and far-field regions of the feed antennas. In light of the thesis motivation, the following discussion will be limited to propagators that are suitable for slot feed antennas.

3.3 Propagator Candidates

Slot antenna radiation can be calculated using many different methods. The following is a summary of several competing techniques.

3.3.1 Fourier Optics: A Scalar Wave Theory

This general analysis method uses two-dimensional spatial Fourier transforms to predict the radiated fields from apertures [61]. Although powerful, this method will be proven to be inadequate for lens illumination, as it fails to meet the criteria specified in Section 3.3 .

As with all physical solutions, the Fourier Optics method begins with Maxwell's equations and assumes that the waves are propagating in a medium that is: a dielectric, free of charge, linear, isotropic, homogeneous, non-dispersive, and non-magnetic. Under these conditions, the free-space Helmholtz wave equations for both the electric and magnetic fields are obtained:

$$\bar{\nabla}^2\bar{E} + k^2\bar{E} = 0 \quad \text{and} \quad \bar{\nabla}^2\bar{H} + k^2\bar{H} = 0\,, \tag{3-1}$$

where the fields are assumed to be time-harmonic with their time phasors rotating in a clockwise direction. The complete E-field expression is therefore written as:

$$\bar{\mathcal{E}}(P,t) = \mathrm{Re}\left\{\bar{E}(P)\exp(-j2\pi\omega t)\right\}. \tag{3-2}$$

The variable P denotes the observation point in space. The Helmholtz equations can be written out in Cartesian coordinates:

$$\hat{x}\nabla^2 E_x + \hat{y}\nabla^2 E_y + \hat{z}\nabla^2 E_z + k^2\left(\hat{x}E_x + \hat{y}E_y + \hat{z}E_z\right) = 0\,, \tag{3-3}$$

where the scalar Laplacian is defined as:

$$\nabla^2 A \equiv \frac{\partial^2 A}{\partial x^2} + \frac{\partial^2 A}{\partial y^2} + \frac{\partial^2 A}{\partial z^2}\,. \tag{3-4}$$

Since all of the spatial components of the two fields must obey the same equation, by assuming that the fields are uncoupled, the two vector Helmholtz wave equations can be replaced by a single scalar equation:

$$\left(\nabla^2 + k^2\right)U(P) = 0, \tag{3-5}$$

where the symbol U, in Cartesian coordinates, may represent either of the six components: E_x, E_y, E_z, H_x, H_y or H_z, at an observation point P. The development given above is the foundation for Fourier Optics and suffices for the analysis that follows. The complete derivation of Fourier Optics is given in Reference [61].

Since the fields in a slot antenna can be specified *a priori*, the Fourier Optics development seems to apply to the propagation problem at hand. However, it does not; and this will become evident after considering the implications of reducing the problem to a scalar one.

Consider a slot antenna cut in a ground plane, which has its longest side L_S oriented in the $\hat{x}$ direction, as illustrated in Figure 12.

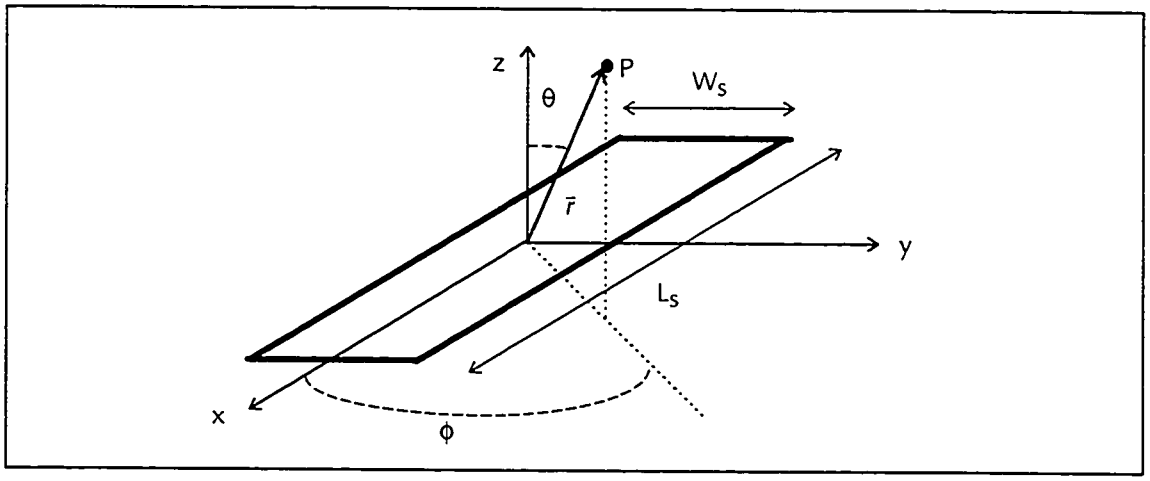

Figure 12: Slot Antenna Geometry

Let the electric field in the slot be uniformly oriented in the $+\hat{y}$ direction over the aperture:

$$\bar{E}_s = \hat{y}E_0, \qquad -L_S/2 \le x \le L_S/2, \qquad -W_S/2 \le y \le W_S/2. \tag{3-6}$$

The complete analytical far-field pattern of this slot, obtained at point P by the far-field Spectral Domain method, is the following [57,pp.586-588]:

$$\begin{aligned} E_x &= 0 \\ E_y &= j\frac{L_S W_S k E_0 e^{-jkr}}{2\pi r}\cos\theta\,\mathrm{sinc}\left(\frac{xkL_S}{2\pi r}\right)\mathrm{sinc}\left(\frac{ykW_S}{2\pi r}\right) \\ E_z &= -j\frac{L_S W_S k E_0 e^{-jkr}}{2\pi r}\sin\theta\sin\phi\,\mathrm{sinc}\left(\frac{xkL_S}{2\pi r}\right)\mathrm{sinc}\left(\frac{ykW_S}{2\pi r}\right), \end{aligned} \tag{3-7}$$

where k is the wavenumber and $r = |\bar{r}|$. Observe that the original source field, oriented uniquely in the y direction, has not only produced a y component in the far-field, but a z component as well. Returning to the analytical derivations of the Fourier Optics method, a similar source field would result in the following equations:

$$\begin{aligned} \nabla^2 E_x + k^2 E_x = 0 \quad &\rightarrow E_x = 0 \\ \nabla^2 E_y + k^2 E_y = 0 \quad & \\ \nabla^2 E_z + k^2 E_z = 0 \quad &\rightarrow E_z = 0 \ . \end{aligned} \tag{3-8}$$

The E_x and E_z components are nil because these fields do not exist in the aperture. Hence we see the effect of the scalar equations: coupling between the components has been eliminated.

The Fourier Optics derivation fails to predict the z component of the far-field. And yet these derivations follow directly from Maxwell's equations! The obvious source of the error is that the field components are uncoupled. Equation (3-7) clearly shows that this is false, as an initial electric field oriented along the y-axis produces both y- and z-directed components in the far-field.

The complete derivation of the Fourier Optics method builds upon the scalar Helmholtz wave equation. These derivations will not be included here because the primary assumption used in this theory —that the fields are uncoupled— renders the method incapable of predicting the total fields radiated from the aperture.

3.3.2 Spectral Domain Method

A more robust form of Fourier transform analysis can be applied to finite aperture antennas mounted on infinite ground planes [57,pp.620-630]. The Fourier Optics technique requires that Maxwell's equations be decoupled and that the propagation phenomenon be intuitively deduced before the equations are reduced to a simple Fourier transform [61,p.74]. The more robust form, hereafter referred to as simply the Spectral Domain Method, does not require these initial assumptions. Rather, this theory *begins* by assuming that a monochromatic radiated wave, observed at any point, can be decomposed into a superposition of plane waves. These plane waves, all evaluated at the same observation point, have the same angular frequency, but have different amplitudes and travel in different directions. They are expressed as:

$$\bar{f}\left(k_x,k_y\right)e^{-j\bar{k}\cdot\bar{r}}, \tag{3-9}$$

where $\bar{k}$ is the vector wavenumber, $\bar{k}=\hat{x}k_x+\hat{y}k_y+\hat{z}k_z$, and $\bar{r}$ is the radial vector from the origin, $\bar{r}=\hat{x}x+\hat{y}y+\hat{z}z$. Note that $\bar{f}\left(k_x,k_y\right)$ is the vector amplitude of the wave and has been formulated to be a function of only the k_x and k_y directors. The electric field at the observation point can thus be written as:

$$\bar{E}(x,y,z)=\frac{1}{4\pi}\int_{-\infty}^{\infty}\int_{-\infty}^{\infty}\left[\bar{f}\left(k_x,k_y\right)e^{-jk_zz}\right]e^{-j\left(k_xx+k_yy\right)}dk_xdk_y, \tag{3-10}$$

where the $1/4\pi$ factor has been added so that this formulation agrees exactly with a common derivation of the two-dimensional Fourier transform. This expression of the electric field is in fact a two-dimensional Fourier transform of the expression in square brackets, which must therefore be equal to the inverse Fourier transform of the electric field:

$$\bar{f}\left(k_x,k_y\right)e^{-jk_zz}=\mathcal{F}_{2D}^{-1}\left\{\bar{E}(x,y,z)\right\}. \tag{3-11}$$

This alone is no great revelation; however, the knowledge of this inverse Fourier transform at $z = 0$ (in the aperture) is sufficient to predict the field at any point in space. The only assumption is that the z variations of the two-dimensional inverse Fourier transform of the electric field are uncoupled. The result is that two double integrals must be performed over the aperture field to find $\bar{f}\left(k_x,k_y\right)$ [57,pp.624-625]. A further double integral with infinite bounds (the Fourier transform) is then required to find the electric field at any point in space. Although a computer simulation based on this technique seems feasible, it will be left as future work, as a third propagation technique has been chosen. Further, the implications of uncoupling the z variations of Equation (3-11) require more study.

3.3.2.1 Fourier Optics - A Special Case of the Spectral Domain Method

As an aside, it is interesting to consider the similarities that exist between the two techniques that have been described. In the far-field of a slot antenna, the Fourier Optics results agree with the Spectral Domain Method results, but only for observation points that are close to boresight. This proof has been included in Appendix A.

3.3.3 Physical Optics Method

The underlying principle of Physical Optics (PO) dates back to the seventeenth century, when Christian Huygens was considering the nature of light. Huygens hypothesized that if each point on a spherical wavefront was considered to be a new secondary source of spherical waves, then the wavefront at a later time could be obtained by summing the contributions from these secondary sources. This hypothesis has since been given a rigorous mathematical foundation. One of many possible examples is Schelkunoff's equivalence principle [57,pp.575-580], in which the fields on an equivalent surface are replaced by equivalent magnetic and electric current densities. These currents are then considered as secondary sources.

The PO technique is also based on Huygen's wave principle. The theory that will be presented here is a full vectorial propagator based on the work of Diaz and Milligan [62]. This theory begins with Maxwell's equations for both magnetic and electric source currents [63]:

$$\begin{aligned} \bar{\nabla} \times \bar{E} &= -j\omega\mu\bar{H} - \bar{M} \\ \bar{\nabla} \times \bar{H} &= j\omega\varepsilon\bar{E} + \bar{J} \\ \bar{\nabla} \cdot \mu\bar{H} &= \rho_m \\ \bar{\nabla} \cdot \varepsilon\bar{E} &= \rho_e \,, \end{aligned} \tag{3-12}$$

where $\bar{J}$ and $\bar{M}$ are electric and magnetic current densities [A/m^2], respectively, and ρ_e and ρ_m are electric and magnetic volume charge densities [C/m^3], respectively.

The ultimate goal is to derive a relationship between the field vectors and the source vectors. Such a relationship is called the dyadic Green's function [64,65]. It consists of a 3x3 matrix, here denoted by an underlined variable ($\underline{G}$). The Green's function can be regarded as the impulse response of the space surrounding the antenna. Whereas the Fourier Optics technique assumes that the fields are not coupled, the PO technique does not.

Assume a discrete electric source current sample point, $\bar{J}(\bar{r}')$, located at $\bar{r}'$. By using the dyadic Green's function, the resulting electric and magnetic fields at the observation point $\bar{r}$ due to this current sample can be expressed as:

$$\begin{aligned} \bar{E}_e(\bar{r},\bar{r}') &= -\underline{G_{EJ}}(\bar{r},\bar{r}')\bullet\bar{J}(\bar{r}') \\ \bar{H}_e(\bar{r},\bar{r}') &= -\underline{G_{HJ}}(\bar{r},\bar{r}')\bullet\bar{J}(\bar{r}'), \end{aligned} \tag{3-13}$$

where the subscript on the fields indicates that they are due to an electric source, and the subscripts on the Green's functions identify the different Green's functions (i.e. *EJ* signifies "electric field due to electric source"). Note that the notation used does *not* indicate a dot product between two vectors, but rather a common matrix multiplication:

$$\underline{G_{EJ}}(\bar{r},\bar{r}')\bullet\bar{J}(\bar{r}') \equiv \begin{bmatrix} G_{EJxx}(\bar{r},\bar{r}') & G_{EJxy}(\bar{r},\bar{r}') & G_{EJxz}(\bar{r},\bar{r}') \\ G_{EJyx}(\bar{r},\bar{r}') & G_{EJyy}(\bar{r},\bar{r}') & G_{EJyz}(\bar{r},\bar{r}') \\ G_{EJzx}(\bar{r},\bar{r}') & G_{EJzy}(\bar{r},\bar{r}') & G_{EJzz}(\bar{r},\bar{r}') \end{bmatrix} \begin{bmatrix} J_x(\bar{r}') \\ J_y(\bar{r}') \\ J_z(\bar{r}') \end{bmatrix}. \tag{3-14}$$

Vector dot products will be denoted by a small dot ($\cdot$). Similar to vectors, dyadics satisfy a number of mathematical identities [66], some of which will be required in subsequent derivations.

Two other impulse response relations exist that account for magnetic current sources:

$$\begin{aligned} \bar{H}_m(\bar{r},\bar{r}') &= -\underline{G_{HM}}(\bar{r},\bar{r}')\bullet\bar{M}(\bar{r}') \\ \bar{E}_m(\bar{r},\bar{r}') &= -\underline{G_{EM}}(\bar{r},\bar{r}')\bullet\bar{M}(\bar{r}'). \end{aligned} \tag{3-15}$$

Following this logic, the total fields at the observation point are found by integrating over all of the source contributions:

$$\begin{aligned}\bar{E}(\bar{r}) &= -\iiint_{V'} \underline{G_{EJ}}(\bar{r},\bar{r}') \bullet \bar{J}(\bar{r}')dV' - \iiint_{V'} \underline{G_{EM}}(\bar{r},\bar{r}') \bullet \bar{M}(\bar{r}')dV' \\ \bar{H}(\bar{r}) &= -\iiint_{V'} \underline{G_{HJ}}(\bar{r},\bar{r}') \bullet \bar{J}(\bar{r}')dV' - \iiint_{V'} \underline{G_{HM}}(\bar{r},\bar{r}') \bullet \bar{M}(\bar{r}')dV' .\end{aligned} \tag{3-16}$$

The actual derivation of the four dyadic Green's functions is quite lengthy and will be performed at a later time. Suffice to say that these functions can be derived in such a way as to predict both the near- and far-fields of the sources. Furthermore, this technique can accommodate any source geometry, as is indicated by the general nature of the volume integrals in Equation (3-16).

3.3.4 Moment Method Solutions for DRAs

SLAs and hemispherical DRAs possess a striking resemblance to one another, as shown in Section 2.3 . Indeed, hemispherical SLAs and DRAs differ only by their relative size. Therefore, it is wise to review the analysis method that is used for DRAs, as it may also prove to be useful in the analysis of electrically small SLAs.

The moment method is a general numerical technique [67] in which an electromagnetic problem is formulated as a functional equation similar to Equation (3-16) and then reduced to a matrix equation. This matrix equation is solved by using known numerical techniques. Note that the moment method is not a one-way propagator like those that have been previously described. So-called one-way propagators assume that the source current is known and is not affected by reaction. The moment method can be used to predict accurately the effects of reflected fields and mutual coupling of the sources. The primary advantage of a moment method solution to an integral equation is that it not only provides the radiated fields but also an approximation of the exact source current. This current may then be used to calculate the input impedance of the antenna.

The moment method solution to an integral equation has been the technique of choice for characterising DRAs [41,48,49,52,55,68-71]. Contrary to the hybrid technique used to analyse substrate lens antennas, the boundary conditions at the dielectric-to-air interface are included in the derivation of the *exact* Green's functions for the structure. One Green's function is used within the bounds of the dielectric and includes both the boundary conditions at the source and the boundary conditions at the interface. A second Green's function is used for the space outside the dielectric and is matched to the first Green's function at the interface. The integral equation is then expressed in the following general form:

$$\bar{E}(\bar{r},\bar{r}') = \iiint_{V'} \underline{G}(\bar{r},\bar{r}') \bullet \bar{J}(\bar{r}') dV' \,. \qquad \textbf{(3-17)}$$

The moment method is therefore a superior analysis tool, using exact propagators (i.e. Green's functions) that must be already known. However, there are still two unknown quantities in Equation (3-17): $\bar{E}(\bar{r},\bar{r}')$ (the field vector), and $\bar{J}(\bar{r}')$ (the source current). Depending on the location of the radiator within the DR, the electric (or magnetic) field near the radiator can be approximated by the electric (or magnetic) field of a known mode within the DR [26]. Hence the placement of the radiator depends on the desired mode to which coupling is desired. The source current is then solved by applying the method of moments. The radiation pattern can then be calculated by again using the Green's functions.

The one drawback of this technique is that several modes can exist in a dielectric resonator and they will all couple, to a certain degree, to the source. In fact, [48,p.20]:

> *" real excitation mechanisms excite other, undesired, higher-order modes, which disturb the field distribution and, hence, affect the computation of the input impedance and the far-field radiation pattern. Therefore, all modes must be considered in the computation of the far-field radiation pattern, as well as in computation of the input impedance, for accurate prediction of these quantities ".*

Different electric fields are associated with these higher order modes. Their effects may be determined independently of one another by substituting a mode's electric field in Equation (3-17) [49]. However, the total contributions from all of the modes taken together is difficult to predict.

3.4 Propagator Selection

To select the appropriate propagator, the type of analysis to be performed must be considered. The full characterisation of the device at hand is ideally sought. For the case of the slot fed lens, this implies that both the input impedance and the radiation pattern are desired.

The only technique, among those described, that is capable of generating both of these values is the moment method solution to the DRA integral equation. Is this solution readily applicable to extended hemispherical lenses of various radii? To successfully apply the moment method, the following are required before the integral equation can be solved:

- the exact dyadic Green's function solution to the extended hemisphere geometry,
- the dielectric resonator modes sustained by this geometry, and,
- a method to include the effects of higher order DR modes that exist when the lens radius is large enough to support these modes.

After assessing these requirements and the time constraint imposed to complete this Master's thesis, the decision was made not to pursue the method of moments solution. The reasons are listed below.

- Formulating the exact dyadic Green's function for the structure alone is a formidable task.
- Dielectric resonator modes for the structure are not available and would have to be derived.
- A method to include higher order modes would also have to be derived.

The analysis of extended hemispherical DRAs is therefore left as future work.

Examination of the remaining propagators reveals that a hybrid analysis will be required. A propagator is therefore required to illuminate the lens. However, some of the mentioned propagators have been proven to be inadequate. The first of these is the use of standard far-field expressions to illuminate the lens. As previously stated, far-field expressions may not be accurate for illuminating electrically small lenses. The Fourier Optics technique cannot be applied either, for it only yields far-field values at boresight.

The remaining propagators are the Physical Optics technique and the Spectral Domain formulation. Given the time restrictions and the immediate availability of PO code, the PO technique has been chosen as the propagator for this thesis. Since the derivation of the exact Green's function for extended hemispherical lenses has been left as future work, the free-space dyadic Green's function will be used to illuminate the lens.

4. Physical Optics Hybrid Simulation Technique

Chapter Four is devoted to the study of the PO hybrid simulation technique. The chapter begins with the mathematical derivation of the free-space dyadic Green's functions, and follows with the description of the simulator algorithm. The approximations of the hybrid analysis are then considered along with their impact on the simulated results. The chapter concludes with an analysis of the minimum lens radius that can be accurately simulated using this technique.

4.1 Physical Optics Derivation of the Free-Space Dyadic Green's Functions

The integral equations describing the radiated electromagnetic fields due to electric and magnetic current densities are given in Equation (3-16). The four dyadic free-space Green's functions for impulse excitations are now derived. Although it is true that this particular development is only strictly valid in free-space, the resulting equations can be modified for use in a dielectric medium (i.e. in the lens) by substituting the permittivity of free-space, ε_0, with the permittivity of the lens, ε.

This derivation closely follows that which is found in [62, Appendix A]. However, the lengthy proofs are not provided therein, and are given instead in Appendix B of this document. Using Equations (3-13) and (3-15) in Maxwell's equations (3-12), the following expressions are obtained:

$$
\begin{aligned}
&j\omega\varepsilon\underline{G_{EJ}}(\bar{r},\bar{r}')\bullet\bar{J}(\bar{r}')-\bar{\nabla}\times\left[\underline{G_{HJ}}(\bar{r},\bar{r}')\bullet\bar{J}(\bar{r}')\right]=\bar{J}(\bar{r}')\delta(\bar{r}-\bar{r}')\\
&j\omega\mu\underline{G_{HM}}(\bar{r},\bar{r}')\bullet\bar{M}(\bar{r}')+\bar{\nabla}\times\left[\underline{G_{EM}}(\bar{r},\bar{r}')\bullet\bar{M}(\bar{r}')\right]=\bar{M}(\bar{r}')\delta(\bar{r}-\bar{r}')\\
&j\omega\mu\underline{G_{HJ}}(\bar{r},\bar{r}')\bullet\bar{J}(\bar{r}')+\bar{\nabla}\times\left[\underline{G_{EJ}}(\bar{r},\bar{r}')\bullet\bar{J}(\bar{r}')\right]=\bar{0}\\
&j\omega\varepsilon\underline{G_{EM}}(\bar{r},\bar{r}')\bullet\bar{M}(\bar{r}')-\bar{\nabla}\times\left[\underline{G_{HM}}(\bar{r},\bar{r}')\bullet\bar{M}(\bar{r}')\right]=\bar{0}\,.
\end{aligned}
\tag{4-1}
$$

The source currents can be factored out of Equation (4-1), yielding the following set of scalar equations grouped into dyads:

$$
\begin{aligned}
j\omega\varepsilon\underline{G}_{EJ}(\bar{r},\bar{r}') - \bar{\nabla}\times\underline{G}_{HJ}(\bar{r},\bar{r}') &= \underline{1}\,\delta(\bar{r}-\bar{r}') \\
j\omega\mu\underline{G}_{HM}(\bar{r},\bar{r}') + \bar{\nabla}\times\underline{G}_{EM}(\bar{r},\bar{r}') &= \underline{1}\,\delta(\bar{r}-\bar{r}') \\
j\omega\mu\underline{G}_{HJ}(\bar{r},\bar{r}') + \bar{\nabla}\times\underline{G}_{EJ}(\bar{r},\bar{r}') &= \underline{0} \\
j\omega\varepsilon\underline{G}_{EM}(\bar{r},\bar{r}') - \bar{\nabla}\times\underline{G}_{HM}(\bar{r},\bar{r}') &= \underline{0}\,.
\end{aligned}
\tag{4-2}
$$

The symbol $\underline{1}$ represents the unit dyad (the identity 3x3 matrix), whereas $\underline{0}$ represents the null dyad (the null 3x3 matrix). Note that (4-2) no longer depends on the current densities, and therefore represents the nature of free-space propagation. Also note that the two last equations relate $\underline{G}_{EJ}(\bar{r},\bar{r}')$ and $\underline{G}_{HM}(\bar{r},\bar{r}')$ to the other two dyadic Green's functions:

$$
\begin{aligned}
\underline{G}_{HJ}(\bar{r},\bar{r}') &= -\frac{1}{j\omega\mu}\bar{\nabla}\times\underline{G}_{EJ}(\bar{r},\bar{r}') \\
\underline{G}_{EM}(\bar{r},\bar{r}') &= \frac{1}{j\omega\varepsilon}\bar{\nabla}\times\underline{G}_{HM}(\bar{r},\bar{r}')\,.
\end{aligned}
\tag{4-3}
$$

Therefore only $\underline{G}_{EJ}(\bar{r},\bar{r}')$ and $\underline{G}_{HM}(\bar{r},\bar{r}')$ need to be derived explicitly. By substituting the first line of Equation (4-3) into the first line of Equation (4-2), and by using the dyadic identity $\bar{\nabla}\times\bar{\nabla}\times\underline{A} = \bar{\nabla}\bar{\nabla}\bullet\underline{A} - \bar{\nabla}^2\underline{A}$, the following equation is obtained (see Appendix B.1):

$$
\bar{\nabla}\bar{\nabla}\bullet\underline{G}_{EJ}(\bar{r},\bar{r}') - \bar{\nabla}^2\underline{G}_{EJ}(\bar{r},\bar{r}') - k^2\underline{G}_{EJ}(\bar{r},\bar{r}') = j\omega\mu\underline{1}\,\delta(\bar{r}-\bar{r}')\,. \tag{4-4}
$$

By using a similar derivation for $\underline{G}_{HM}(\bar{r},\bar{r}')$, the following equation results:

$$
\bar{\nabla}\bar{\nabla}\bullet\underline{G}_{HM}(\bar{r},\bar{r}') - \bar{\nabla}^2\underline{G}_{HM}(\bar{r},\bar{r}') - k^2\underline{G}_{HM}(\bar{r},\bar{r}') = j\omega\varepsilon\underline{1}\,\delta(\bar{r}-\bar{r}')\,. \tag{4-5}
$$

Equations (4-4) and (4-5) differ by a constant; therefore only one requires explicit derivation. By expanding $-k^2 = j\omega\mu(j\omega\varepsilon)$, and by using the same dyadic identity, Equation (4-4) is rewritten as:

$$
j\omega\varepsilon\underline{G}_{EJ}(\bar{r},\bar{r}') + \bar{\nabla}\times\bar{\nabla}\times\underline{G}_{EJ}(\bar{r},\bar{r}')\left(\frac{1}{j\omega\mu}\right) = \underline{1}\,\delta(\bar{r}-\bar{r}')\,. \tag{4-6}
$$

By taking the divergence of Equation (4-6), and noting that $\bar{\nabla}\bullet\bar{\nabla}\times\underline{A} \equiv 0$, the following is obtained:

$$
j\omega\varepsilon\bar{\nabla}\bullet\underline{G}_{EJ}(\bar{r},\bar{r}') = \bar{\nabla}\bullet\left[\underline{1}\,\delta(\bar{r}-\bar{r}')\right] = \bar{\nabla}\left[\delta(\bar{r}-\bar{r}')\right]. \tag{4-7}
$$

Substitution of Equation (4-7) into the first term of Equation (4-4) results in Equation (4-8):

$$\bar{\nabla}\left(\frac{\bar{\nabla}\delta(\bar{r}-\bar{r}')}{j\omega\varepsilon}\right)-\left(\bar{\nabla}^2+k^2\right)\underline{G_{EJ}}(\bar{r},\bar{r}')=j\omega\mu\underline{1}\,\delta(\bar{r}-\bar{r}'). \tag{4-8}$$

Rearranging,

$$\underline{G_{EJ}}(\bar{r},\bar{r}')=-j\omega\mu\left(\underline{1}+\frac{\bar{\nabla}\bar{\nabla}}{k^2}\right)\frac{\delta(\bar{r}-\bar{r}')}{\left(\bar{\nabla}^2+k^2\right)}. \tag{4-9}$$

The term $g(\bar{r}-\bar{r}')=-\dfrac{\delta(\bar{r}-\bar{r}')}{\bar{\nabla}^2+k^2}$ is a scalar quantity because the numerator is a scalar. Hence the argument $(\bar{r}-\bar{r}')$ can be replaced by $R=|\bar{r}-\bar{r}'|$.

The solution of the equation:

$$\left(\bar{\nabla}^2+k^2\right)g(R)=-\delta(R)$$

is $g(R)=\dfrac{e^{-jkR}}{4\pi R}$, which is also known as the scalar free-space Green's function. As a result, the equations for the electric-electric and magnetic-magnetic dyadic Green's functions become:

$$\underline{G_{EJ}}(\bar{R})=j\omega\mu\left(\underline{1}+\frac{\bar{\nabla}\bar{\nabla}}{k^2}\right)g(R) \qquad \text{and} \qquad \underline{G_{HM}}(\bar{R})=j\omega\varepsilon\left(\underline{1}+\frac{\bar{\nabla}\bar{\nabla}}{k^2}\right)g(R). \tag{4-10}$$

The differential operators in Equation (4-10) can be eliminated by using the lengthy derivations that have been included in Appendix B.2 . The resulting four dyadic Green's functions are the following:

$$\begin{aligned}
\underline{G_{EJ}}(\bar{R})&=j\omega\mu\frac{e^{-jkR}}{4\pi R}\left[\left(\underline{1}-\hat{R}\hat{R}\right)\left(1-\frac{1}{k^2R^2}-j\frac{1}{kR}\right)+\hat{R}\hat{R}\left(\frac{2}{k^2R^2}+j\frac{2}{kR}\right)\right]\\
\underline{G_{HM}}(\bar{R})&=j\omega\varepsilon\frac{e^{-jkR}}{4\pi R}\left[\left(\underline{1}-\hat{R}\hat{R}\right)\left(1-\frac{1}{k^2R^2}-j\frac{1}{kR}\right)+\hat{R}\hat{R}\left(\frac{2}{k^2R^2}+j\frac{2}{kR}\right)\right]\\
\underline{G_{HJ}}(\bar{R})&=\left(\frac{1}{R}+jk\right)\frac{e^{-jkR}}{4\pi R}\hat{R}\times\underline{1}\\
\underline{G_{EM}}(\bar{R})&=-\left(\frac{1}{R}+jk\right)\frac{e^{-jkR}}{4\pi R}\hat{R}\times\underline{1}.
\end{aligned} \tag{4-11}$$

4.2 Hybrid Analysis Using PO Illumination

The lens antennas that are studied in this thesis will be characterised using a more elaborate version of the hybrid GO analysis. Recapping, the first step is the illumination of the inside surface of the lens. Previous authors [13,18,23-25] have used analytical far-field expressions to weight the rays, which limits their analysis to electrically large lenses fed by simple feed configurations. Instead of using far-field expressions to weight the rays, the PO propagators are used to illuminate the lens regardless of its electrical size. The PO propagators predict both the perpendicular and radial components of the fields, and can be used with any source configuration. This thesis represents the first attempt to analyse SLAs using PO propagators.

Once the fields on the inside of the lens are known, a ray approximation is made. In essence, the radiation at the field point is approximated by a local plane wave that is contained in a flux tube. This flux tube originates from the origin, defined as the center of the base of the lens, as illustrated in Figure 13. The validity of this approximation is verified in a later section of this document.

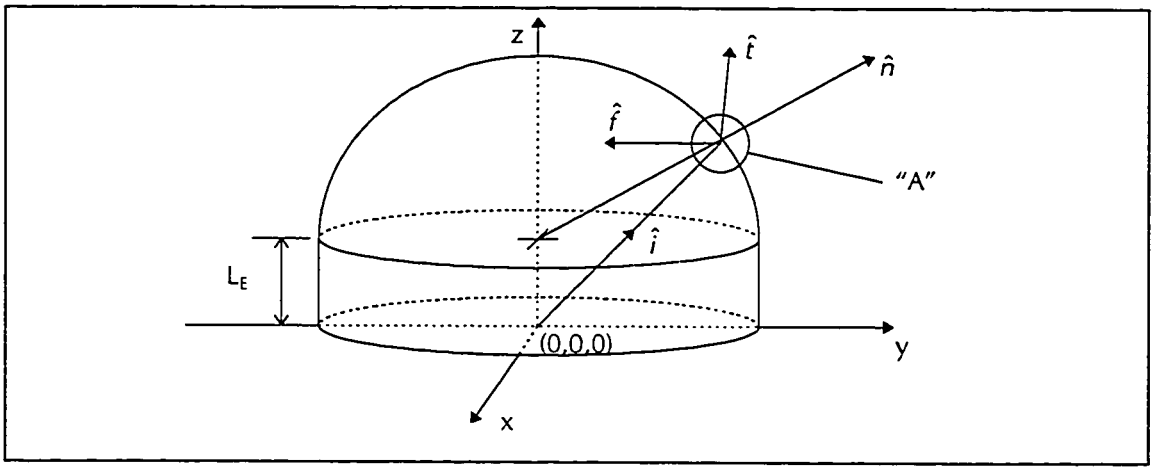

Figure 13: Hybrid Analysis Geometry

By defining an incident ray $\bar{i}$ and a surface normal $\bar{n}$, the Fresnel transmission and reflection equations can be applied at the dielectric-to-air boundary. The circle marked "A" in Figure 13 has been expanded in Figure 14.

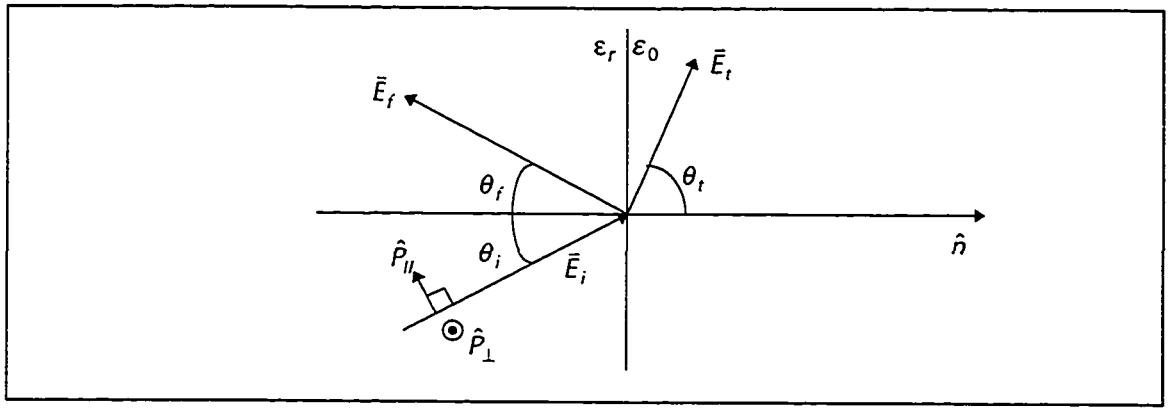

Figure 14: Dielectric-to-Air Boundary

First, the incident electric field $\vec{E}_i$ is decomposed into components that are perpendicular and parallel to the plane of incidence. This operation is accomplished by using the unit vectors defined by [24]:

$$\vec{P}_\perp = \hat{n} \times \hat{i}, \quad \hat{P}_\perp = \frac{\vec{P}_\perp}{\left|\vec{P}_\perp\right|}, \text{ and } \quad \hat{P}_{II} = \hat{P}_\perp \times \hat{i}. \tag{4-12}$$

The TE and TM electric field components are determined by:

$$\vec{E}_{\perp i} = \vec{E}_i \cdot \hat{P}_\perp \quad \text{and} \quad \vec{E}_{IIi} = \vec{E}_i \cdot \hat{P}_{II}. \tag{4-13}$$

The Fresnel transmission and reflection coefficients are then used [56] to obtain the reflected and transmitted electric fields ($\vec{E}_f$ and $\vec{E}_t$, respectively):

$$\vec{E}_f = \Gamma_{II}\vec{E}_{IIi} + \Gamma_\perp \vec{E}_{\perp i} \quad \text{and} \quad \vec{E}_t = \tau_{II}\vec{E}_{IIi} + \tau_\perp \vec{E}_{\perp i}, \tag{4-14}$$

where the coefficients are given by the following equations:

$$\begin{aligned}
\Gamma_\perp &= \frac{\sqrt{\varepsilon_r}\cos\theta_i - \cos\theta_t}{\sqrt{\varepsilon_r}\cos\theta_i + \cos\theta_t} \\
\tau_\perp &= \frac{2\sqrt{\varepsilon_r}\cos\theta_i}{\sqrt{\varepsilon_r}\cos\theta_i + \cos\theta_t} = 1 + \Gamma_\perp \\
\Gamma_{II} &= \frac{\sqrt{\varepsilon_r}\cos\theta_t - \cos\theta_i}{\sqrt{\varepsilon_r}\cos\theta_t + \cos\theta_i} \\
\tau_{II} &= \frac{2\sqrt{\varepsilon_r}\cos\theta_i}{\sqrt{\varepsilon_r}\cos\theta_t + \cos\theta_i} = \frac{(1+\Gamma_{II})\cos\theta_i}{\cos\theta_t}.
\end{aligned} \tag{4-15}$$

The incident, reflected, and transmitted angles are given by:

$$\theta_i = \text{acos}\left(\hat{n}\cdot\hat{E}_i\right), \qquad \theta_r = \theta_i, \text{ and} \qquad \theta_t = \text{acos}\left(\sqrt{1-\varepsilon_r \sin^2\theta_i}\right). \tag{4-16}$$

Once the transmitted fields are obtained, Love's equivalence principle [57,p.577] is used to compute equivalent electric and magnetic sheet currents over the outer surface of the lens. These surface currents are given by:

$$\bar{J}_S = \hat{n}\times\bar{H}_t \text{ and } \bar{M}_S = -\hat{n}\times\bar{E}_t\,. \tag{4-17}$$

The same PO propagators are then used to find the far-field radiation pattern that is produced by these secondary sources.

4.3 Limitations of the Hybrid Analysis

Many approximations are made in the hybrid analysis, and it is important to specify the limitations that they impose. Once these limitations are known, the simulator can be judiciously chosen to analyse appropriate structures.

The most severe approximation is that the free-space Green's function is used inside the lens. An exact Green's function for this structure would include the effects of the boundary conditions at the lens-to-air interface. This is what distinguishes the hybrid technique from an exact technique. An exact dyadic Green's function has been derived for a hemispherical structure using a mode matching method [50]. It is used extensively in the moment method analysis of hemispherical DRAs [49-51]. An exact dyadic Green's function for *extended* hemispheres does not yet exist and would require derivation if it were to be used in this thesis. Judging by the complexity of the work that was performed to solve the hemisphere, the work that would be required to derive such an equation for this project would be formidable and it is not undertaken here. The limitation that this approximation imposes is that the input impedance of the source antenna cannot be predicted. This is obvious since the source currents must be specified *a priori* at the beginning of the analysis.

Another approximation occurs at the dielectric-to-air interface of the lens. The amount of power contained in the reflections at the boundary can be significant due to the impedance mismatch between the dielectric and the air. This reflected, or scattered power will impinge upon the lens surface at other locations and will modify the predicted radiation pattern. Several complicated ray tracing iterations would be required to track all of the reflections. However, the merit of tracking the reflections is uncertain because the source currents must remain undisturbed by these reflections (no reaction). This issue will be treated in Section 5.6 .

The final approximations to be considered are the use of the Fresnel equations at the interface and the ray approximation. The derivation of the Fresnel equations requires the incident radiation to be in the far-field of its source, where the purely transverse electric and magnetic fields are related by:

$$\bar{E}^{FF} = -\frac{1}{Z_d}\hat{n}\times\bar{H}^{FF}, \tag{4-18}$$

with Z_d the intrinsic impedance inside the dielectric. This relation will fail when the radius of the lens is in the near-field, where the $1/R^2$ and $1/R^3$ radial and transverse field components are significant. Further, the ray approximation introduces directional phase errors because it is assumed that the incident ray $\bar{i}$ originates from the center of the slot antenna. The limitations that these approximations impose will be examined in Section 4.5 .

4.4 Slot Currents

The feed antennas that are considered in this thesis are either single slots or double slot arrays. It is assumed that the magnetic current excitation consists of one dominant, single fundamental TE_{10} mode contained in the geometry of Figure 12 and defined by:

$$\bar{M} = \hat{x} M_0 \cos\left(\frac{\pi x'}{L_S}\right), \qquad \begin{cases} -\frac{L_S}{2} \le x' \le \frac{L_S}{2} \\ -\frac{W_S}{2} \le y' \le \frac{W_S}{2} \end{cases}, \tag{4-19}$$

where L_S is the length of the slot and M_0 is a constant. This distribution is also used in [13] and [24]. Although the current distribution is not exact, as the slot feeding mechanism generally causes some variation from Equation (4-19), it should be sufficient for radiation pattern calculations. In fact, a moment method solution of single slots on a semi-infinite dielectric half-space has shown [3] that two entire domain basis functions are sufficient to characterise the slot current; one of which resembles the function defined by Equation (4-19). Also, the use of a single piece-wise sinusoidal mode expansion without edge conditions resulted in impedance data that were very close to those using three or more modes [54]. Further, [62, p.3]:

> *" Small changes in the current distribution cause only secondary changes in the radiation pattern, so it is usually adequate to know the source current approximately".*

4.5 Minimum Lens Radius Analysis

It is desirable to derive a set of bounds over which this simulation technique will be applicable. In particular, the minimum lens radius that can be accurately simulated must be determined. There are two factors that aid in determining this limit, both originating from the approximations that are made at the lens-to-air boundary.

Although the focusing gain of electrically small spherical lenses has been studied in [72], the incident energy on the receiving lens was assumed to be convergent. While this is indeed the case if an objective lens is used in front of the SLA (see Figure 5), this work does not pertain to receiving lenses that are exposed to an incident plane wave.

4.5.1 Validity of the Fresnel Equations

The first limitation is due to the Fresnel reflection and transmission equations. The derivation of the TE and TM equations requires the radial components of the electric and magnetic fields to be negligible. Further, it requires the electromagnetic fields to obey the common far-field relation defined by Equation (4-18); that is, the cross product of the electric and magnetic field vectors must point in the direction of propagation. When this condition fails, the Fresnel equations cease to be valid. The cause of such a failure would be due to the existence of a strong radial component (meaning in the direction of propagation) in either of the two fields. Associated with these radial fields are other differences in the transverse components that are functions of $1/R^2$ and $1/R^3$.

To determine the minimum lens radius where the radial components become significant, the fields radiated by the source are calculated on the inner surface of a hemispherical lens. First, the exact electric field is calculated using the full PO propagator yielding both its radial and transverse components. The far-field approximation of the transverse magnetic field is then calculated using Equation (4-18). Finally. the approximate magnetic field is compared to the exact magnetic field calculated using the magnetic field's PO propagator, allowing any differences to be assesses. The magnitudes of the radial components of the exact E and H fields are also examined.

4.5.2 Wave Vector Direction Ambiguity

The hybrid analysis reduces the slot's incident radiation to a localised plane wave that is contained within a ray tube. Associated to this local plane wave is a wave vector, $\bar{k}_{local}$, that specifies the direction of propagation. This wave vector points in the same direction as the incident vector $\bar{i}$ in Figure 13. For observation points that are far removed from the slot, it can be safely assumed that the ray originates from the center of the slot. However, as the observation point moves closer to the slot, it becomes difficult to pinpoint the origin of the ray. The resulting error in the incident angle θ_i,

defined in Figure 14, will directly affect the transmission and reflection coefficients of Equation (4-15), as well as the reflected and transmitted angles of the rays: θ_i and θ_t, respectively.

Assume that the spatial sampling interval on the lens' surface is made infinitesimally small. The ray tubes are thus reduced to points on the lens' surface, as illustrated in Figure 15. The two rays originating from the diametrically opposite corners of the slot (or array) define the bounds over which θ_i may vary. However, it is not expected that the incident angle will vary over these extreme bounds and it is subsequently ignored in this thesis.

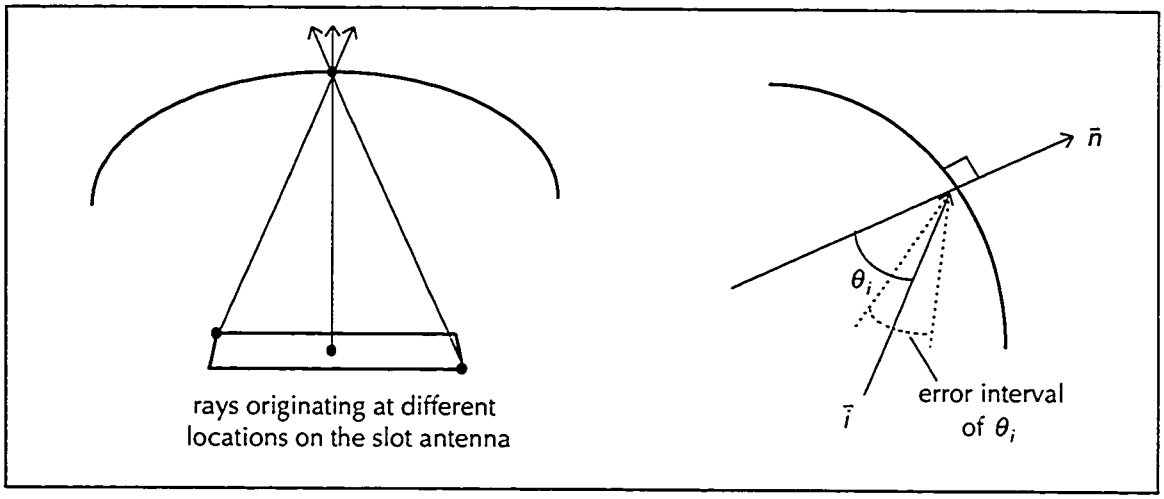

Figure 15: Directional Error Caused by the Ray Approximation

One way to determine the true direction of the incident vector is to use the PO propagators to predict only the transverse electric and magnetic field vectors. The cross product of these two yields the Poynting vector that would replace $\bar{i}$. To obtain these fields, the propagators can be modified so that only the 1/R terms are calculated. This method is valid because the $1/R^n$ terms in Equation (4-11) are additive and are not coupled. Unfortunately, this must be left as future work due to time limitations.

4.5.3 First Test Case

The minimum lens radius of a double slot array will now be determined. The feed array is identical to the one published in [18].

Slot Lengths	342.8 μm (0.708 λ_m)
Slot Widths	30 μm (approx.)
Extension Length	0 (hemispherical lens)
Frequency	246 GHz
Dielectric Constant of the Lens	11.7 (Silicon)
Magnetic Current Modes	One Fundamental Sinusoidal, variation in x
Magnetic Current Vector	x - directed
Slot Orientation (Slot Length Alignment)	x - axis
Array Direction	y - axis
Array Spacing	195.9 μm (0.549 λ_d)
Array Position	Center of the Lens Base
Phase Difference Between Slot Currents	0° (In Phase Excitation)

Table 3: Double Slot Array Parameters

The lens radii to be considered for this feed are the following: $5.6\lambda_0$, $1.0\lambda_0$, $0.5\lambda_0$, and $0.25\lambda_0$. With the exception of the dyadic Green's function code, which was corrected from [62], all of the code for the simulations was written in-house using MATLAB* .

Figure 16 displays the simulated electric and magnetic fields on the inside surface of a $5.6\lambda_0$ ($19.2\lambda_d$) radius hemispherical lens. The uppermost graph shows the magnitude of the exact magnetic field that is transverse to the incident vector $\bar{i}$, calculated using the full PO propagator. Let this quantity be denoted by $\bar{H}_{\perp}^{PO}$. The horizontal axis indicates the "point number", which corresponds to a discrete location on the lens surface. The exact physical locations corresponding to these points are not important; it is sufficient to know that they cover the entire lens surface.

---

* MATLAB is a registered trademark of The Mathworks, Inc.

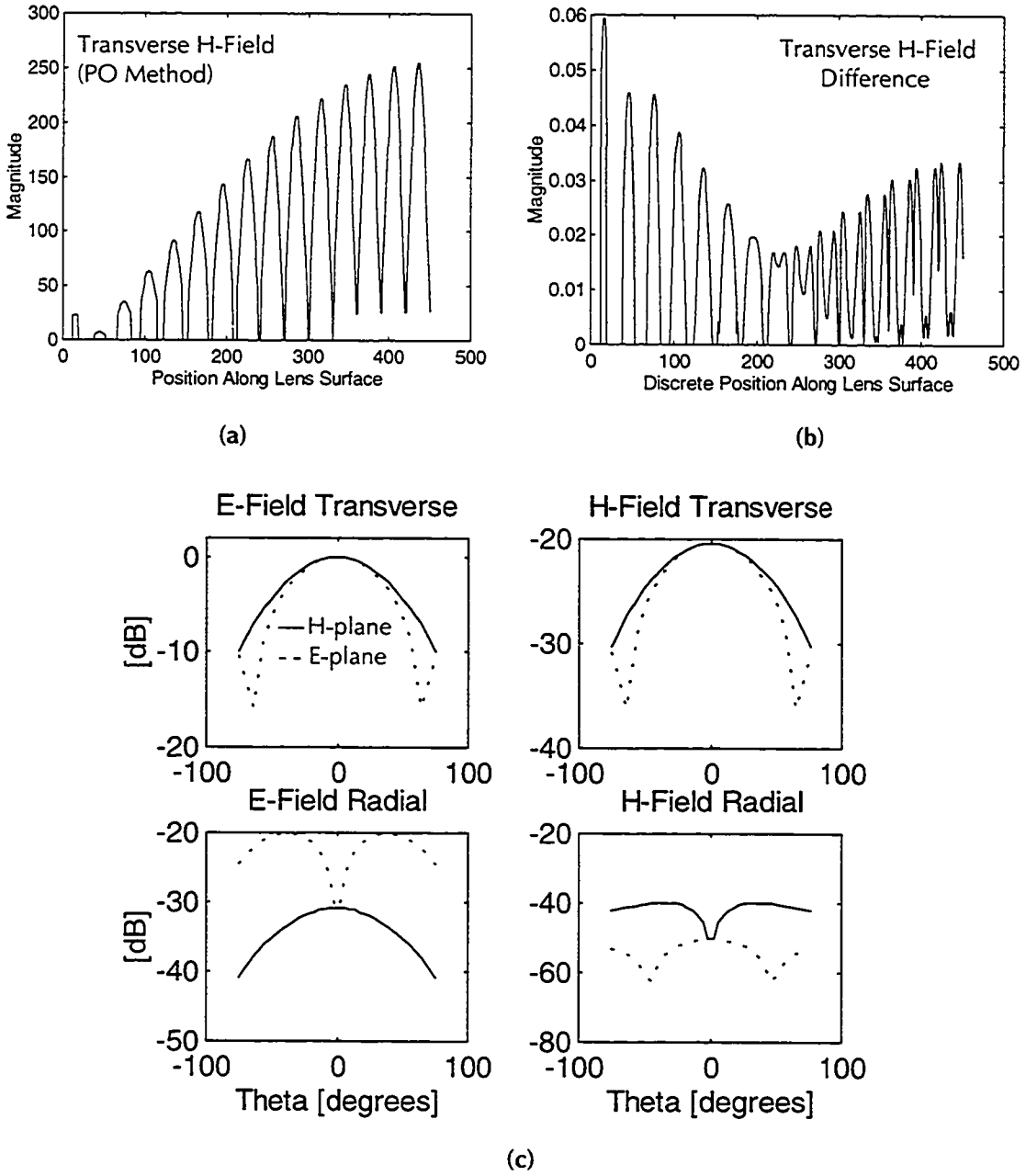

Figure 16: Case I, Electric and Magnetic Field Components, $R_{lens} = 5.6\lambda_0$, $L_E = 0$

(a) "Exact" $H_\perp$ magnitude as a function of position along lens surface
(b) Error in $H_\perp$ magnitude by Equation (4-20)
(c) Magnitude of transverse and radial components as a function of angle off of boresight

The second graph of Figure 16 shows the difference between this transverse magnetic field and that which is calculated using Equation (4-18):

$$Difference = \left| \bar{H}_{\perp}^{PO} - \frac{1}{Z_d} \hat{k} \times \bar{E}^{PO} \right| . \qquad \textbf{(4-20)}$$

The electric field used in this equation is the exact field that is calculated using its full PO propagator. The graph shows that there is very little difference between the two calculated values of the perpendicular magnetic field. The lower four graphs show the exact magnetic and electric fields' transverse and radial components, in vertical units of [dBV/m] or [dBA/m], where the dotted lines represent the E-plane data. The radial fields are seen to be negligibly small for this case.

Figure 17 presents the same information for a lens radius of $1.0\lambda_0$ ($3.4\lambda_d$). The difference between the transverse components of the H field calculated directly or by Equation (4-18) is again relatively small. The lower four graphs indicate that the radial components have increased. At its maximum level, the radial electric field is 12% of the transverse component at that same point. It is also interesting to note that the maximum radial and transverse components of the electric field do not occur at the same location in the E-plane.

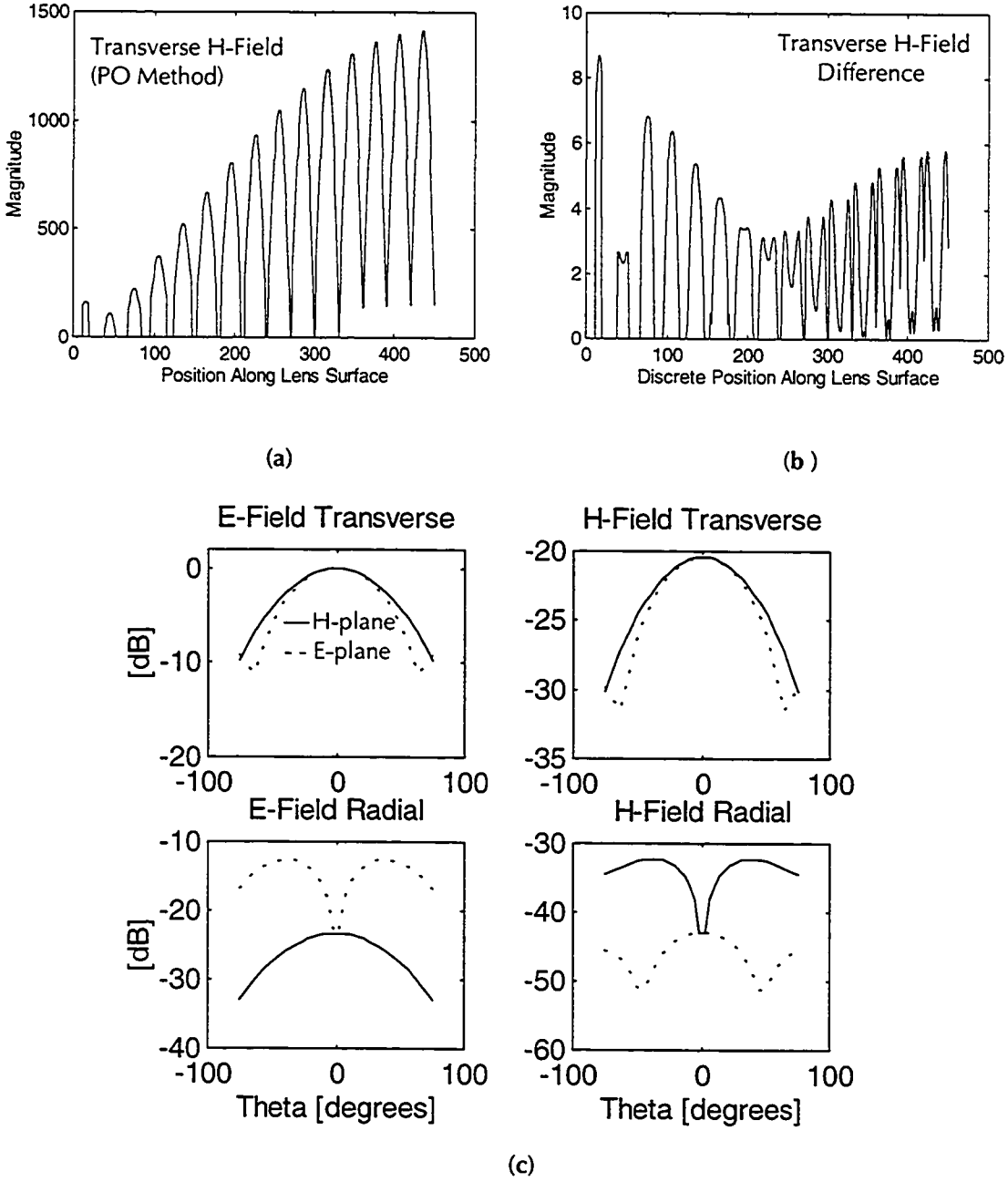

Figure 17: Case I, Electric and Magnetic Field Components, $R_{lens} = 1.0\lambda_0$, $L_E = 0$

(a) "Exact" $H_\perp$ magnitude as a function of position along lens surface
(b) Error in $H_\perp$ magnitude by Equation (4-20)
(c) Magnitude of transverse and radial components as a function of angle off of boresight

A reduction of the radius to $0.5\lambda_0$ ($1.7\lambda_d$) yields the results that are depicted in Figure 18. Again, the transverse H-field components are shown to be accurately predicted using Equation (4-18). However, the radial field components have increased significantly: the maximum level of the radial component of the electric field is now 23.5% of its transverse component at the location of the maximum radial component (in the E-plane, where both the transverse and radial components of the E-field attain their maximum values). However, it is worth noting that the radial electric field drops when the transverse electric field attains its maximum value. The maximum radial E-field value represents only 5.6% of the maximum transverse E-field value.

Figure 19 depicts the results for a hemispherical lens of radius $0.25\lambda_0$ ($0.86\lambda_d$). The error between the two calculated transverse H fields is now becoming significant. The radial field components are also quite significant. The radial E field at its maximum point is 56.7% of the transverse field at that same point, and the maximum electric radial field is 25.3% of the maximum transverse electric field. The maximum radial magnetic field is 28.8% of the maximum transverse magnetic field.

Based on these results, this simulator must fail as the lens radius is reduced below $0.5\lambda_0$. Beyond this point, the maximum radial components become a significant fraction of the maximum transverse fields.

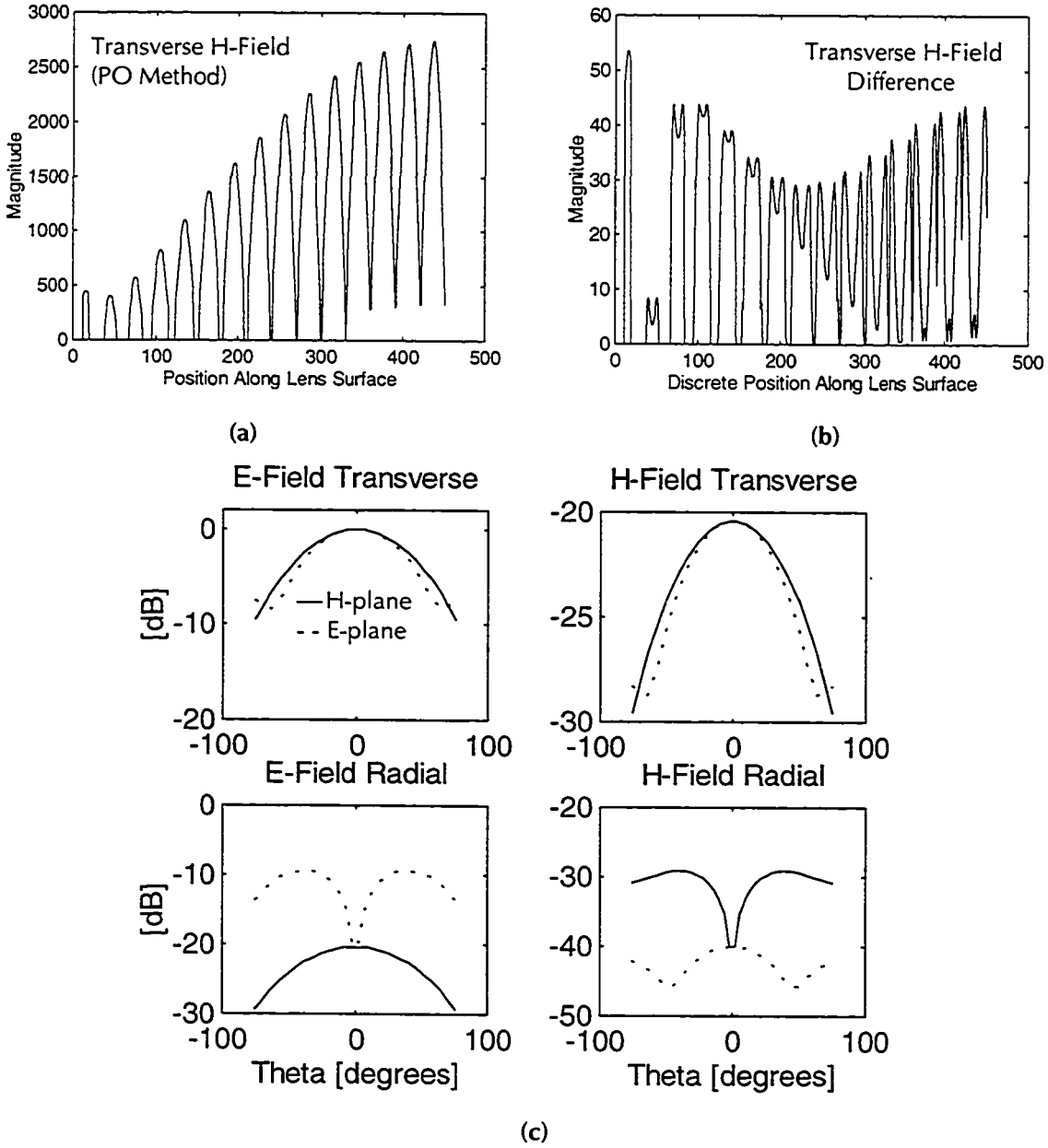

Figure 18: Case I, Electric and Magnetic Field Components, $R_{lens} = 0.5\lambda_0$, $L_E = 0$

(a) "Exact" $H_\perp$ magnitude as a function of position along lens surface
(b) Error in $H_\perp$ magnitude by Equation (4-20)
(c) Magnitude of transverse and radial components as a function of angle off of boresight

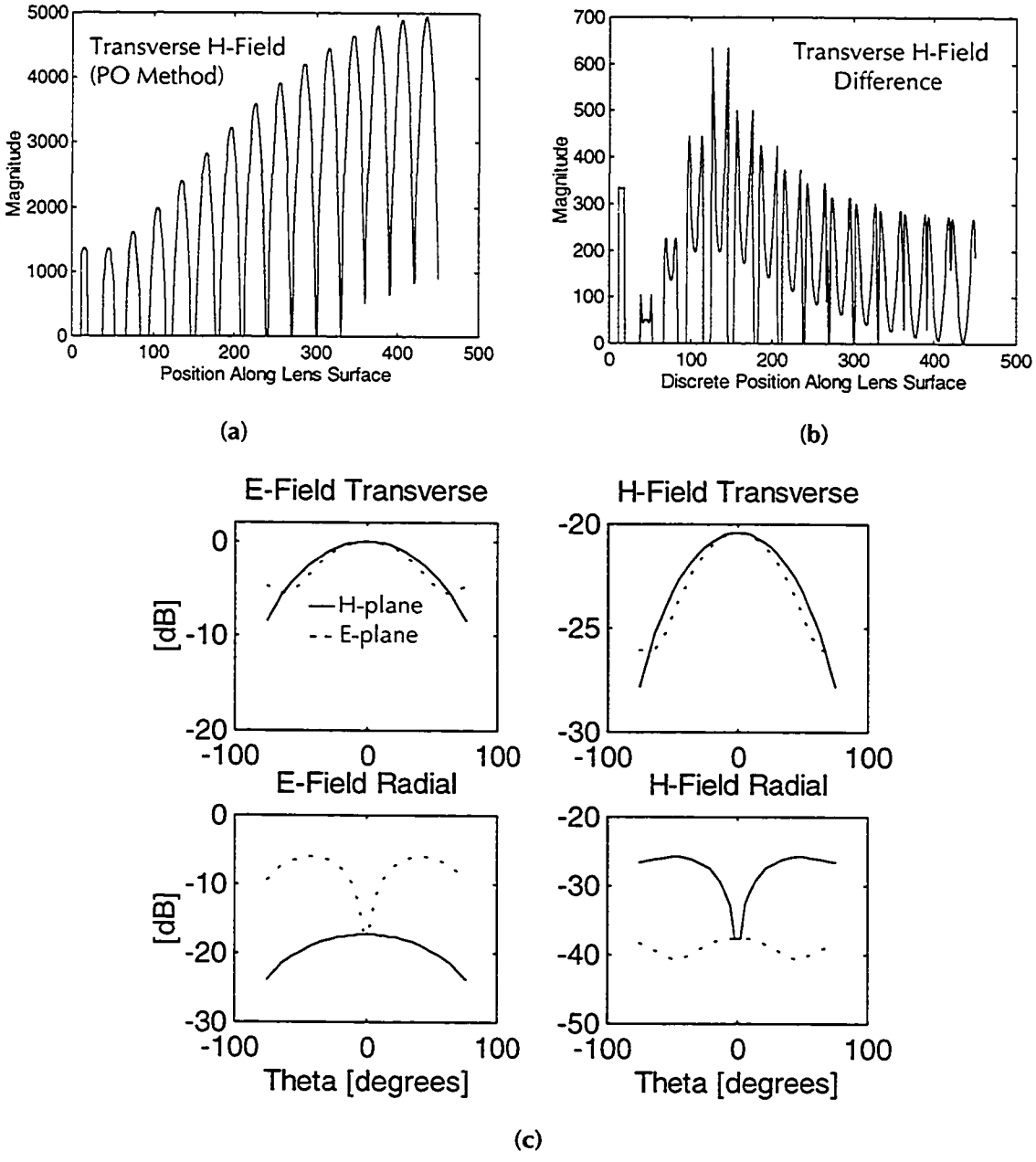

Figure 19: Case I, Electric and Magnetic Field Components, $R_{lens} = 0.25\lambda_0$, $L_E = 0$

(a) "Exact" $H_\perp$ magnitude as a function of position along lens surface
(b) Error in $H_\perp$ magnitude by Equation (4-20)
(c) Magnitude of transverse and radial components as a function of angle off of boresight

4.5.4 Second Test Case

The second test case to be examined is the configuration that will be tested experimentally in this thesis. The parameters for the single slot antenna are listed below.

Slot Length	3.023 mm (0.236 λ_m)
Slot Width	0.420 mm
Frequency	10 GHz
Dielectric Constant of the Lens	10 (C-stock AK-10)
Slot Orientation (Slot Length Alignment)	x - axis
Magnetic Current Modes	One Fundamental Sinusoidal, variation in x
Magnetic Current Vector	x - directed
Slot Position	Center of the Lens Base

Table 4: Single Slot Antenna Parameters

The radius values to be considered are $3\lambda_0$,$1.0\lambda_0$, $0.5\lambda_0$, and $0.25\lambda_0$. Of course, the minimum radius that can physically be considered is given by half the length of the slot, or $0.0504\lambda_0$.

Figure 20 shows the results for the largest hemispherical lens radius ($3\lambda_0 = 9.49\lambda_d$). The transverse components display the typical single slot radiation pattern, and the radial components are relatively low. The results for the $1.0\lambda_0$ ($3.16\lambda_d$) lens are similar and have not been included.

Figure 21 depicts the field patterns for the $0.5\lambda_0$ ($1.58\lambda_d$) radius lens. The transverse components of the magnetic field are exact to within 1% when using Equation (4-18). Observing the lower four graphs, the transverse component patterns have remained unchanged; however, the radial components have increased. Although the radial electric field is negligible, the maximum value of the radial magnetic field is now 18% of the maximum transverse magnetic field. It is also of interest to note that in the H-plane, the radial magnetic component is maximum when the transverse magnetic component is at its minimum, and vice versa.

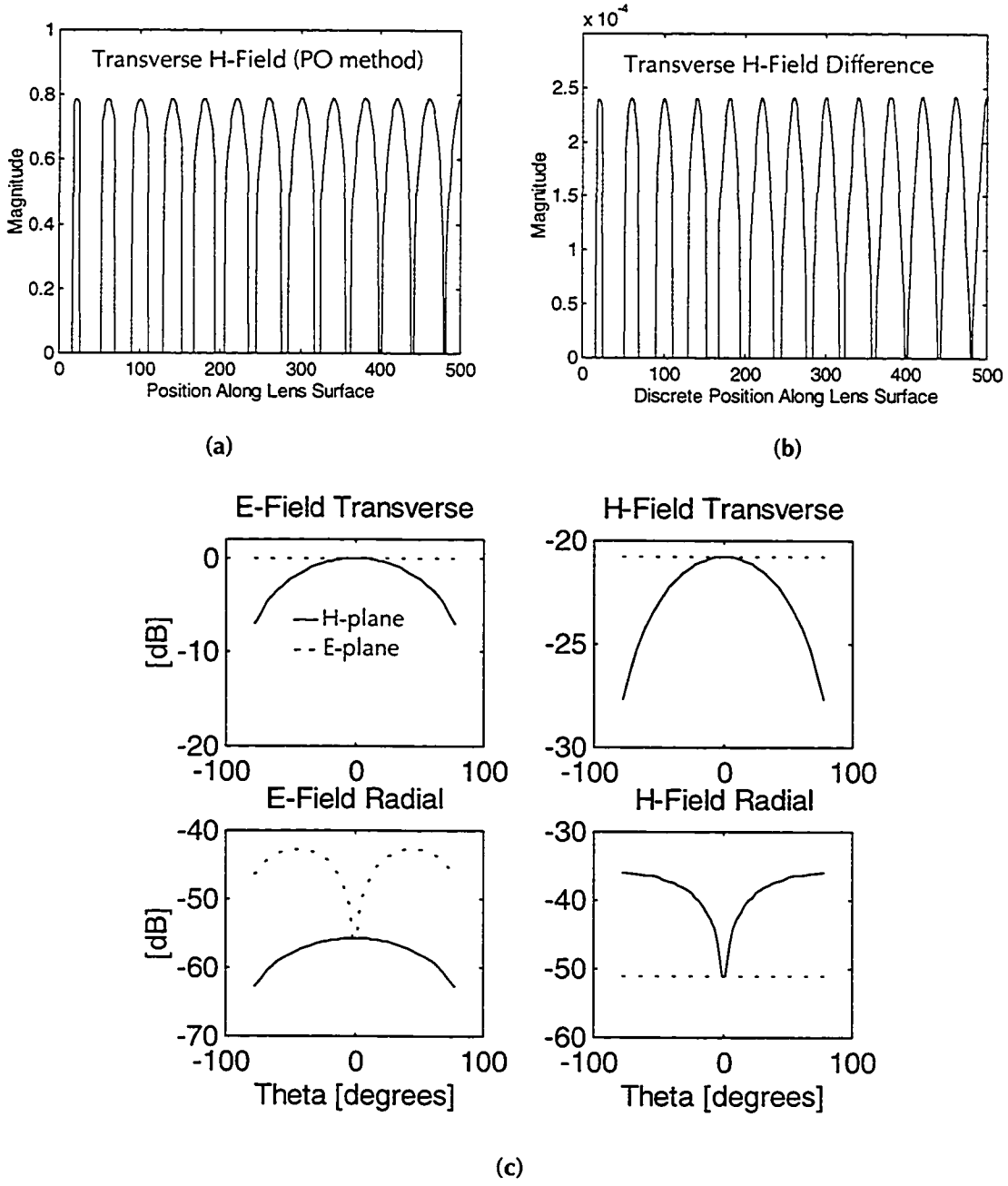

Figure 20: Case II, Electric and Magnetic Field Components, $R_{lens} = 3\lambda_0$, $L_E = 0$

(a) "Exact" $H_\perp$ magnitude as a function of position along lens surface

(b) Error in $H_\perp$ magnitude by Equation (4-20)

(c) Magnitude of transverse and radial components as a function of angle off of boresight

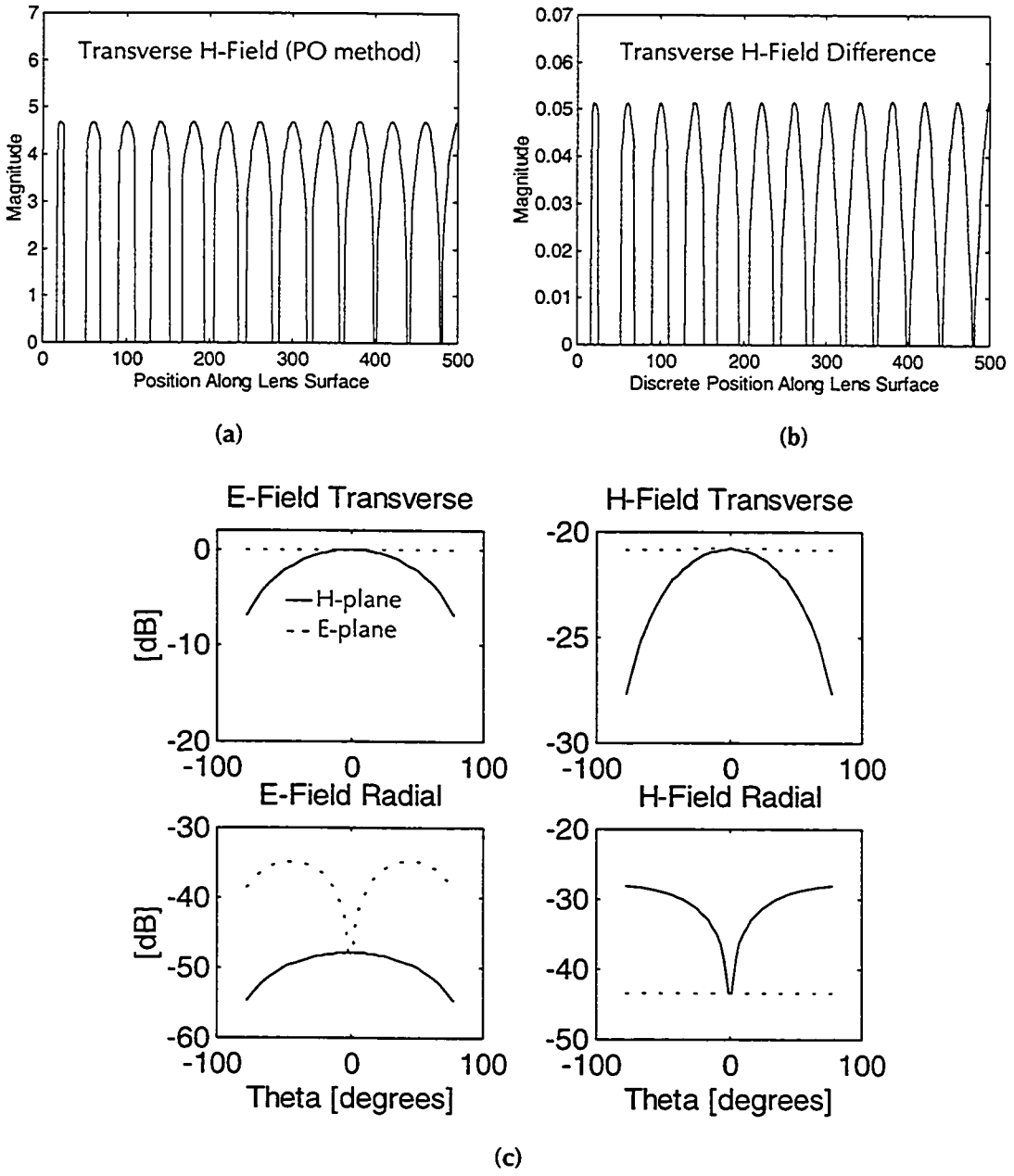

Figure 21: Case II, Electric and Magnetic Field Components, $R_{lens} = 0.5\lambda_0$, $L_E = 0$

(a) "Exact" $H_\perp$ magnitude as a function of position along lens surface
(b) Error in $H_\perp$ magnitude by Equation (4-20)
(c) Magnitude of transverse and radial components as a function of angle off of boresight

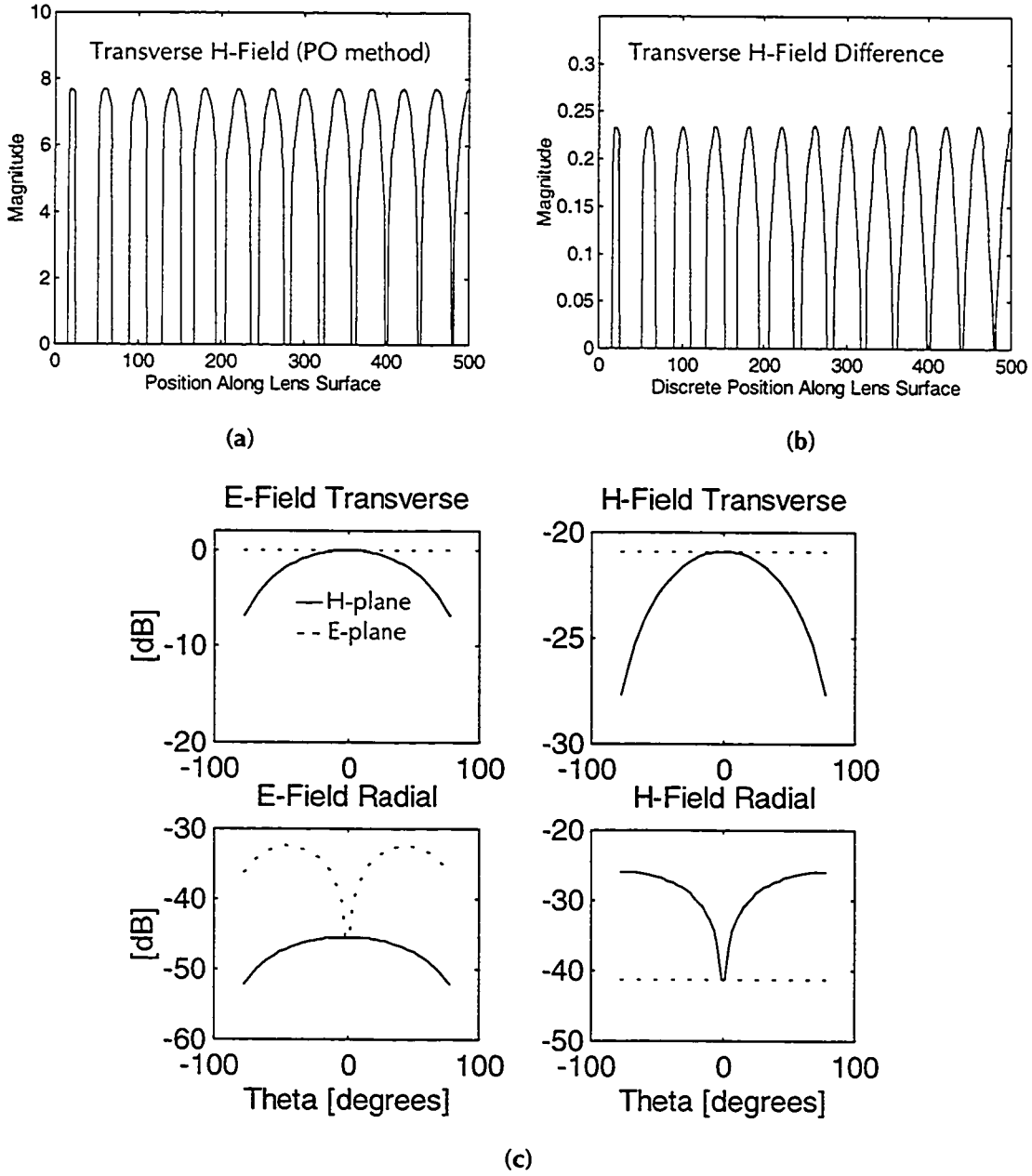

Figure 22: Case II, Electric and Magnetic Field Components, $R_{lens} = 0.3\lambda_0$, $L_E = 0$

(a) "Exact" $H_\perp$ magnitude as a function of position along lens surface
(b) Error in $H_\perp$ magnitude by Equation (4-20)
(c) Magnitude of transverse and radial components as a function of angle off of boresight

Figure 22 illustrates the results when the radius is reduced to $0.3\lambda_0$ ($0.95\lambda_d$). Although both the radial E-field and the error in calculating the transverse H-field using Equation (4-18) are small, the radial H-field is not. The maximum value of that component is now 38.7% of the maximum transverse H-field.

4.5.5 Comparative Results

As a point of interest, the percentage of the maximum radial component with respect to the maximum transverse component is plotted as a function of the lens radius in Figure 23. The vertical axes indicate the percentage, and the horizontal axes indicate the radius of the lens, in units of wavelengths in the dielectric (λ_d).

Analysing the results for the first case (double slot), it is seen that the percentage of the radial component of the E-field is approximately the same as that of the H-field. The maximum radial value surpasses 10% of the maximum transverse value at a lens radius that is surprisingly very close to the far-field distance criterion (Appendix C):

$$\frac{2D^2}{\lambda_d} = 1.83\lambda_d = 0.54\lambda_0 \ .$$

The situation is not the same for the single slot feed antenna, Case II. The radial component of the electric field, although increasing as the radius is reduced, is seen to be negligibly small. However, the maximum value of the magnetic field's radial component is more than 10% of the maximum transverse component when the lens radius is $3\lambda_d$. This is well before the distance that is predicted by the far-field distance formula:

$$\frac{2D^2}{\lambda_d} = 0.20\lambda_d = 0.064\lambda_0 .$$

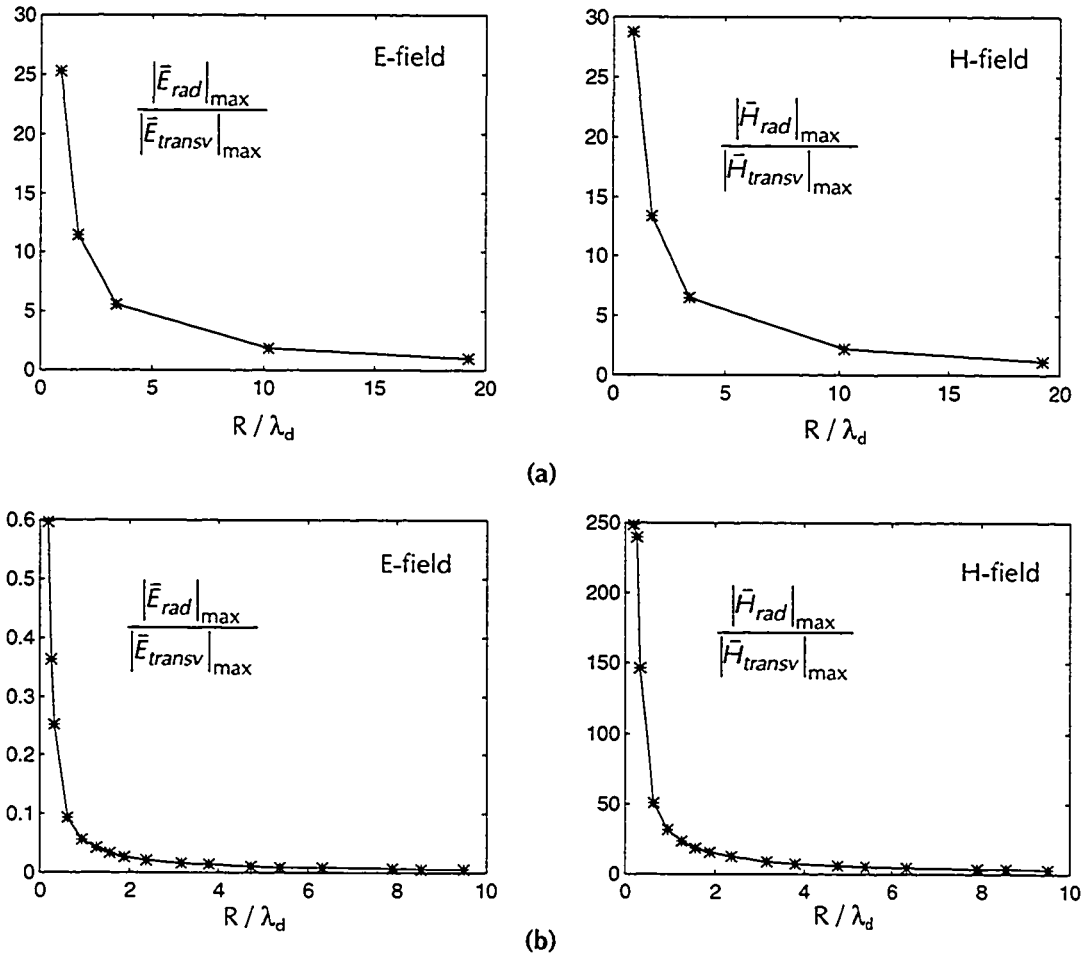

Figure 23: Maximum Radial Component as a Percentage of the Maximum Transverse Component vs. the Normalized Lens Radius

(a) Case I, Electric and Magnetic Fields

(b) Case II, Electric and Magnetic Fields

4.5.6 Conclusion - Range of Validity

For the double-slot case, both the radial components and the ray approximation set the minimum lens size to approximately $0.5\lambda_0$. For the single slot, the radial component of the magnetic field becomes significant (>10%) when the lens radius is $\approx 1\lambda_0$. If the lens radii are reduced below these limits, the approximations that are used at the lens-to-air boundary will cause the method to fail.

5. Simulation Results

In this fifth chapter, the results of the hybrid analysis are studied. First, the hybrid analysis results using closed-form illumination are compared to those obtained using PO illumination. The directivities of the lenses are then computed versus the lenses' extension lengths and radii. Reflection loss effects are examined, and the chapter closes with a preliminary analysis of the reflected energy's contribution to the radiation pattern.

5.1 Comparison Between Closed-Form and Physical Optics Lens Illuminations for a Double-Slot Array

The closed-form lens illumination used by Filipovic *et al.* [13] in their hybrid analysis of a double-slot array is now compared to the PO illumination hybrid analysis. Here, lens illumination refers to the simulation technique that is used to predict the values of the fields originating from the slot antenna. Previous work relies on closed-form far-field equations to illuminate the lens, while the PO approach uses the free-space dyadic Green's functions described in previous sections. The specifications of the double-slot array used by Filipovic *et al.* have already been given in Table 3 of Section 4.5.3 . The geometry of the array is shown in Figure 24. The closed-form far-field lens illumination technique assumes that the slots are excited in-phase with a single fundamental sinusoidal mode. The far-field expressions for this antenna are given by Equation (5-1) in spherical coordinates [57,p.596].

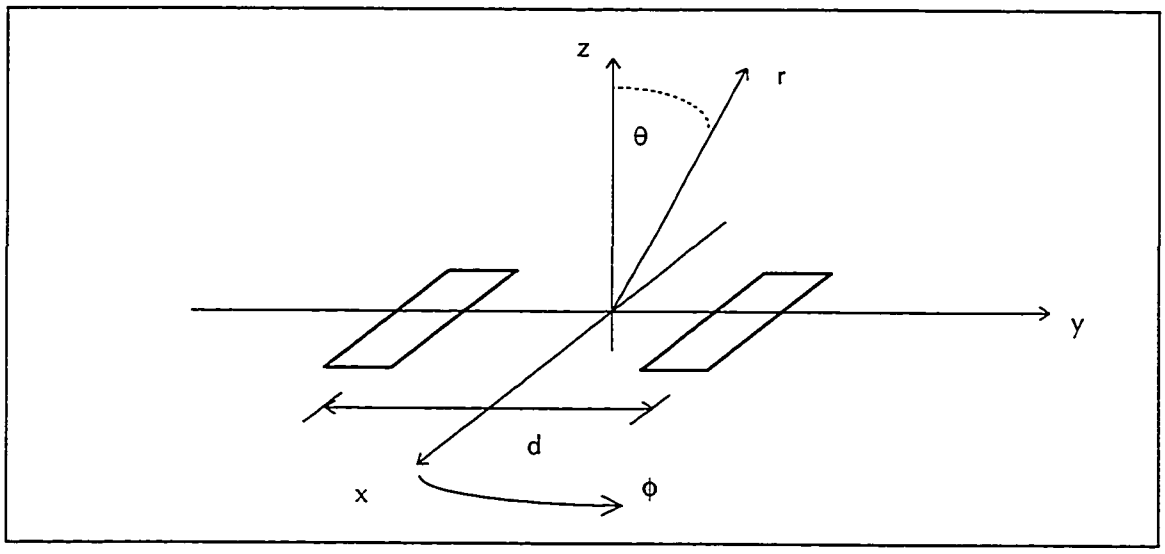

Figure 24: Double-Slot Geometry

$$E_\phi = (AF)\frac{-jk_d E_0 L_S W_S \cos\theta\cos\phi}{2\pi r} e^{-jk_d r}\left[\frac{\left(\frac{\pi}{2}\right)\cos\left(\frac{k_d L_S}{2}\sin\theta\cos\phi\right)}{\left(\frac{k_d L_S}{2}\sin\theta\cos\phi\right)^2 - \left(\frac{\pi}{2}\right)^2}\right]\left[\frac{\sin\left(\frac{k_d W_S}{2}\sin\theta\sin\phi\right)}{\frac{k_d W_S}{2}\sin\theta\sin\phi}\right] \tag{5-1}$$

$$E_\theta = (AF)\frac{-jk_d E_0 L_S W_S \sin\phi}{2\pi r} e^{-jk_d r}\left[\frac{\left(\frac{\pi}{2}\right)\cos\left(\frac{k_d L_S}{2}\sin\theta\cos\phi\right)}{\left(\frac{k_d L_S}{2}\sin\theta\cos\phi\right)^2 - \left(\frac{\pi}{2}\right)^2}\right]\left[\frac{\sin\left(\frac{k_d W_S}{2}\sin\theta\sin\phi\right)}{\frac{k_d W_S}{2}\sin\theta\sin\phi}\right]$$

The array factor, *AF*, is for a two-element array on the y-axis:

$$AF = \cos\left(\frac{k_d d}{2}\sin\phi\sin\theta\right). \tag{5-2}$$

The variables L_S and W_S are the length and width of the slot, d is the distance between the two slots, E_0 is the maximum electric field in the slot, k_d is the wavenumber inside the dielectric lens, and E_ϕ and E_θ represent the far-field phi and theta electric field polarisations, respectively.

The illumination generated by these equations is now compared to the illumination generated by the PO method at various radial distances r from the origin. Note that the *shape* of the patterns generated by the closed-form equations are *not* a function of r, while no such restriction exists for the PO method.

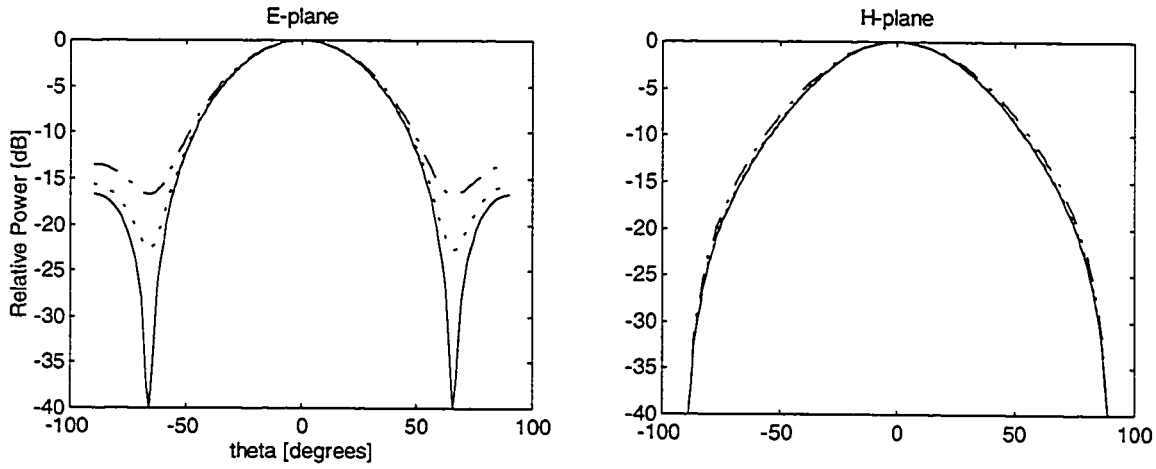

Figure 25: E- and H-plane Illuminations from a Double-Slot Array

(——) Closed-Form Formulation

(- - - -) PO Formulation with $r = \lambda_0$

(- · - · -) PO Formulation with $r = 0.5\lambda_0$

In Figure 25, the solid lines represent the closed-form far-field patterns. The dashed line is the PO pattern taken at $r = 1\lambda_0$, and the dash-dot line is the PO pattern taken at $r = 0.5\lambda_0$. Although not shown, it has been found that the PO illumination is exactly equal to the closed-form far-field illumination when r is large ($>10\lambda_0$). However, as r decreases below $10\lambda_0$, discrepancies appear between the PO results and the far-field equations in the E-plane. The PO results indicate that the sidelobes tend to increase and that the pattern nulls are transformed into shoulders as the radius r is reduced. The results also indicate that the H-plane pattern, which is not affected by the array factor ($\phi = 0°$), is almost identical for both analysis methods regardless of the radial distance.

The above analysis was performed without the lens. It must now be ascertained whether this illumination discrepancy will affect the lens' radiation pattern once the hybrid analysis is applied. The radiated fields from elliptical extension lenses of various radii will be calculated in Section 5.3 and in Section 5.4 using the results from both of the lens illumination methods.

5.2 Validation of the Hybrid Simulation Technique

In this section, the MATLAB simulator is used to compute the radiation pattern of a SLA that has been simulated by Filipovic *et al.* [13] using the hybrid GO technique. The $5.6\lambda_0$-radius silicon lens has an elliptical extension and is fed by the double slot array that was described in Table 3. To accurately compare the simulation results to the published data, the simulation is conducted using the closed-form illumination formulation that is specified by Equation (5-1). These results are depicted in Figure 26 and compare well to the published data.

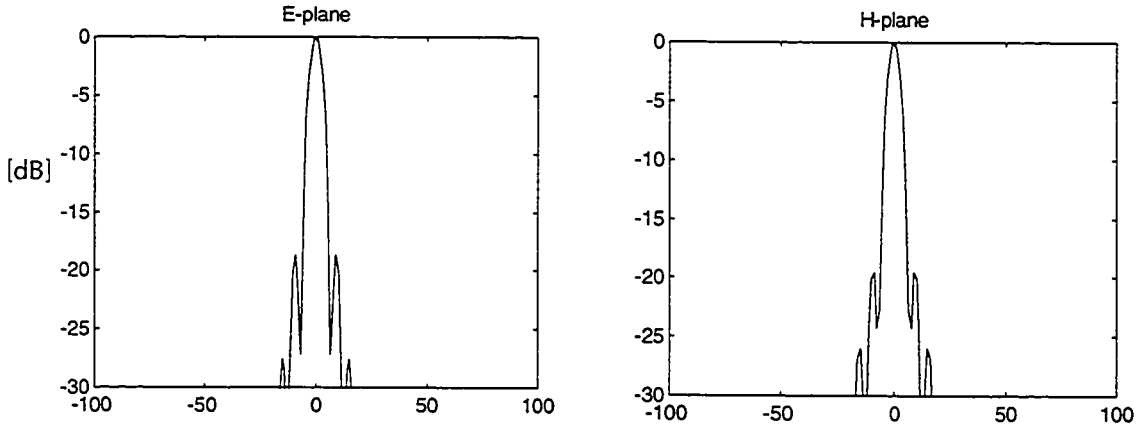

Figure 26: Simulated Radiation Patterns for a Closed-Form Illuminated $5.6\lambda_0$-radius Elliptical Lens

5.3 Comparison Between the Radiation Patterns of Double Slot-Fed SLAs that are Illuminated by Closed-Form Equations and Physical Optics

The results of Section 5.1 demonstrated that discrepancies exist between the PO and the closed-form double slot-fed lens illuminations. In this section, the effects of these discrepancies on the SLA radiation pattern will be determined. Figure 27 illustrates the radiation patterns for an elliptical extension, $1\lambda_0$-radius lens. The solid line represents the closed-form illuminated far-field lens pattern, while the dash-dot line represents the far-field pattern obtained by PO illumination. Although the patterns are not exactly the same, it is observed that the illuminations' impact on the radiation patterns is minimal.

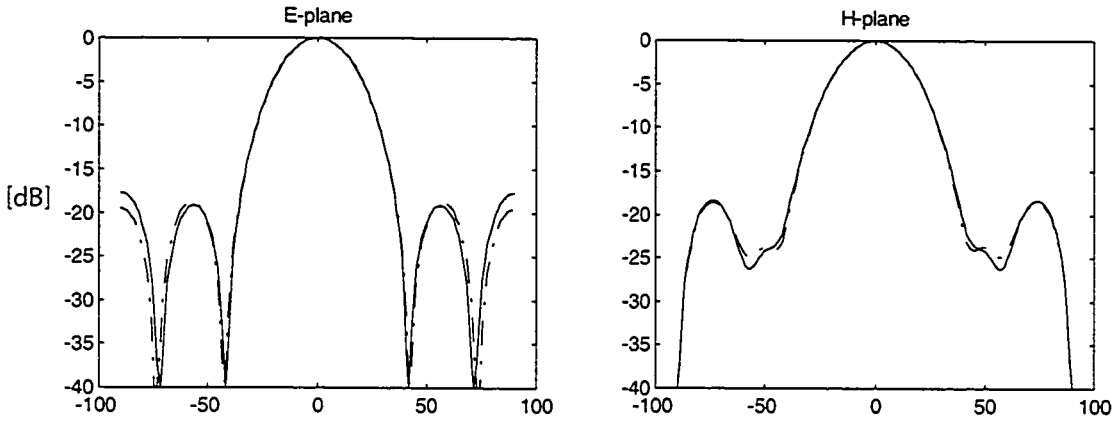

Figure 27: Radiation Patterns for a Double-Slot Fed $1\lambda_0$-radius Elliptical Extension Lens
(——) Closed-Form Illumination Formulation
(- · - · -) PO Illumination Formulation

Reducing the lens radius to $0.5\lambda_0$, the graphs of Figure 28 are obtained. Again, the solid line represents the results obtained by closed-form illumination. It is observed that the PO illumination predicts a slightly narrower main lobe and higher cusps in the E-plane, while the H-plane results are almost identical for both illuminations. Smaller lens radii will not be simulated because it has been determined that the radial fields become significant beyond the $0.5\lambda_0$ lens radius for this feed

configuration (see Section 4.5.3). Strong radial components violate the Fresnel equations that are used at the lens-to-air interface.

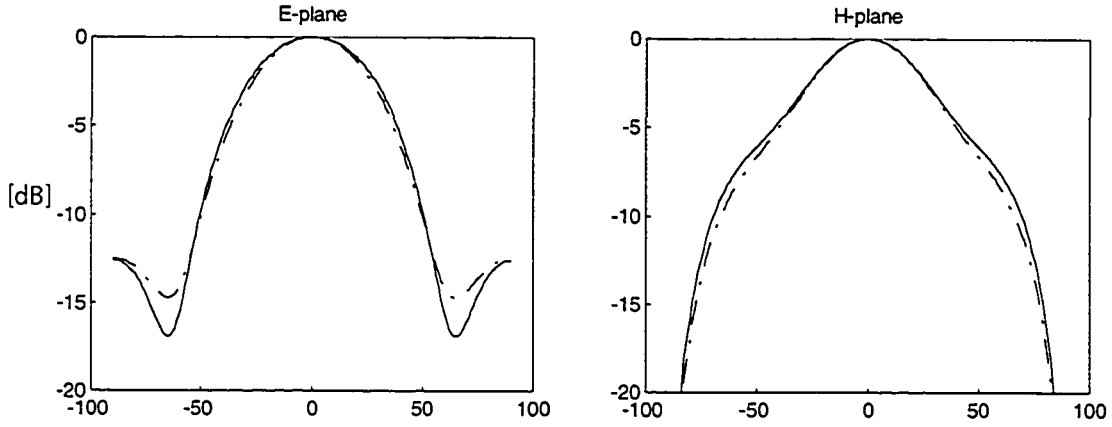

Figure 28: Radiation Patterns for a Double-Slot Fed $0.5\lambda_0$-radius Elliptical Extension Lens

(——) Closed-Form Illumination Formulation

(- - - -) PO Illumination Formulation

The results indicate that the closed-form far-field illumination is quite accurate for the two-element feed down to a lens radius of $0.5\lambda_0$. It is also of interest to note the general variation of the patterns as the lens size is reduced. Indeed, the effects of diffraction are clearly dominant, as the beamwidth increases significantly as the lens aperture is reduced. The variation in directivity as a function of the lens size will be computed in a subsequent section of this chapter.

5.4 Comparison Between the Radiation Patterns of Single Slot-Fed SLAs that are Illuminated by Closed-Form Equations and Physical Optics

Attention is now focused on the single slot feed. The single slot geometry is the same as that given in Figure 12 of Section 3.4.1 . The closed-form far-field expressions for the single slot feed are the same as those for the double-slot array given in the previous section, except that the array factor is omitted from the equations. The illumination generated by these equations is now compared to the PO illumination. Again, the *shape* of the patterns predicted by the far-field equations does *not* vary as a function of the radial distance r form the slot. The patterns are compared in Figure 29.

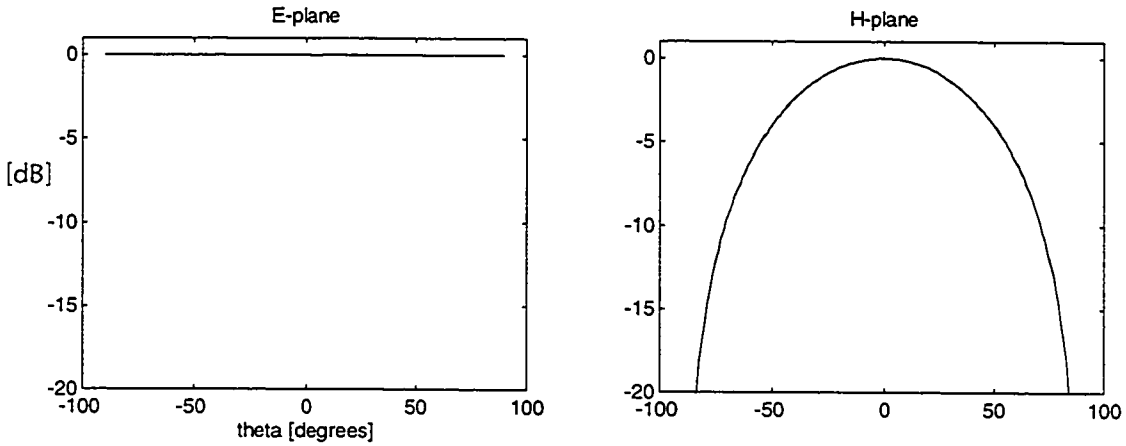

Figure 29: E- and H-plane Illuminations from a Single Slot
(——) Closed-Form Illumination Formulation
(- · · - ·) PO Illumination Formulation

The solid line again represents the closed-form illumination, while the dotted line, which is barely distinguishable, represents PO illumination at $r = 0.5\lambda_0$. It is observed that the patterns are identical, therefore both methods are suitable for illuminating the lens.

The two illuminations are now used in the hybrid analysis of the lens. The resulting radiation patterns are shown in Figure 30 and Figure 31 for elliptical-extension lenses of radii $1\lambda_0$ and $0.5\lambda_0$.

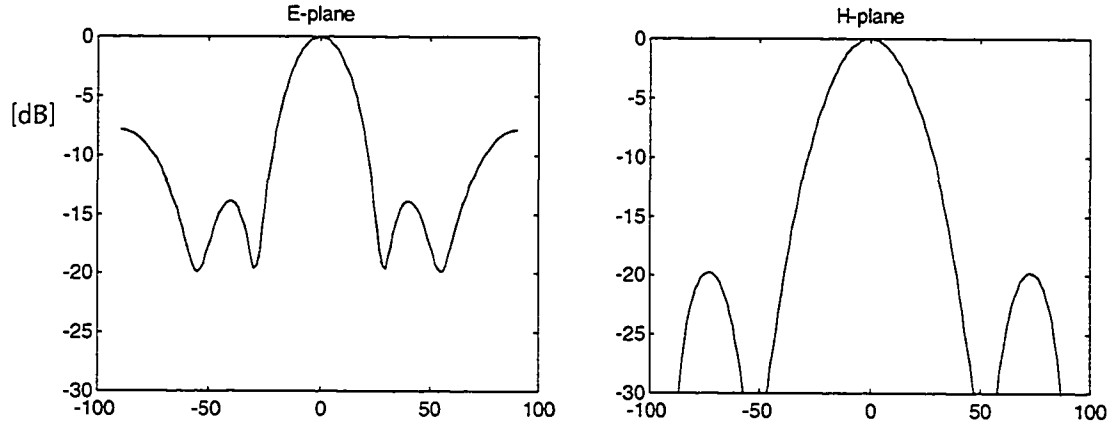

Figure 30: Radiation Patterns for a Single Slot-Fed $1\lambda_0$-radius Elliptical Extension Lens

(——) Closed-Form Illumination Formulation

(- · - · -) PO Illumination Formulation (indistinguishable)

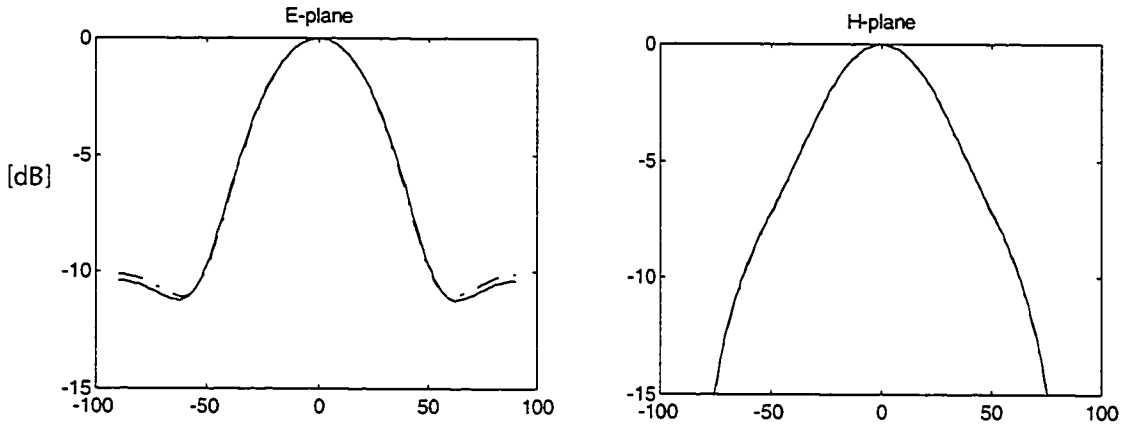

Figure 31: Radiation Patterns for a Single Slot-Fed $0.5\lambda_0$-radius Elliptical Extension Lens

(——) Closed-Form Illumination Formulation

(- · - · -) PO Illumination Formulation

The solid lines represent the far-fields that are obtained using the closed-form illumination. It is observed that the differences are indeed minimal for these cases. Again, smaller lens radii are not simulated, since the resulting radial field components become significant and negate the use of the Fresnel equations at the lens-to-air boundary, as calculated in Section 4.5.5 .

Coupled with the minimum lens size limitations imposed in Section 4.5.5, the results indicate that closed-form far-field expressions are sufficiently accurate for illuminating the lens. Although it is more precise, the slower PO propagator is not required for single-slot lens illumination.

5.5 Directivity of Single Slot-Fed Lenses

The directivities of elliptical and hyperhemispherical slot fed lenses are calculated numerically using the algorithm described below [57,pp.53-55]. Since only the half space above the lens is considered, a total solid angle of 2π steradians is covered and the directivity is calculated based on the equation:

$$D_0 = \frac{2\pi U_{\max}}{P_{rad}}, \tag{5-3}$$

where U_{max} is the maximum radiation intensity, P_{rad} is the total radiated power into the half space, and D_0 is the directivity of the SLA. By sampling the far-field hemisphere above the SLA, the normalized far-field pattern of the antenna, $F(\theta_i,\phi_j)$, is calculated, where the subscripts i and j are indexing terms into the theta and phi arrays, respectively. The maximum normalized radiation intensity is thus simply:

$$U_{\max} = F\left(\theta_i,\phi_j\right)\Big|_{\max}. \tag{5-4}$$

The total radiated power is calculated analytically as:

$$P_{rad} = \int_0^{2\pi}\int_0^{\frac{\pi}{2}} F(\theta,\phi)\sin\theta d\theta d\phi, \tag{5-5}$$

where $F(\theta,\phi)$ is a continuous function.

The series approximation to this double integral is the following double summation:

$$P_{rad} \approx \sum_{j=1}^{M} \left\{ \sum_{i=1}^{N} F(\theta_i, \phi_j) \sin\theta_i \Delta\theta_i \right\} \Delta\phi_j, \quad \left(\sum_j \Delta\phi_j = 2\pi \quad \text{and} \quad \sum_i \Delta\theta_i = \frac{\pi}{2} \right), \qquad \textbf{(5-6)}$$

where M and N are the number of points in ϕ and θ, respectively, and $\Delta\theta_i$ and $\Delta\phi_j$ are the size of the i^{th} θ and of the j^{th} ϕ increments, respectively. In this scheme, a theta plane summation is taken at every phi increment. Although there are many ways to define the interval, a trailing edge approach is taken, where the entire increment's interval assumes the constant value that is evaluated at its beginning, as shown in Figure 32.

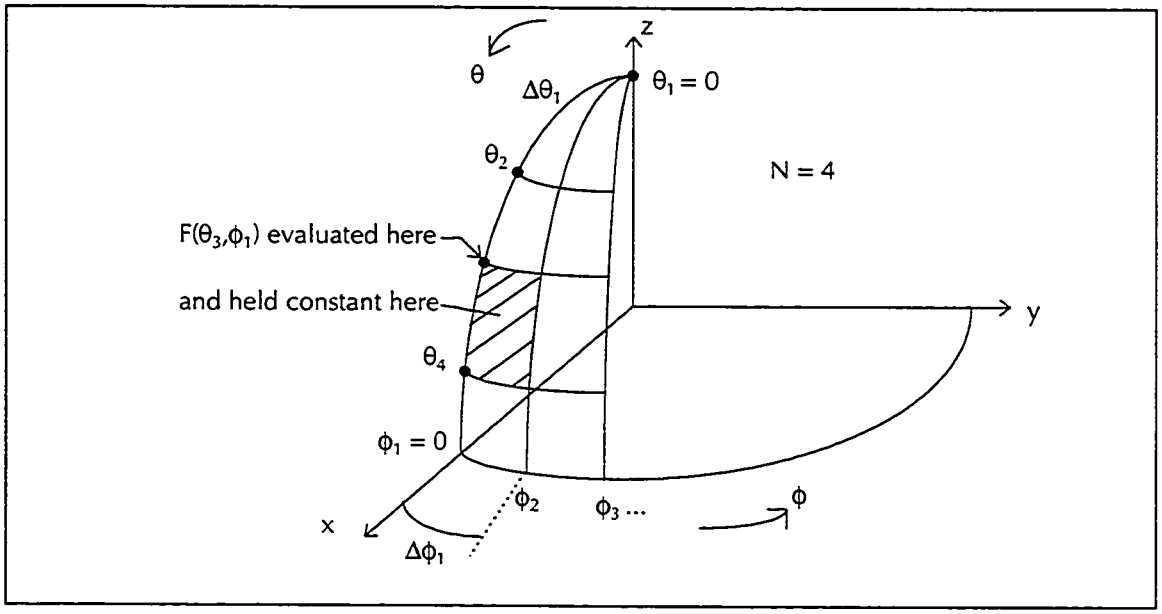

Figure 32: Sampling Scheme for Directivity Calculations

The directivities of elliptical and hyperhemispherical lenses of varying radii have been computed and are displayed in Figure 33.

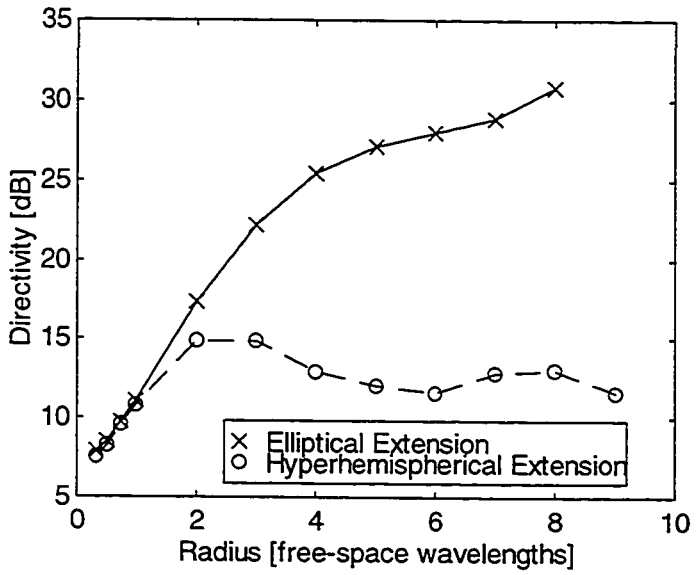

Figure 33: Directivity of Single Slot Fed SLAs, $\varepsilon_r = 10$

The results indicate that both the elliptical and hyperhemispherical lenses have similar directivities up to a radius of $R_{lens} \approx 1\lambda_0$. The directivity of the elliptical lens then steadily increases as the radius is increased. This is expected, since the spot size of a diffraction limited beam decreases as the aperture's size increases. The hyperhemispherical lens displays an oscillatory response, varying between approximately 12 and 15 dB. For comparison, a single slot radiating into free-space without a lens has a directivity of 4.9 dBi (when calculated over a total solid angle of 2π steradians, as was done for the SLAs).

5.6 Reflection Loss Analysis

The lenses that are studied in this thesis have not been fitted with a quarter-wave matching cap layer. Therefore, the SLAs are susceptible to strong reflections at the lens-to-air interface and hence the curves in Figure 33 do not give a true indication of the gain that could be achieved. This is a major concern for three reasons:

1. the simulator is not designed to handle reflections because it uses the free-space dyadic Green's function,
2. the source current is assumed to be known and not affected by reaction, and,
3. the reflections will degrade the radiation pattern.

The first and second points are related. Indeed, the use of the free-space Green's function implies that the source currents cannot be affected by any returning radiation. And although the first reflection's effect on the radiation pattern is predicted in a later section, the problem quickly becomes intractable for subsequent reflections. This is due to the one-way nature of the ray tracing that is used in the simulator. In this sense, the MATLAB simulator seems better suited for transient analyses than it does for steady-state problems. Nonetheless, the simulated results may still be of value, especially if the reflection is minimized. The magnitude of the reflection is obviously controlled by the reflection coefficients at the interface. The TE and TM reflection coefficients are functions of the incident angle and of the surface's normal vector (see the definition of θ_i in Figure 14). The incident angle, in turn, is a function of the extension length and of the launch angle of the incident ray. The reflection and transmission coefficients are plotted in Figure 34 for a lens that has a permittivity of 10.

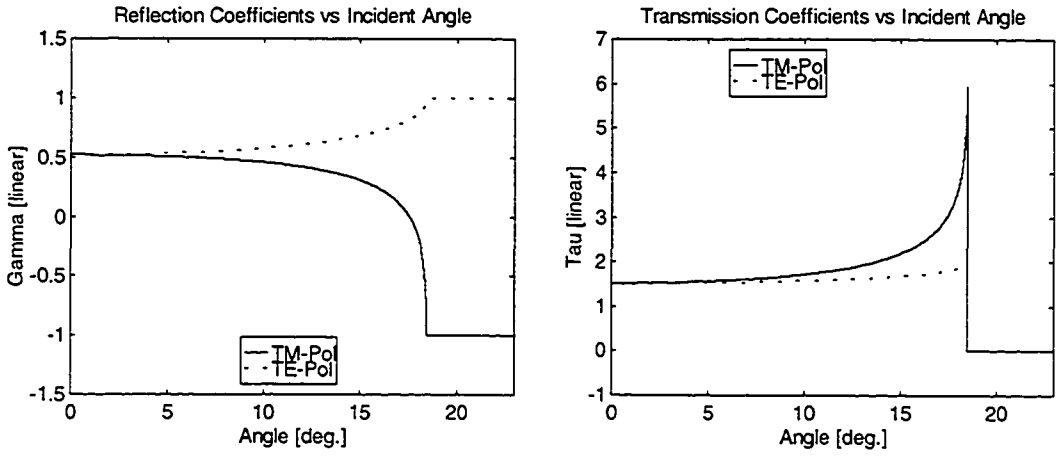

Figure 34: Reflection and Transmission Coefficients for $\varepsilon_r = 10$

Observe that as the incident angle increases, the reflection progressively worsens for the TE-polarised fields until total internal reflection occurs at the critical angle of $\theta_i = \theta_c = 18.43°$. Conversely, the TM-polarised reflection decreases until the Brewster angle is reached at $\theta_i = \theta_B = 17.55°$. The TM reflection then quickly worsens as the angle approaches the critical value. Note that the transmission coefficients are greater than unity. This is because the lens' permittivity is greater than that of free-space. Although the transmission coefficients increase as the reflection coefficients approach ±1, they are not indicative of the amount of power that is being transmitted through the boundary.

As previously stated, the incident angle, and therefore the reflection, are functions of both the extension length and the incident ray's launch angle. Let the Reflection Loss (RL) of the lens be redefined as:

$$RL = -10\log_{10}\left(\frac{\text{Total Transmitted Power through the Lens}}{\text{Total Power Incident on the Lens Surface}}\right). \qquad (5\text{-}7)$$

This value is plotted as a function of the extension length in Figure 35 for a $1\lambda_0$-radius lens that has a permittivity of 10. Interestingly, the reflection loss decreases until a minimum value of

approximately 0.98 dB is reached near the hyperhemispherical extension length of $L_E = \frac{R_{lens}}{\sqrt{\varepsilon_r}} = 9.5\,\text{mm}$.

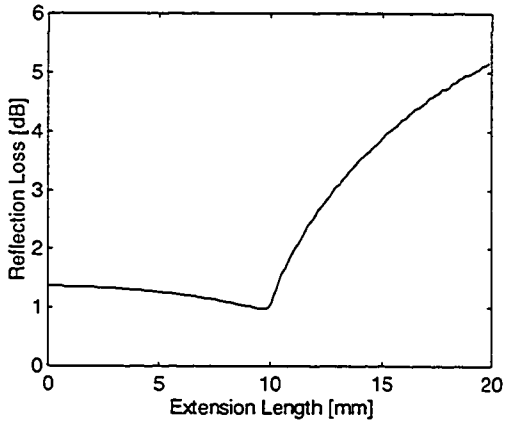

Figure 35: Reflection Loss versus Extension Length for $R_{lens} = 1\lambda_0$ and $\varepsilon_r = 10$

The reflection loss then quickly deteriorates as the extension is further increased. It is of interest to note that the reflection loss is quite severe at the elliptical extension of 12.87 mm, where the pattern gain of the SLA is maximised. Continuing the analysis, the total incident power from the slot feed antenna has been calculated to be 75.5% TM-polarised at the lens-to-air interface. The reflection loss curve is therefore more strongly affected by the TM reflection coefficient. Further, this percentage appears to be only weakly influenced by the extension length.

In the work that follows, the terms *launch angle* (θ) and *incident angle* (θ_i) will be used extensively. These are defined in Figure 36. The launch angle is simply the azimuthal angle between the z-axis and the incident ray, while the incident angle is the angle subtended between the surface normal and the incident ray.

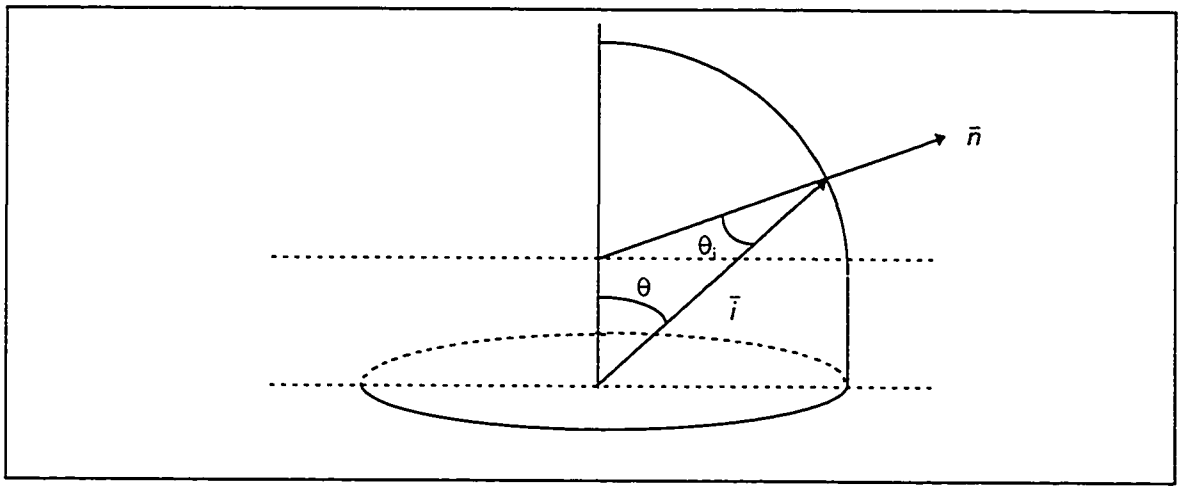

Figure 36: Launch Angle and Incident Angle Geometry

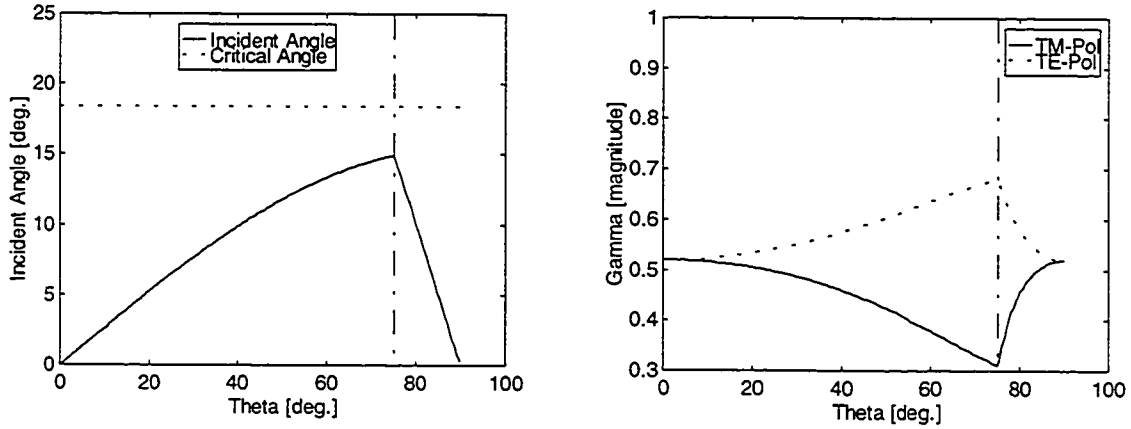

(a) (b)

Figure 37: (a) Incident Angle and (b) Reflection Coefficients for $R_{lens} = 1\lambda_0$, $\varepsilon_r = 10$, and $L_E = 8$ mm

The incident angle θ_i is plotted versus the launch angle of the incident ray on the left side of Figure 37. A θ-plane cut through the lens at any ϕ angle yields the same curve. The curve is for a $1\lambda_0$-radius lens with an extension length of 8.0 mm and a permittivity of 10. In this plot, the launch angle θ varies from 0° (lens zenith) to 90° (parallel with the substrate). The straight vertical line indicates the transition from the incident ray falling on the hemispherical surface to the cylindrical one, and the straight horizontal line indicates the critical angle. The graph indicates that the incident angle reaches a maximum at the hemisphere-to-cylinder transition but that this maximum

does not exceed the critical angle for the L_E = 8 mm case. The graph on the right side of Figure 37 shows the corresponding reflection coefficient curves. Although the dominant TM reflection coefficient decreases, it never reaches zero.

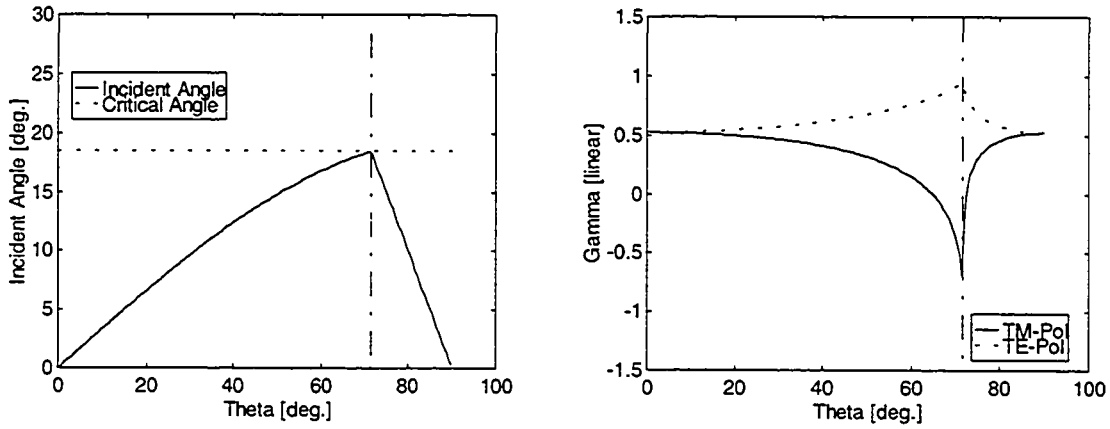

Figure 38: (a) Incident Angle and (b) Reflection Coefficient for $R_{lens} = 1\lambda_0$, $\varepsilon_r = 10$, and $L_E = 10$ mm

Figure 38 displays the same data for an extension length of 10 mm. The maximum incident angle is now very close to the critical value, and the TM reflection coefficient does indeed cross the zero value.

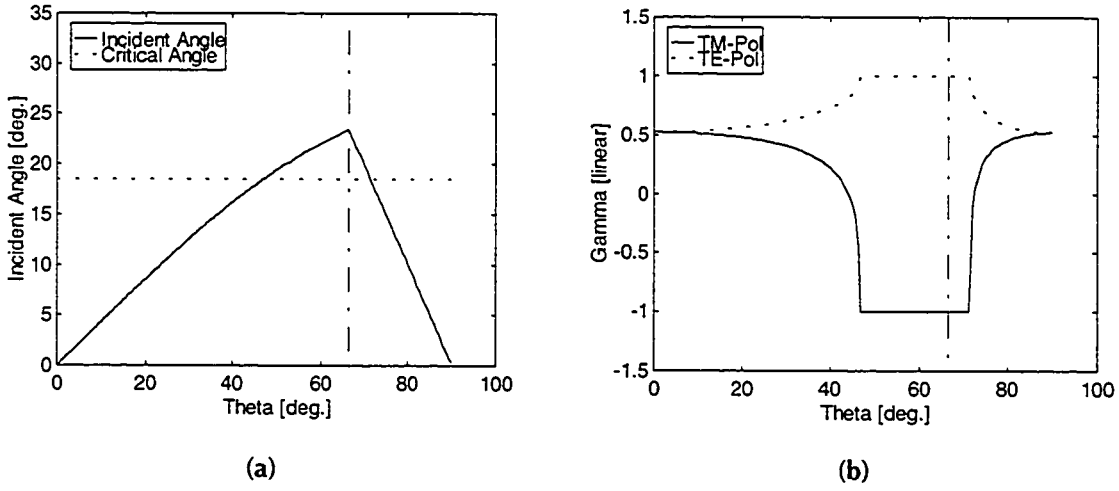

Figure 39: (a) Incident Angle and (b) Reflection Coefficient for $R_{lens} = 1\lambda_0$, $\varepsilon_r = 10$, and $L_E = 13$ mm

Increasing the extension to 13 mm causes the incident angle to surpass the critical angle near the hemisphere-to-cylinder transition. The cause of the steep rise in the reflection loss in Figure 35 is

now understood as being caused by the total internal reflection of the rays that are incident at angles that are greater than the critical angle. The effect is even more pronounced in Figure 40, which is for an extension of 15 mm.

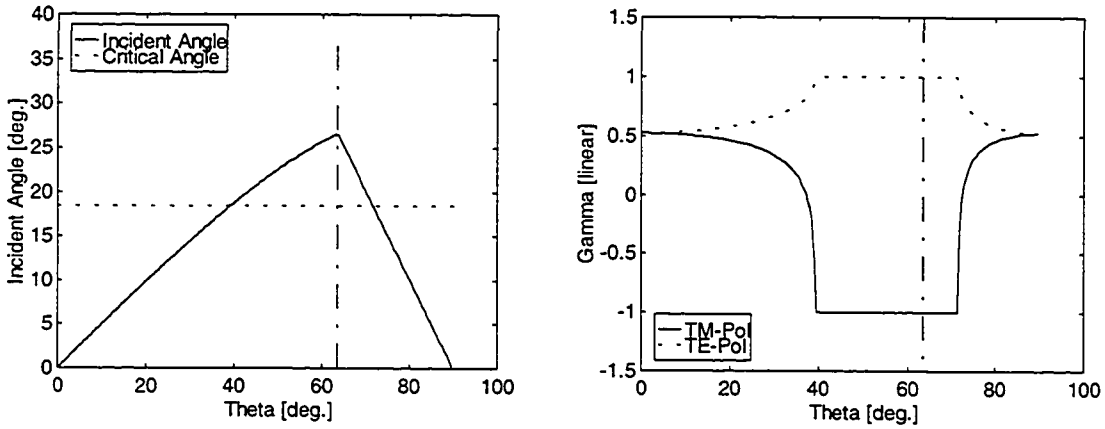

(a) (b)

Figure 40: (a) Incident Angle and (b) Reflection Coefficient for $R_{lens} = 1\lambda_0$, $\varepsilon_r = 10$, and $L_E = 15$ mm

Recapping, the reflection loss curve steadily decreases as the extension length is increased up to 10 mm because the incident angles of the predominantly TM-polarised rays are approaching the Brewster angle. However, the minimum reflection loss is short-lived as the extension length is further increased. Referring back to Figure 34, this is evidently due to the zero of the TM reflection coefficient being on the portion of the curve that is asymptotically approaching -1. This occurs because the Brewster angle is very close to the critical angle. Therefore, as the extension length is increased beyond 10 mm, total internal reflection begins to dominate, causing the sudden increase in the reflection loss.

The reflection loss curves for lens radii of 1, 2, 3, and $5\lambda_0$ have been plotted in Figure 41.

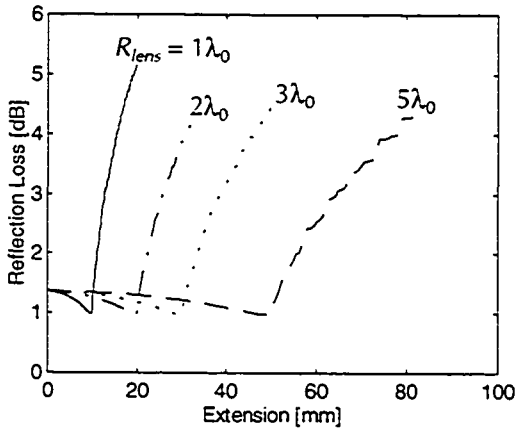

Figure 41: Reflection Loss Curves for Four Lens Radii, $\varepsilon_r = 10$

Interestingly, the RL minima occur shortly after the respective hyperhemispherical extensions of the lenses, regardless of the radius. Note that the ripples in some of the curves are sampling artifacts. The curves are actually not a function of the lens radius: normalising the independent axes by their respective lens radii (L_E / R_{lens}), the curves converge to the one in Figure 42.

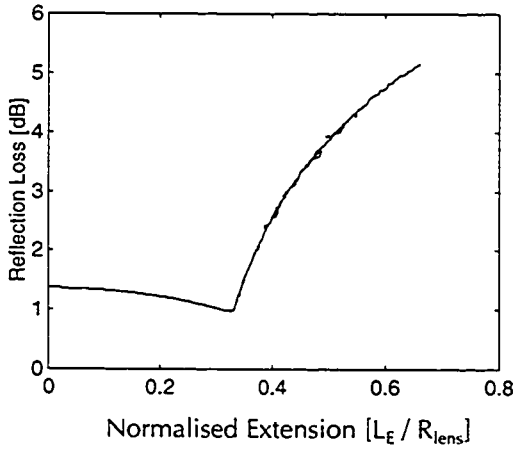

Figure 42: Normalised Reflection Loss Curves, $\varepsilon_r = 10$

Referring to Table 5, the minimum reflection loss occurs at 1.03 times the hyperhemispherical position, while fully half of the incident power is reflected at the elliptical position.

Figure 43 displays the reflection loss curves for lenses that have permittivities of: 2.3, 10, 11.7 and 40.

Extension Name	Extension Length (L_E)	Reflection Loss [dB]
Minimum Reflection Loss	$0.3250 \cdot R_{lens}$	0.9770
Hyperhemispherical	$0.3162 \cdot R_{lens}$	0.9867
Elliptical	$0.4290 \cdot R_{lens}$	3.020

Table 5: Reflection Losses at Important Extension Length Values, $\varepsilon_r = 10$

As expected, Figure 43 indicates that the reflection loss worsens as the permittivity is increased. The magnitude of the dip in the reflection loss also appears to be a function of the lens' permittivity.

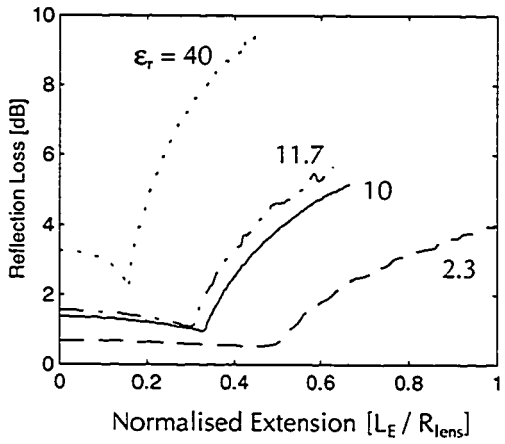

Figure 43: Reflection Loss for Various Lens Permittivities

However, although the reflection loss of a higher permittivity lens dips down lower relative to its $L_E = 0$ value, the drop does not make up for the overall higher reflection loss values. Table 6 lists the relevant data for all four curves.

Permittivity (ε_r)	Extension Name	Extension Length	Reflection Loss [dB]
2.3	Minimum Reflection Loss	$0.453 \cdot R_{lens}$	0.534
	Hyperhemispherical	$0.447 \cdot R_{lens}$	0.534
	Elliptical	$0.667 \cdot R_{lens}$	2.41
10	Minimum Reflection Loss	$0.325 \cdot R_{lens}$	0.977
	Hyperhemispherical	$0.316 \cdot R_{lens}$	0.987
	Elliptical	$0.429 \cdot R_{lens}$	3.02
11.7	Minimum Reflection Loss	$0.300 \cdot R_{lens}$	1.09
	Hyperhemispherical	$0.292 \cdot R_{lens}$	1.10
	Elliptical	$0.392 \cdot R_{lens}$	3.18
40	Minimum Reflection Loss	$0.160 \cdot R_{lens}$	2.13
	Hyperhemispherical	$0.158 \cdot R_{lens}$	2.17
	Elliptical	$0.208 \cdot R_{lens}$	5.00

Table 6: Reflection Losses at Important Extension Lengths for Four Lens Permittivities

The minimum reflection loss always occurs slightly after the hyperhemispherical extension length. It also appears as though the reflection losses can be made relatively small for extensions that are close to the hyperhemispherical position. The reflection losses for high lens permittivities, however, remain relatively large regardless of the extension length. Figure 44 shows the reflection losses at the hyperhemispherical and elliptical positions versus the permittivity of the lens.

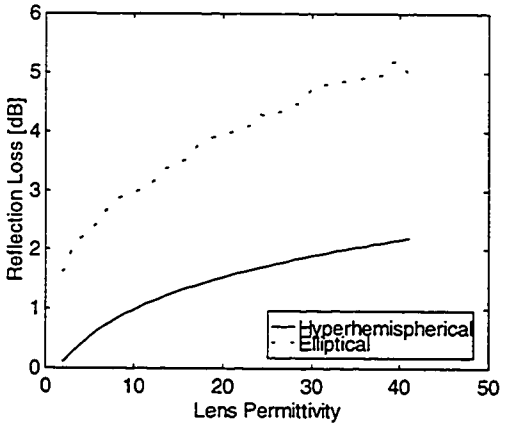

Figure 44: Reflection Loss at the Elliptical and Hyperhemispherical Extension Lengths

Therefore, a compromise exists between the reflection loss and the directivity of the lens when no matching layer is applied. A further compromise must also be made between the reflection loss and the front-to-back radiation ratio, for a low permittivity lens allows a greater amount of power to be radiated via the backside of the substrate. The lenses that are to be measured experimentally have extensions that correspond to the hyperhemispherical position. The reflection loss for these $\varepsilon_r = 10$ lenses will therefore be approximately 1 dB; in other words, 20% of the radiation will be scattered. It remains to be seen if this percentage is high enough to negate the validity of the simulated radiation pattern results that preceded this section.

5.7 First Reflection Effects

The impedance mismatch at the lens-to-air interface causes some of the incident energy to be reflected back inside the lens. The effect of one such reflection on the radiation pattern will now be considered. Specifically, only rays that are reflected back onto the hemispherical part of the lens will be analysed. Tracing the path of these reflected rays is not a trivial task. Although the term "ray tracing" suggests that a Geometrical Optics analysis is used to characterise the radiation, this is not entirely true. The rays serve to delimit the boundaries of the rectangular flux tubes that emanate from a point source. Within each tube is a localised plane wave containing a finite amount of power. The opening of the tube is characterised by a constant amplitude and a constant phase, both calculated at the center of the tube's opening using Physical Optics.

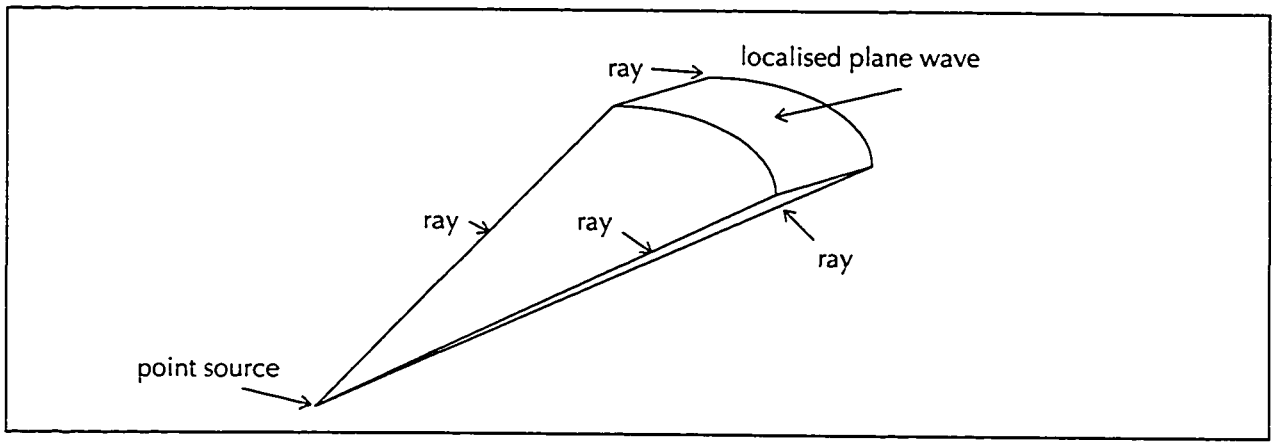

Figure 45: Flux Tube Definition

To define the flux tubes, the lens surface is decomposed into a quasi-rectangular mesh. For a given lens geometry, theta is first quantized yielding an annular structure. These rings are then decomposed by descretising phi, yielding an igloo-like mesh. These two steps are visualised in Figure 46.

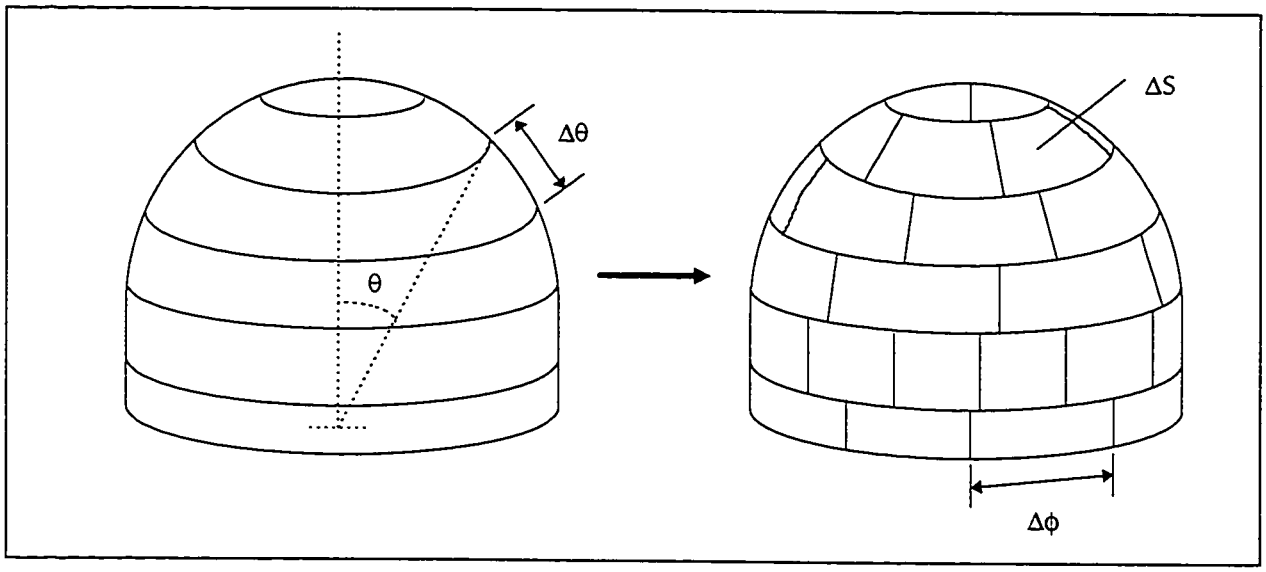

Figure 46: Lens Meshing

Associated with every surface element ΔS are four rays, each intersecting the lens surface at the corners of the quasi-rectangle. The angles of incidence of the rays in the theta-plane at the lens-to-air interface are generally not normal to the surface. These angles vary as a function of the launch angle θ. Therefore, the

rays defining a flux tube are either divergent or convergent after the reflection. This is depicted in the two-dimensional constant-phi plane in Figure 47.

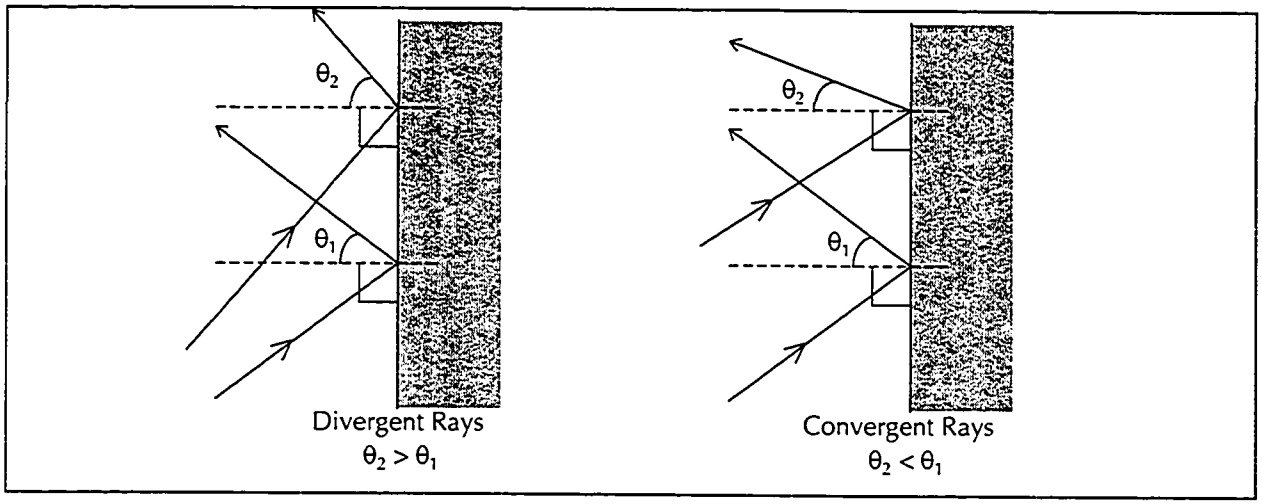

Figure 47: Flux Tube Variation after Reflection

However, the power contained in the tube must remain constant. Hence, the magnitude of the electric field inside the flux tube does not remain constant. It will be shown that the electric field magnitude is a function of the flux tube's area ΔS. Although a general theory pertaining to reflected flux tubes exists [73,74], the geometry at hand allows a more specific solution to be applied.

In the text that follows, the term *primary flux tube* refers to a flux tube that originates from the slot (the point source) and that intersects the lens surface. The term *secondary flux tube* refers to a tube that has been once reflected from the lens surface and will subsequently intersect the lens structure at another location. Now consider the reflection of a flux tube in the phi-plane. The lens, viewed from its zenith, appears as a two dimensional circle for any constant-theta plane cut along the z-axis. This is depicted in Figure 48.

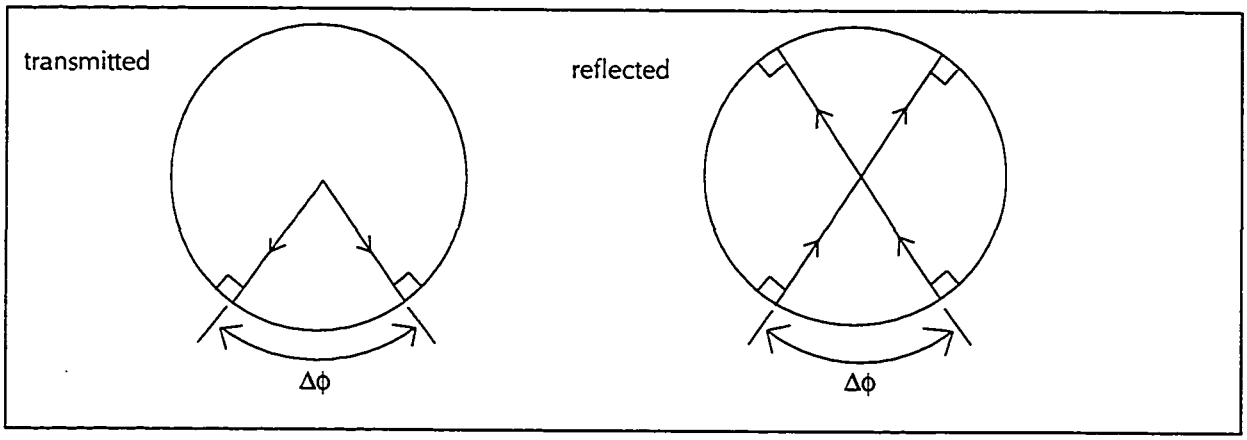

Figure 48: Lens Geometry in the ϕ-plane Viewed From Lens Apex

Assuming that two rays originate from a point source centered at the base of the lens, their angular separation at the lens surface can be defined by $\Delta\phi$. Since both rays arrive at normal incidence as viewed from the lens apex, the reflection is symmetric: the reflected rays intersect each other at the center of the lens. The reflected rays intersect the lens surface for the second time with the same angular separation $\Delta\phi$, regardless of their direction in θ.

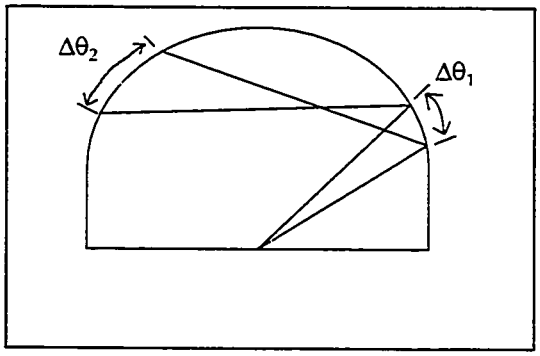

Figure 49: Theta-Plane Reflection

Unfortunately, the reflection in the constant-phi plane is not as straightforward. Referring to Figure 49, the angular separation of the secondary tube is not the same as that of the primary tube. However, the relationship between $\Delta\theta_1$ and $\Delta\theta_2$ can readily be found using basic geometry.

An incident ray launched at an angle θ intersects the hemisphere at a point $[x'_p, z'_p]$. The geometry of the problem is given in Figure 50.

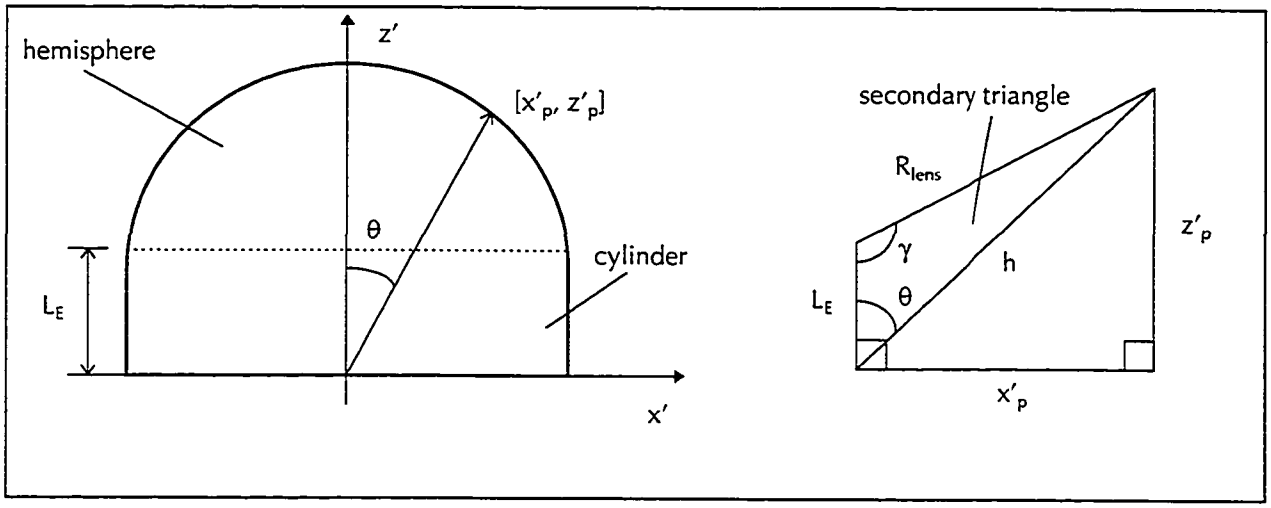

Figure 50: Theta-plane Geometry

The intercept point on the hemisphere is defined as:

$$x'_p = h\cos\left(\frac{\pi}{2}-\theta\right) = h\sin\theta \quad \text{and} \quad z'_p = h\sin\left(\frac{\pi}{2}-\theta\right) = h\cos\theta\,, \tag{5-8}$$

where the hypotenuse h is found by using the sine rule on the secondary triangle:

$$\frac{R_{lens}}{\sin\theta} = \frac{h}{\sin\gamma} \qquad \therefore h = \frac{R_{lens}\sin\gamma}{\sin\theta}\,, \tag{5-9}$$

and where the angle γ is readily found by applying the cosine rule. If the ray is incident upon the cylinder ($z'_p < L_E$), then the intercept point is simply:

$$x'_p = R_{lens} \qquad \text{and} \qquad z'_p = R_{lens}\tan\theta\,. \tag{5-10}$$

Next, the angle of incidence (and reflection), θ_i, must be found. The unit normal on the surface of the hemisphere is given by:

$$\hat{n} = \frac{\left[x'_p, z'_p\right] - \left[0, L_E\right]}{\left\|\left[x'_p, z'_p\right] - \left[0, L_E\right]\right\|}\,, \tag{5-11}$$

and it is simply $\hat{n} = \hat{x}'$ on the cylinder. The angle of incidence is therefore $\theta_i = \arccos\left(\hat{n}\cdot\bar{i}\right)$, where the incident vector $\bar{i}$ points from the origin to the intercept point:

$$\bar{i} = \frac{\left[x'_p, z'_p\right] - \left[0, 0\right]}{\left\|\left[x'_p, z'_p\right] - \left[0, 0\right]\right\|}\,. \tag{5-12}$$

Figure 51 indicates the required geometry.

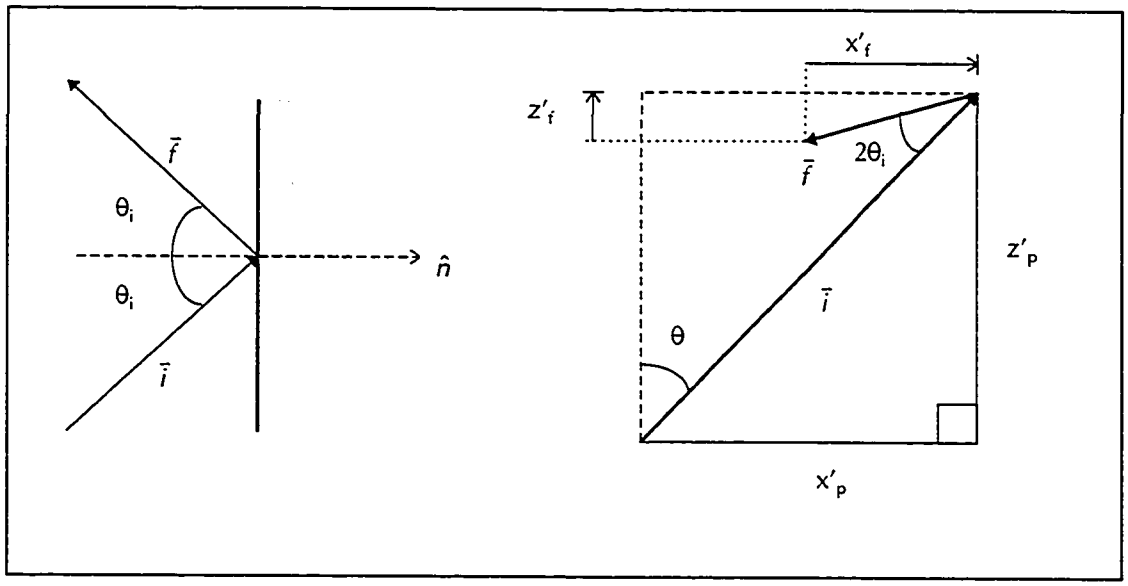

Figure 51: Reflection Geometry

Next, the parametric equations of the reflection vector $\vec{f}$ are derived. The x' component of $\vec{f}$ is:

$$x'_f = -\cos\left(\frac{\pi}{2} - \theta - 2\theta_i\right), \tag{5-13}$$

and its z' component is given by:

$$z'_f = -\sin\left(\frac{\pi}{2} - \theta - 2\theta_i\right). \tag{5-14}$$

Note that z'_f can be positive when $2\theta_i > (\pi/2 - \theta)$. The parametric equations of the reflected ray are therefore

$$\begin{cases} x' = x'_p + x'_f u \\ z' = z'_p + z'_f u \end{cases}, \tag{5-15}$$

where u is an independent variable. The two dimensional equation of the circle representing the hemisphere is:

$$x'^2 + (z' - L_E)^2 = R_{lens}{}^2. \tag{5-16}$$

Substituting x' and z' from the parametric equations into the equation for the circle, the system can be solved for u to find the next intercept point on the circle. Substituting,

$$\left(x'_p + x'_f u\right)^2 + \left(z'_p + z'_f u - L\right)^2 = {R_{lens}}^2$$
$$x'_p{}^2 + 2x'_p x'_f u + \left(x'_f u\right)^2 + z'_p{}^2 + 2z'_p z'_f u - 2z'_p L + \left(z'_f u\right)^2 - 2z'_f uL + L^2 - {R_{lens}}^2 = 0 \qquad \textbf{(5-17)}$$
$$u^2\left(x'_f + z'_f\right) + u\left(2x'_p x'_f + 2z'_p z'_f - 2z'_f L\right) + \left(x'_p{}^2 + z'_p{}^2 - 2z'_p L + L^2 - {R_{lens}}^2\right) = 0 \ .$$

The roots of the quadratic equation in u are then found numerically. For $[x'_p, z'_p]$ on the hemisphere, these roots must consist of one nil and one non-nil value (the nil value is because $[x'_p, z'_p]$ already lies on the circle). The non-nil root therefore gives the next intercept point with the circle.

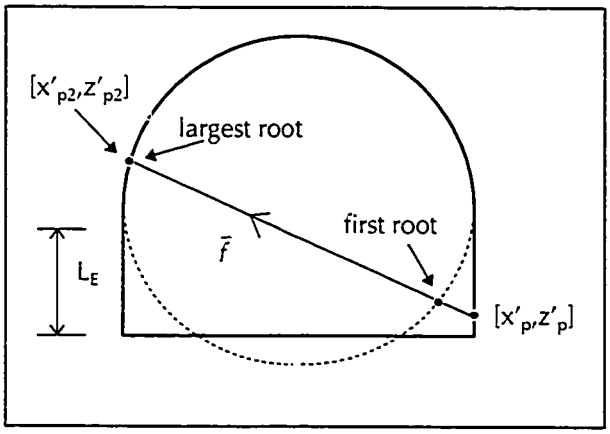

Figure 52: Roots When the Reflection Point is on the Cylinder

For $[x'_p, z'_p]$ on the cylinder, the quadratic equation will yield two non-nil roots. The largest root indicates the next valid intercept point with the hemisphere, as shown in Figure 52. Once the proper roots in u have been selected, they are substituted back into the parametric equation of $\bar{f}$ to find the next intercept points x'_{p2} and z'_{p2}. This is done for all of the theta launch angles.

As previously stated, only the secondary flux tubes that fall entirely on the hemispherical surface of the lens will be considered in this section. To select such a tube, the two rays which delimit the tube must both fall on the hemisphere, as illustrated in Figure 53

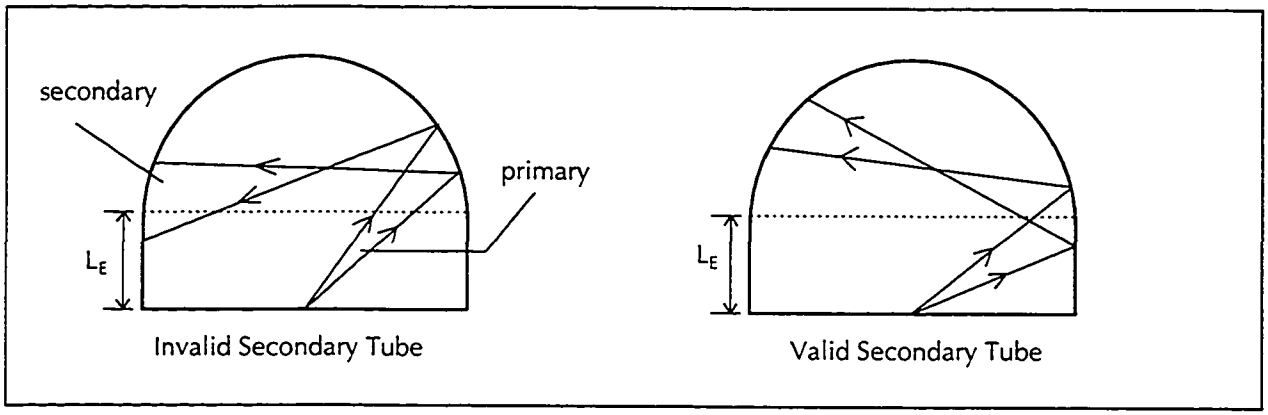

Figure 53: Flux Tube Criteria

To calculate the new areas ΔS_2 of the secondary flux tubes, the angular difference between the rays in both the theta- and phi-planes must be known. Since the z'_{p2} values are now known, the following geometry may be used in the constant-phi plane.

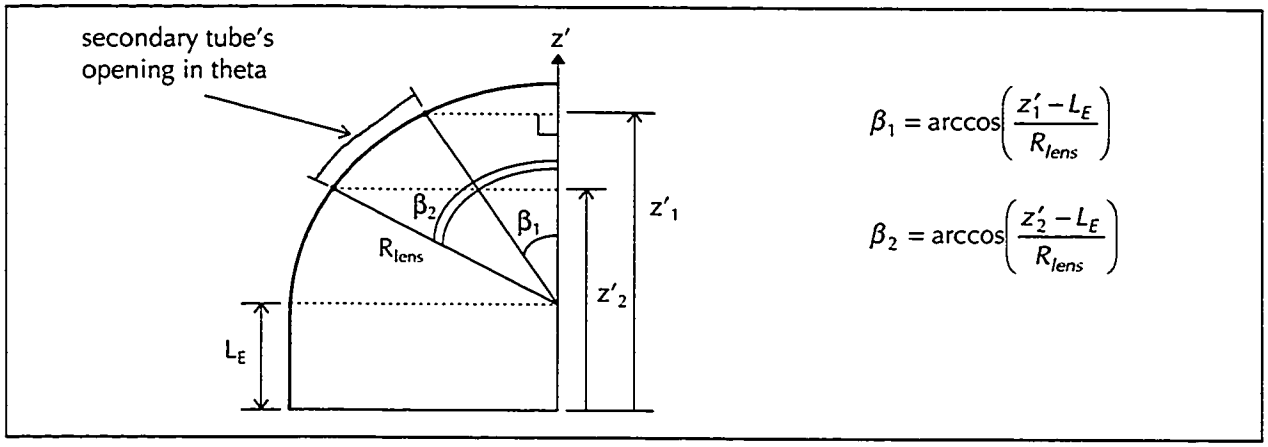

Figure 54: Geometry for the Calculation of the Secondary Tube's Area at the Lens Surface

The definition of the new β variable permits the use of spherical coordinates to calculate the area of the secondary tube's opening at the lens surface. The new spherical coordinates are centered at the base of the hemisphere. Since the angular difference in the constant-theta plane is already known, the area of the flux tube's opening is:

$$\begin{aligned} \Delta S_2 &= \iint r^2 \sin\beta \, d\beta \, d\phi \\ &= R_{lens}{}^2 (\Delta\phi)[-\cos\beta_2 + \cos\beta_1]. \end{aligned} \qquad \textbf{(5-18)}$$

As previously stated, the power in the output of the secondary flux tube must equal the input power of the secondary flux tube, which is related to the power of the primary flux tube via the reflection coefficients (neglecting the losses of the dielectric lens). The power in the primary flux tube is:

$$P_1 = \Delta S_1 \frac{|E_f|^2}{2Z_d}, \tag{5-19}$$

where ΔS_1 is the area of the primary flux tube's opening at the lens interface, $|E_f|$ is the magnitude of the reflected electric field taken evaluated in the middle of the primary flux tube, and Z_d is the characteristic impedance inside the dielectric lens. The magnitude of the electric field at the secondary flux tube's opening on the lens surface is calculated by the rule of power conservation:

$$\begin{aligned} P_2 = \Delta S_2 \frac{|E_2|^2}{2Z_d} = P_1 = \Delta S_1 \frac{|E_f|^2}{2Z_d} \\ \therefore |E_2| = \sqrt{\frac{P_1(2Z_d)}{\Delta S_2}} = |E_f| \sqrt{\frac{\Delta S_1}{\Delta S_2}}. \end{aligned} \tag{5-20}$$

Therefore, the electric field at the secondary flux tube's opening is given by the reflected field at the primary flux tube's opening, scaled by the factor given above and phased by the distance Δd between the two openings:

$$\vec{E}_2 = \sqrt{\frac{\Delta S_1}{\Delta S_2}} \vec{E}_f \exp(jk_d \Delta d), \tag{5-21}$$

where k_d is the phase constant inside the lens. Now that the secondary flux tube's electric field is known, it is again refracted at the lens-to-air interface so that its contribution to the radiation pattern can be determined.

Figure 55 shows the calculated radiation pattern for the $3\lambda_0$-radius hyperhemispherical lens with and without the secondary ray tube calculation. Both the co-polarised and cross-polarised electric fields are shown in the two principle planes. The curves with the solid lines represent the radiation patterns without the secondary ray tubes, and the dashed lines represent the radiation patterns with the secondary ray tubes. The

plots are normalised to the maximum co-polarised value in their respective plane calculated without the secondary ray tubes.

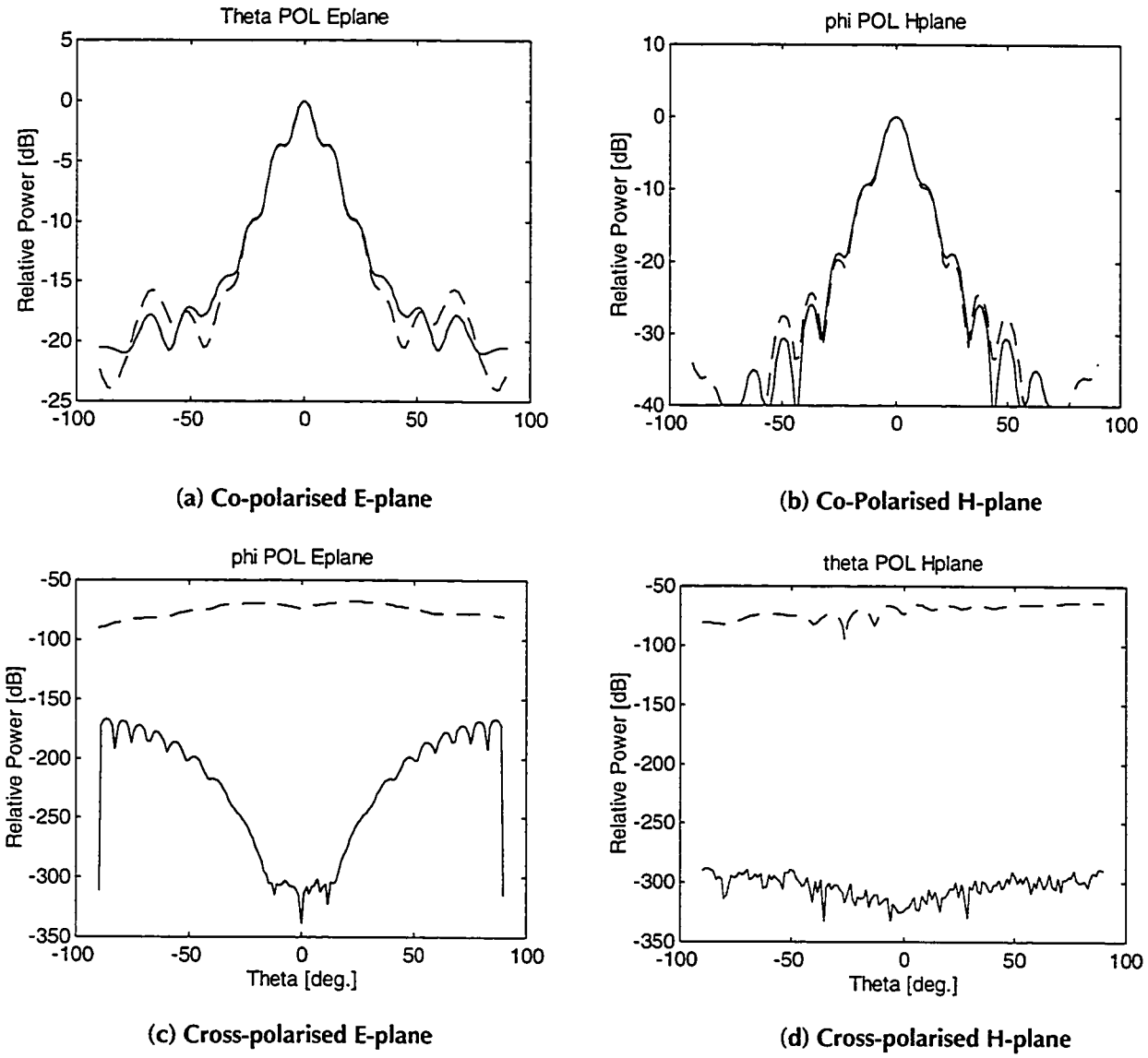

(a) Co-polarised E-plane

(b) Co-Polarised H-plane

(c) Cross-polarised E-plane

(d) Cross-polarised H-plane

Figure 55: First Reflection's Effect on the Radiation Pattern of a $3\lambda_0$-radius Hyperhemispherical Lens

(——) Patterns taken without the secondary ray tubes

(- - - -) Patterns taken with the secondary ray tubes

The results indicate that the co-polarised fields differ only by their sidelobes. However, the first reflection has a significant effect on the cross-polarised fields. Indeed, without the reflection effect, the cross-polarisation is insignificant. This is due to the ideally-polarised excitation source current in the slot antenna. The results show that internal reflections inside the lens will increase the cross-polarisation levels. It should be noted that these far-field cross-polarisation levels have been computed with an ideally polarised source. Actual slots support cross-polarised currents that are likely to cause significantly higher cross-polarisation levels in the far-field.

It is also of interest to note the change in the reflection loss level inside the lens. Prior to the second reflection, the reflection loss was equal to 1 dB, indicating that 20% of the radiation incident upon the lens is reflected. After the second reflection calculation, the reflection loss decreases slightly to 0.91 dB, or 18.9% reflected. Hence, the ray tubes that are entirely incident upon the hemisphere subsequent to their first reflection do not transfer much of their power through the lens and into space. This power undergoes subsequent reflections and is either absorbed by the dielectric, absorbed by the slot through reaction, or is transmitted through the lens at other points. Figure 56 illustrates the theta-rings in the theta-plane that contributed to the secondary reflection and the locations of the secondary flux tube openings.

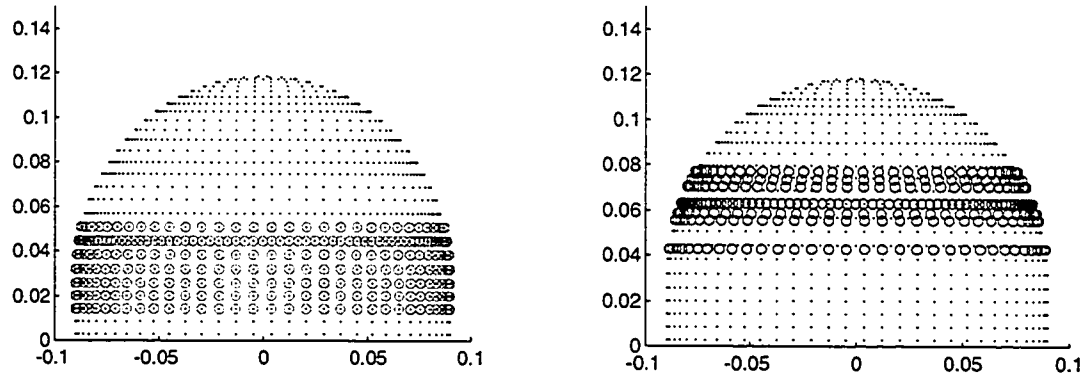

(a) Reflection Sources **(b) Reflection Destinations**

Figure 56: Primary and Secondary Ray Locations

5.8 Simulation Results - Conclusion

The hybrid simulations that were performed for slot-fed SLAs have yielded many useful results. In Section 5.3 and Section 5.4, it was shown that although the PO lens illumination yields more precise results than the GO illumination, the difference in the resulting SLA radiation patterns are minimal for single and double slot feeds. This result does not preclude the use of the PO propagators as illuminators; in Section 5.1 it was shown that the PO propagators more accurately predict the near-field radiation patterns of double-slot arrays. This will hold true for any array feed configuration. Therefore, the PO illumination is a useful tool for determining the validity of GO illumination for array feeds in the near-field.

In Section 5.5, the hybrid simulator was used to calculate the directivities of single slot-fed SLAs. These results, displayed in Figure 33, serve as useful design curves for building single slot-fed SLAs. Although the directivity is specified, it may not accurately reflect the gain of the SLA for a lens with no matching cap layer is susceptible to reflection loss at the lens-to-air interface. In Section 5.6, the hyperhemispherical extension lens was shown to provide far less reflection loss than the elliptical extension lens. Hence a compromise exists between the directivity and the reflection loss of lenses without matching layers. Figure 43 provided reflection loss data as a function of extension length for various lens permittivities.

Finally, in Section 5.7, the effects on the SLA radiation pattern from one internal reflection was determined. The results indicated that the reflections will perturb the sidelobes and raise the cross-polarisation levels. Minimal power was transmitted through the lens on the second reflection, indicating that much of the reflected power undergoes multiple internal reflections inside the lens before being absorbed or transmitted. However, the one-way nature of the hybrid simulator prohibits accurate tracing of subsequent reflections.

6. Experimental Design and Measurements

This chapter is devoted to the experimental aspects of this thesis. The theoretical work required to design the slot antennas, lenses and test jig is first presented. The measured impedances and radiation patterns of the various assemblies are then documented.

6.1 Feed Antenna Design

6.1.1 Design of the Free-Space Slot Antenna

A 10 GHz single slot antenna serves as the experimental feed antenna for this project. The slot is printed on the ground plane of a Rogers 10i substrate, which has a permittivity of $\varepsilon_r = 9.8$ and a dielectric thickness of 15 mils. To excite the slot, it is electromagnetically coupled [75-79] to an open-circuited microstrip transmission line. The geometry of the structure is depicted in Figure 57.

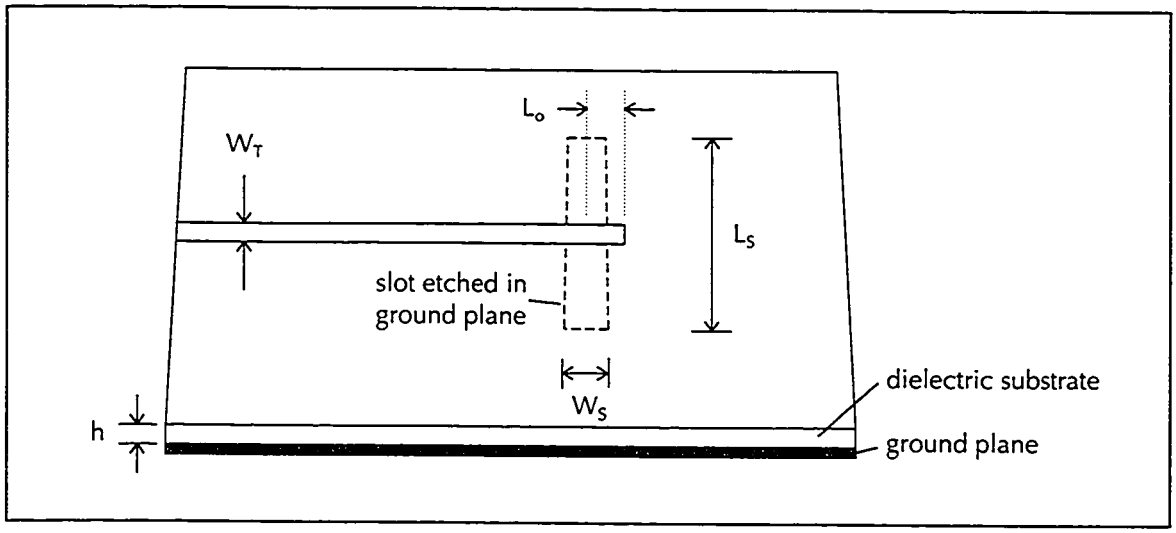

Figure 57: Microstrip Coupled Slot Antenna Geometry

As indicated, h is the thickness of the substrate, W_T is the width of the microstrip transmission line, W_S is the width of the slot, L_S is the slot length, and L_o is the length of the open-circuited stub. Although some similar reported structures measure the stub length from the edge of the slot [79,80],

it will be seen that measuring the stub from the center of the slot [78,81,82] agrees well with the electrical model of the circuit that will be given later in this section.

Dielectric substrates are excellent surface waveguides that have a fundamental mode with no cutoff. By ensuring that the substrate thickness is a small fraction of the free-space wavelength, the amount of power coupling to the substrate modes can be minimized [4]. For the case at hand,

$$\frac{h}{\lambda_0} = \frac{381(10^{-6})}{30(10^{-3})} = 0.0127.$$

By comparing this result to Figure 58 below, it can be seen that negligible power will be coupled to substrate modes.

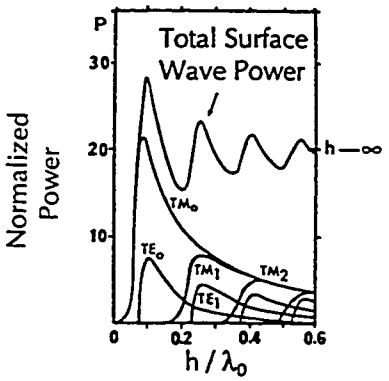

Figure 58: Power Fraction Coupled to Substrate Modes as a function of h/λ_0 on Silicon or GaAs

The slot antenna has been designed at the Communications Research Center (CRC) using Ensemble Design 4.1, a microwave circuit simulation package. To obtain a 50 Ω feed line, the microstrip transmission line's width is estimated to be W_T = 0.3712 mm, yielding an effective permittivity of ε_{eff} = 6.541 and a guided wavelength of λ_g = 11.173 mm. To de-embed the slot impedance during subsequent simulations, the length of the transmission line is set to an integral number of guided wavelengths from the center of the slot. Impedance measurements are then taken at the edge of this transmission line.

According to theory [54], the microstrip coupled slot is modeled as a cascade connection of a series impedance modelling the slot and of the input impedance of the stub, as illustrated in Figure 59.

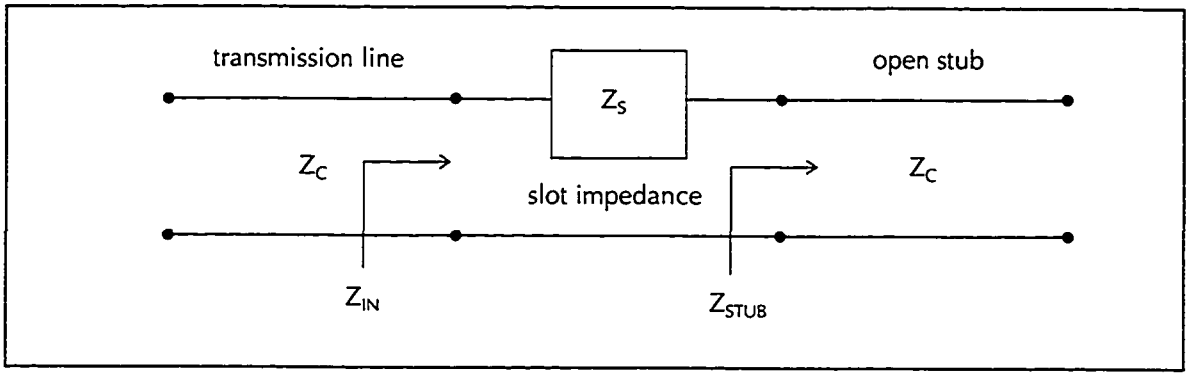

Figure 59: Equivalent Circuit of the Microstrip Coupled Slot

The input impedance is simply the addition of the slot and open stub impedances:

$$Z_{IN} = Z_S + Z_{STUB}. \tag{6-1}$$

From transmission line theory, the impedance of an open-circuited stub is a pure reactance:

$$Z_{STUB} = jX_{STUB} = -jZ_C \cot(\beta L_o), \tag{6-2}$$

where Z_C is the characteristic impedance of the transmission line and β is its phase constant. The phase constant is evaluated as the following:

$$\beta = \omega\sqrt{\mu_0\varepsilon_0\varepsilon_{eff}} = 2\pi 10(10^9)\sqrt{4\pi(10^{-7})8.854(10^{-12})(6.541)} = 536.0146 \text{ [rad/m]}.$$

The resulting open stub impedance, which is periodic every $\lambda_g/2$, is plotted in Figure 60.

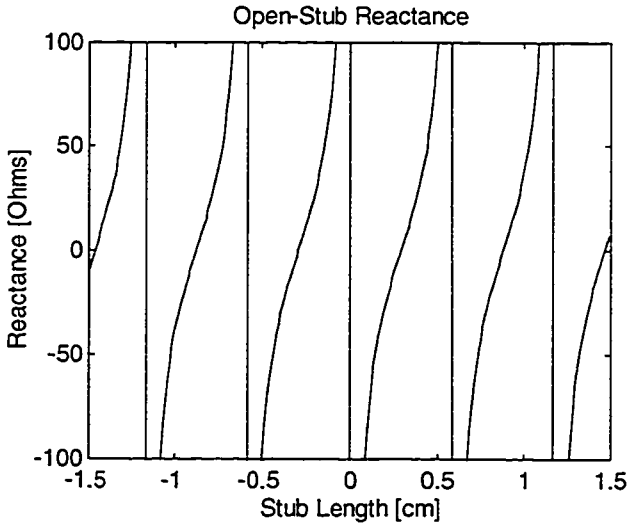

Figure 60: Open-Circuited Stub Reactance

To validate the equivalent circuit representation, a free-space slot antenna is first designed. This antenna will serve only as a test and is not intended to be loaded with a dielectric lens. After performing several iterations, an impedance of Z_{IN} = 45 + j93 Ω was obtained for $L_S = 0.65\lambda_g = 0.762$ cm, $W_S = 0.10\lambda_g = 0.12$ cm and $L_o = W_S/2$ (the stub extends to the far edge of the slot). Since the resistive component is close to 50 Ω, an attempt to cancel the reactance is made. The reactance of 93 Ω is the sum of the slot and stub reactances. To isolate the slot reactance, the stub reactance is subtracted:

$$\begin{aligned} X_{IN} = 93\Omega &= X_{SLOT} + X_{STUB} \\ \therefore X_{SLOT} &= X_{IN} - X_{STUB} \\ &= 93 + 50\cot\left(536.0146 \bullet 0.06\left(10^{-2}\right)\right) \\ &= 93 + 150 \;=\; 243\ [\Omega]\ . \end{aligned}$$

To cancel this inductive reactance, the length of the stub must be increased to:

$$L_o = \frac{\arctan\left(\frac{50}{243}\right)}{\beta} + N\frac{\lambda_g}{2} = 0.038 \;+\; (1)\frac{\lambda_g}{2} = 0.624\ [\text{cm}],$$

where N can be any positive integer that ensures that the stub length is at least as long as half of the slot width, $W_S/2$ = 0.06 cm. Choosing N = 1 gives L_o = 0.624 cm. Although this particular slot design was not chosen in the end, subsequent simulations have been done for various stub lengths in order to further verify the theory of the equivalent circuit. Furthering the verification will also show whether the stub's reference plane should be taken on the edge of the slot or at its center. The Ensemble simulation results, which are taken to be absolutely correct, are listed in Table 7 and are plotted on the Smith Chart in Figure 61.

Stub Length [cm]	Input Impedance [Ω]
0.06	45 + j93
0.11	38 + j156
0.26	36 + j206
0.36	35 + j223
0.46	35 + j247
0.56	39 + j362
0.61	76 - j233
0.64	38 + j84
0.66	36 + j128

Table 7: Simulated Input Impedance Versus Stub Length

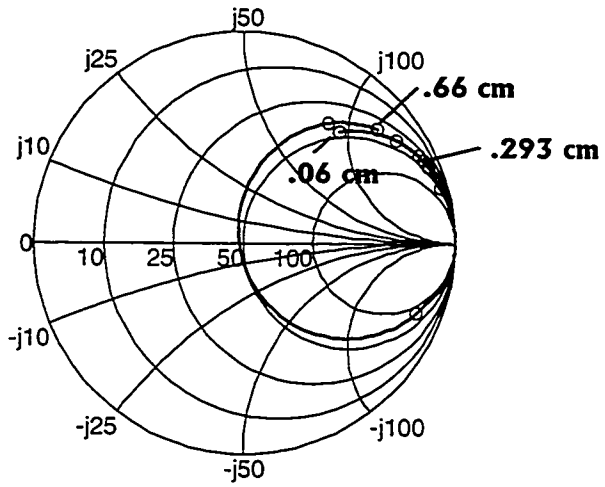

Figure 61: Simulated Input Impedance Versus Stub Length for a Microstrip Coupled Slot

The impedance curve roughly follows the 50 Ω resistance locus as the stub length is varied. Its corresponding input reactance values have been numerically fitted to the theoretical reactance curve of an open stub and slot combination, Equation (6-1), by using a least squared error algorithm. The results are displayed in Figure 62. Two degrees of freedom are available to the curve fitting: varying X_{SLOT} translates the curve vertically, while varying the stub's reference position (nominally taken at the center of the slot) translates the curve horizontally.

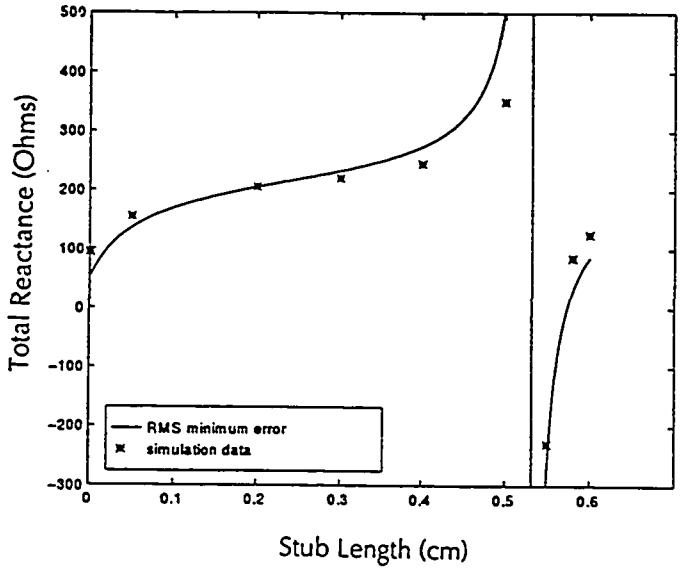

Figure 62: Least Squared Error Curve Fitting of the Slot and Open Stub Reactance

The minimum error is obtained when $X_{SLOT} = 215\ \Omega$ and the stub's reference position is shifted by $\Delta L_o = -0.005$ cm. The new slot reactance is the best fit for all of the data points taken together, and the very small stub length adjustment ($\Delta L_o \approx 0$) indicates that the center of the slot is indeed the proper location at which to reference it. Although the simulated data points do not lie exactly on the ideal reactance curve, the equivalent circuit closely approximates the true nature of this circuit.

It is of interest to note that the fitted slot reactance of $X_{SLOT} = 215\ \Omega$ very nearly coincides with the reactance that is found at the stub length of $L_o = \lambda_g/4 = 0.293$ cm. Indeed, by setting the stub length to $\lambda_g/4$, its reactance is nulled out, allowing the design to depend only on two variables, namely L_S and W_S, the slot dimensions. Although this allows the slot to be designed at self-resonance, which can dramatically increase its impedance bandwidth [1], there is no guarantee that the resonant resistance will be near the desired input resistance.

The specifications that have been chosen for the free-space 10 GHz test antenna are: $L_S = 0.7$ cm and $L_o = W_S/2$. Although arbitrary, it was decided to keep the stub length flush with the edge of the slot. The resulting input impedances are listed in Table 8 and Table 9, and plotted in Figure 63 as a function of W_S and as a function of the frequency when $W_S = 0.07$ cm.

Slot Width [cm]	Z_{IN} [Ω]
0.03	101 - j39.4
0.07 (best match)	49.6 - j2.78
0.08	43.7 + j2.12
0.10	34.9 + j26.3

Table 8: Simulated Input Impedance vs. Slot Width for $L_S = 0.7$ cm, $L_o = W_S/2$ and $f = 10$ GHz

Frequency [GHz]	Z_{IN} [Ω]
9.6	62.4 - j90.8
9.7	50.0 - j62.9
9.8	44.9 - j41.4
9.9	44.6 - j23.6
10.0	49.5 - j2.8
10.1	57.5 + j7.7
10.2	75.0 + j21.3
10.3	107 + j27.7
10.4	134 + j48.4

Table 9: Simulated Input Impedance vs. Frequency for $L_S = 0.7$ cm, $W_S = 0.07$ cm and $L_o = W_S/2$

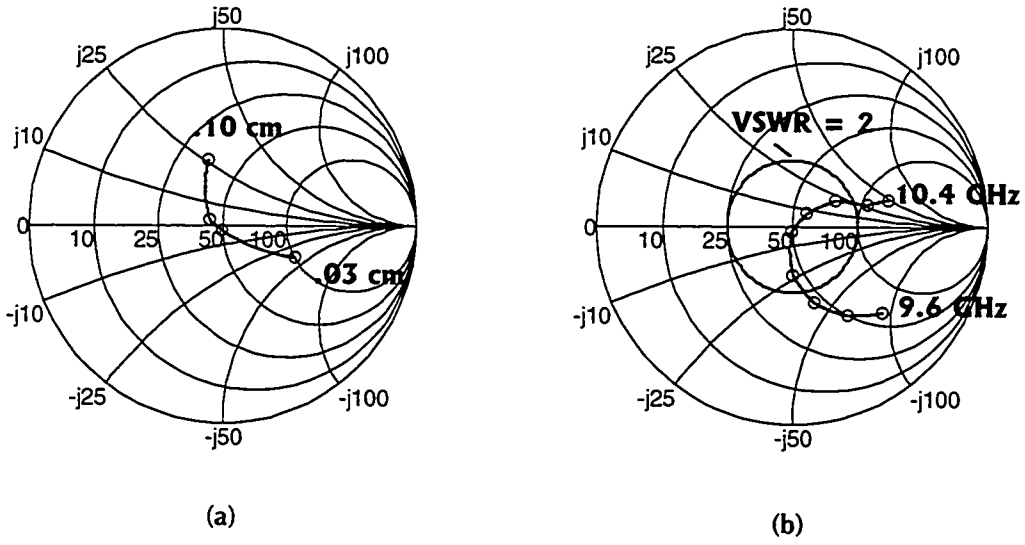

Figure 63: (a) Impedance vs. Slot Width on the Smith Chart at 10 GHz, (b) Impedance vs. Frequency for $W_S = 0.07$ cm

The 2:1 voltage standing wave ratio (VSWR) circle has also been plotted in Figure 63 and indicates that the free-space slot has a 4% bandwidth, which is typical of substrate antennas [1].

6.1.2 Design of the Scaled Slot Feed Antenna

Having designed the free-space test slot, attention is now focused on the design of the slot that will be used with the dielectric lenses. As will be seen, it is a scaled version of a free-space slot, and is hereafter referred to as the *scaled slot.*

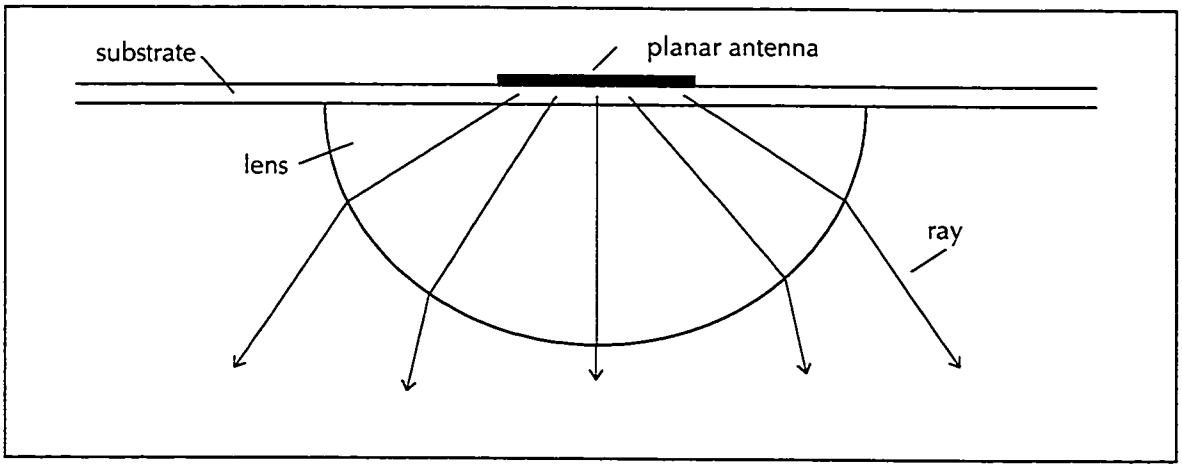

Figure 64: Substrate Lens Geometry

An ideal dielectric lens mounted on a dielectric substrate, shown in Figure 64, refracts all of the incident rays through the dielectric-to-air interface, thereby approximating an infinite dielectric half-space by eliminating all of the reflections that normally occur at this interface [2]. A dielectric half-space increases the static capacitance of the substrate antenna by a factor of the *mean dielectric constant,* ε_m [1,2,27]:

$$\varepsilon_m = \frac{\varepsilon_1 + \varepsilon_2}{2} = \frac{1+\varepsilon_r}{2}, \qquad \textbf{(6-3)}$$

where it is assumed that the lens of permittivity ε_r is mounted on a dielectric substrate of the same permittivity $\varepsilon_2 = \varepsilon_r$ and the substrate antenna borders on air on the opposite side ($\varepsilon_1 = 1$). By increasing the static capacitance, the quasi-static impedance of the antenna is reduced by the square

root of the mean dielectric constant [16,33], while its electrical length is increased by the same factor.

An underlying assumption in this thesis is that this relation will also be valid for antennas that are exposed to a dielectric half-space on one side and exposed to a very thin dielectric substrate on the other. This assumption must be made because the lenses *cannot* be mounted on the dielectric side of the substrate for microstrip coupled slots. Indeed, the addition of a lens on the substrate side would interfere with the transmission line. Therefore, all lenses must be placed on the ground plane side of the slot. This contrasts with all of the substrate lens antennas that have been documented. From a radiation point of view, the assumption should be accurate, since slot antennas on thin substrates radiate in a bi-directional manner [7]. Further, a recent publication [35] documents a similar aperture coupled microstrip lens antenna that has a front-to-back radiation ratio of 50 dB. Whether or not the simple scaling relationship will hold true from an impedance point of view remains to be seen.

The self-impedance and the required length of a slot antenna on a dielectric half-space are therefore reduced to:

$$Z_{SLOT}' = \frac{Z_{SLOT}}{\sqrt{\varepsilon_m}} = \frac{Z_{SLOT}}{\sqrt{\frac{1+\varepsilon_r}{2}}} \text{ and} \tag{6-4}$$

$$L_S' = \frac{L_S}{\sqrt{\varepsilon_m}} = \frac{L_S}{\sqrt{\frac{1+\varepsilon_r}{2}}}, \tag{6-5}$$

where Z_{SLOT} and L_S are the self-impedance and the length, respectively, of a slot antenna that is exposed entirely to free-space. The lens material that has been selected for this thesis has a permittivity of 10.0, which is close to the substrate's permittivity of 9.8 . Note however that the open-circuited stub, which is located on the dielectric side of the substrate, does not see the dielectric half-space since the latter is isolated by the ground plane. Hence, the stub reactance

remains unchanged by the addition of the lens. Ensemble Design 4.1 is unable to simulate slots on dielectric half-spaces; therefore, to obtain a 50 Ω input reactance after the lens is added on the ground plane, Equation 6-4 must be used, which yields a required free-space slot resistance of:

$$R_{SLOT} = 50\sqrt{\varepsilon_m} = 50\sqrt{5.5} = 117.26 \ [\Omega].$$

After performing several iterations on the computer, an input impedance of Z_{IN} = 116.43 + j2.09 Ω was obtained for a slot length of L_S' = 0.709 cm, a slot width of W_S' = 0.042 cm, and a stub length of $L_o = W_S/2$. The resistive component is within 0.7% of the desired 117.26 Ω at this point. The next step is to tune out the input reactance. It is already quite low, indicating that the stub is very close to canceling the positive reactance of the free-space slot. The reactance of the $W_S/2$ stub is:

$$X_{STUB} = -50\cot\left(536.0146 \bullet 0.021\left(10^{-2}\right)\right) = -442.32 \ [\Omega].$$

Therefore, the slot's self-reactance must be:

$$X_{SLOT} = X_{IN} - X_{STUB} = 444.41 \ [\Omega].$$

Once the lens is placed on the slot, this reactance should drop to:

$$X_{SLOT}' = \frac{444.41}{\sqrt{5.5}} = 189.50 \ [\Omega].$$

The stub must therefore contribute X_{STUB}' = -189.50 Ω of reactance, requiring a length of:

$$L_o' = \frac{\arctan\left(\frac{50}{189.50}\right)}{536.0146} = 481 \ [\mu m] \ = \ 0.0481 \ [cm].$$

Therefore, the input impedance of the combination of L_S, W_S and L_o' should yield a free-space resistance of approximately R_{IN}' = 117.26 Ω and a free-space reactance of $X_{IN}' = X_{SLOT}' + X_{STUB}'$ = 254.91 Ω; that is, this should be the self impedance of the *unscaled* slot without its lens. Unfortunately, due to availability restrictions of the software, the author was unable to simulate this configuration to verify and to perfect the impedance match.

The final dimensions of the scaled slot antenna are:

$$L_S'' = \frac{L_S'}{\sqrt{5.5}} = 3.023 \text{ mm},$$
$$W_S'' = W_S' = 0.420 \text{ mm and}$$
$$L_o' = 0.481 \text{ mm}.$$

Note that the width of the antenna was not scaled, and may prove to be a source of error.

6.2 Lens Design and Test Jig Design

6.2.1 Lens Design

An empirical study of the performance of the single-slot fed substrate lens antenna versus the lens' size is desired. Ideally, the lens material must be low-loss, readily machined, and matched to the dielectric constant of the substrate. For this reason, *C-Stock AK-10.0**, a plastic stock material manufactured by Cuming Corporation[1], has been chosen as the lens material. This hard, high-density material has a dielectric constant of 10, which closely matches the substrate permittivity of 9.8 . Specifications indicate that the permittivity is almost isotropic, varying within ±5% of nominal at all points. Further, the loss tangent is rated at less than 0.002 from 2.0 to 18.0 GHz. C-Stock is readily machined with carbide tools or by grinding.

Due to time limitations, no attempt was made to find a suitable matching cap layer [12] for the lenses. Since Section 5.6 proved that the resulting reflection loss would be close to 3 dB for elliptical lenses, hyperhemispherical lenses have been chosen to be manufactured in order to limit the reflection loss to approximately 1 dB. Reflection within the lens can cause the experimental radiation patterns and impedances to differ from the simulated ones. As a result, although the pattern gain of the hyperhemispherical lens is slightly less than that of the elliptical lens, the former's radiation pattern and impedance are more likely to conform to the simulations.

The lens radii that have been chosen to be manufactured are listed in Table 10, along with their corresponding R_{lens}/n hyperhemispherical extension lengths. The extensions are cylindrical sections

---

* C-Stock AK is similar to Stycast [25,27], which was manufactured by Emerson and Cuming.

[1] Cuming Corporation, 230 Bodwell Street, Avon, MA 02322, USA. (800) 432-6464.

that are made from the same material and have the same radii as the hemispherical sections of the lenses. They are bonded to the hemispheres by applying a silicone adhesive.

Lens Radius R_{lens} [λ_0]	Lens Radius R_{lens} [mm]	Extension L_E [mm]
3	90	28.46
1	30	9.49
0.75	22.5	7.12
0.5	15	4.74
0.333	10	3.16
0.25	7.5	2.37

Table 10: Hyperhemispherical Lens Specifications at 10 GHz

It has been decided that the smallest lens' extension should be empirically varied from approximately the hyperhemispherical position to well past the elliptical position in order to verify if such an electrically small lens would still show a pattern gain improvement. As calculated in Section 2.2, the elliptical extension is $L_E/R_{lens} = 0.4290$ for a permittivity of 10, yielding $L_E = 3.22$ mm. The extension lengths of the 7.5 mm radius lens are listed in Table 11. Only the extensions corresponding to the hyperhemispherical position were manufactured for the other lenses.

L_E [mm]:	2.3	2.5	2.7	2.9	3.1	3.3	3.5	3.7	3.8

Table 11: Empirical Extension Lengths for the 7.5 mm Radius Lens

Although it has been shown in Section 4.4 that the hybrid analysis must restrict itself to lens radii that are greater than $1.0\lambda_0$ for the single slot feed, smaller lenses will be tested empirically to verify if their performance is still acceptable. After all, the restriction imposed on the simulator does not necessarily apply to the physical lenses. The manufactured lenses are depicted in Figure 65.

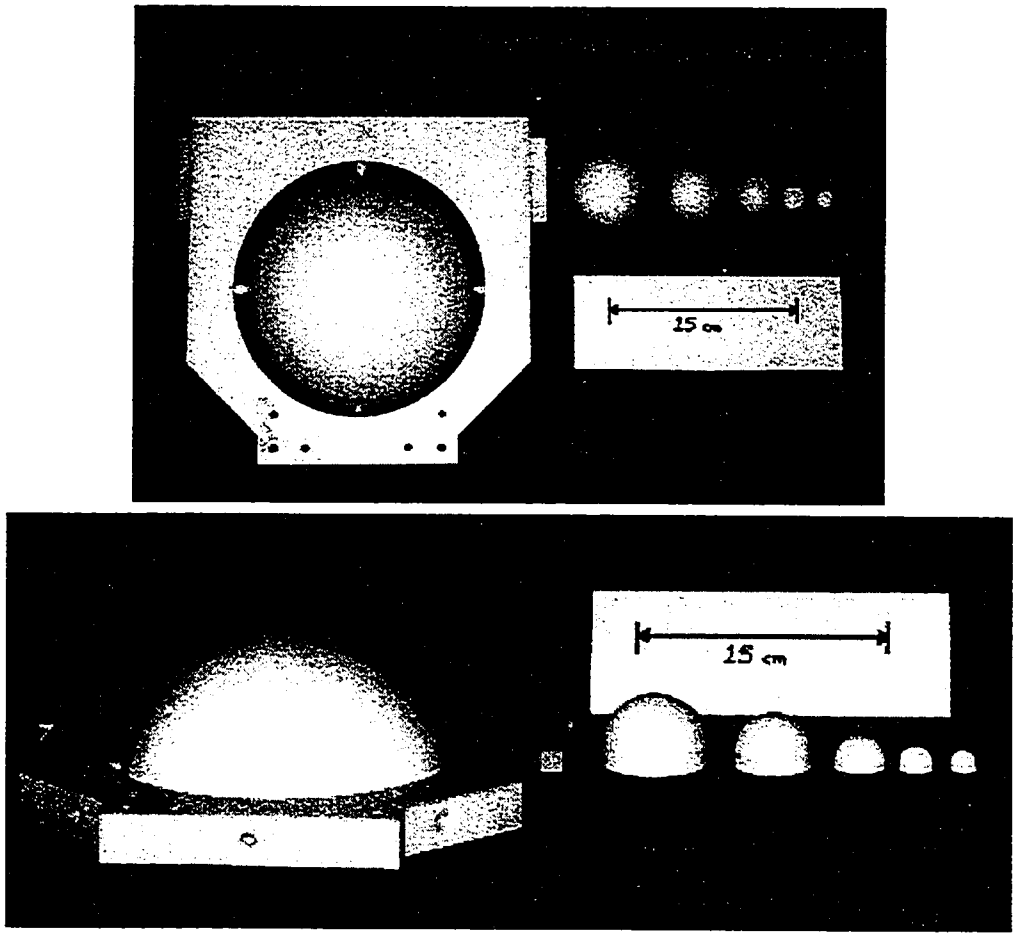

Figure 65: Photographs of the Manufactured Lenses

6.2.2 Test Jig Design

To perform radiation pattern measurements, the lenses must be mounted onto the substrate and tilted by 90 degrees so that the main beam is directed horizontally. Although the substrate can easily support the weight of the smaller lenses, the larger lenses pose a problem. Due to the high density of C-Stock, the 90 mm radius lens and cylinder weigh approximately 4 kg! The 15 mil thick Rogers 10i substrate is far too thin and brittle to support the larger lenses. For this reason, separate substrate and lens supports (test jigs) were designed. Photos of the experimental assembly are provided in Figure 66.

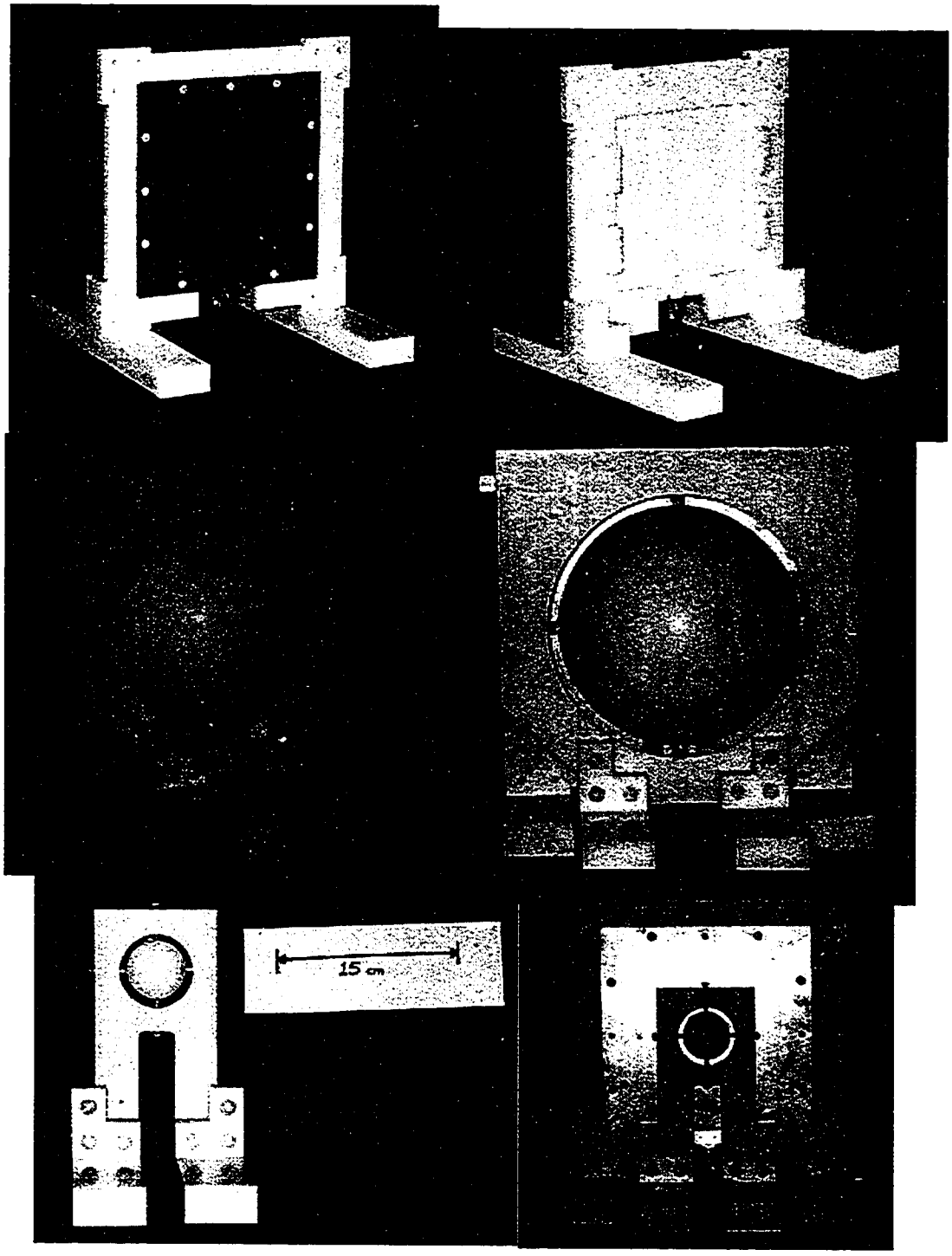

Figure 66: Photographs of the Experimental Antenna Substrate and Lens Assemblies

The upper two photos show the front (ground plane side) and back (substrate side) profiles of the substrate secured to its mount. The mount is expected to cause some blockage on the substrate side at grazing angles. The remaining photos show the 90 mm and 22.5 mm radii lenses in their holders and placed upon the slot antenna. The test jigs were manufactured from 1/2- and 1-inch thick nylon plastic (ε_r = 2.8). The radiation pattern perturbation effects of the jig will be analysed in a subsequent section by placing the nylon supports, without their lenses, in front of the free-space slot test antenna. It is anticipated that the supports will cause blockage and diffraction effects in the measured radiation patterns.

6.3 Free-Space Slot Measurements

Upon placement of a coaxial-to-microstrip connector, an impedance measurement of the free-space slot defined in Table 8 was taken on a Hewlett-Packard 8510B Vector Network Analyser at the University of Ottawa. The data are represented from 9.5 to 10.5 GHz on the log-magnitude graph and Smith Chart in Figure 67(a) and (b), respectively.

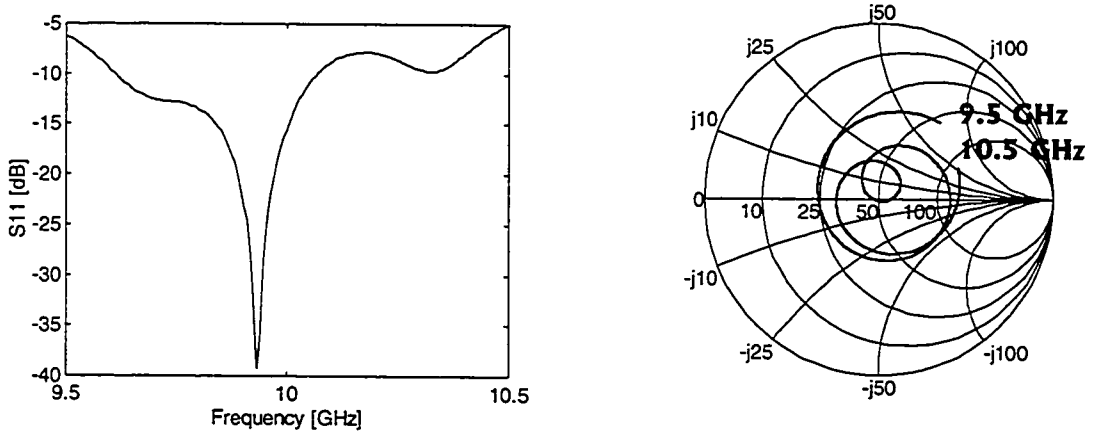

Figure 67: Measured Free-Space Slot Input Impedance

The best match of -39.3 dB is achieved at 9.935 GHz, quite close to the Ensemble 4.1 simulation. Note that the measured data are not compared to the Ensemble simulated data because the latter does not consider the perturbation that is caused by the addition of the coaxial-to-microstrip

connector. The co- and cross-polarisation radiation patterns for this slot, measured at the University of Ottawa's anechoic chamber, are shown in Figure 68 and Figure 69 for both principal planes. The magnitudes are normalised to the maximum co-polarised H-plane level.

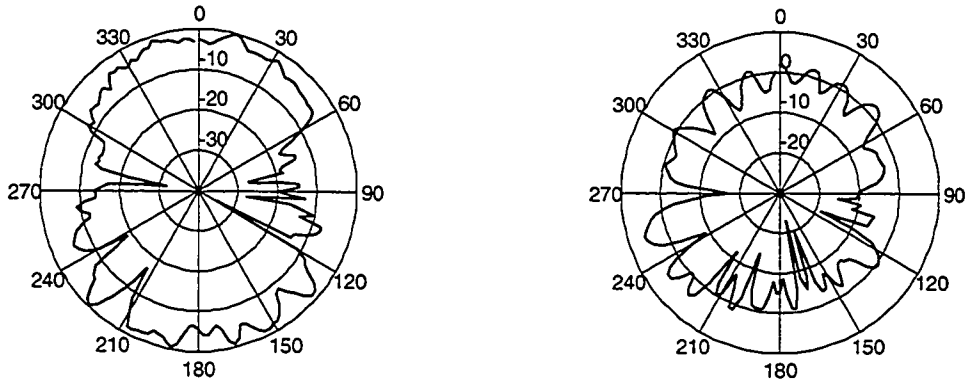

Figure 68: Co-polarised Free-Space Slot Radiation Patterns

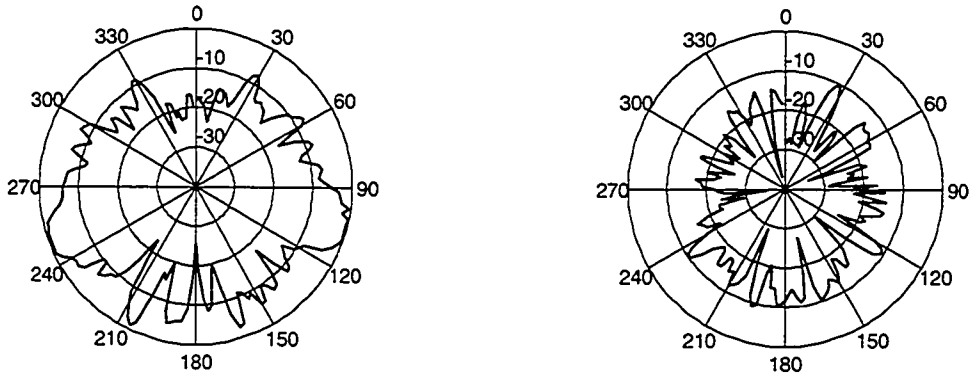

Figure 69: Cross-polarised Free-Space Slot Radiation Patterns

The top parts of the graphs (270° → 0° and 0° → 90°) represent the slot's radiation directly into space (front), while the bottom parts represent the radiation through the substrate (back). As expected, the H-plane co-polarisation has nulls at 90° and 270° and the radiation is bi-directional. The front-side 5 dB ripples are due to the finite ground plane, while the more severe back-side ripples are believed to be caused by the combination of the finite ground plane and diffraction around the rectangular frame that holds the substrate in place. The E-plane co-polarisation displays

a more uniform distribution. The pattern ripples are again attributed to the finite ground plane and back-side diffraction. The pattern minima located near ±90° are attributed to blockage from the test jig. The measured cross-polarisations are somewhat higher than expected for a slot, especially in the H-plane. These H-plane cross-polarisation maxima correspond to the angles at which the slot is blocked by the substrate's test jig.

6.4 Radiation Pattern Perturbation of the Lens Holders

The effects of the nylon lens holders on the free-space radiation patterns are now presented. By placing the large lens holder (without the lens) in front of the free-space slot antenna, its pattern perturbation effects are determined. These are shown in Figure 70.

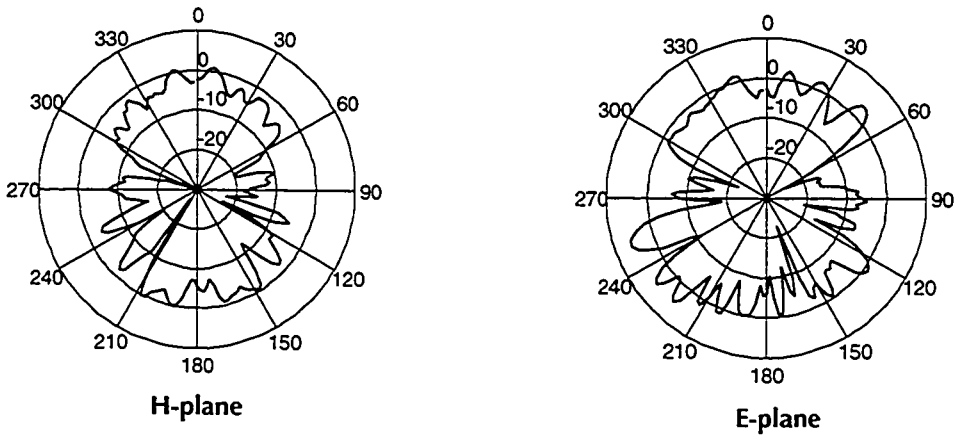

Figure 70: Large Lens Holder Perturbation Effects

The large lens holder's size is approximately the same as that of the substrate and its 7"-diameter aperture is centered on the substrate's slot. Figure 70 indicates that the large holder causes radiation blockage at angles between 270° to 300° and 60° to 90°. The slight increase in ripple in both planes located near the front side boresight (0°) are possibly due to diffraction through the circular aperture.

The large lens holder is used in conjunction with the 90 mm radius lens only. The 30 mm and the 22.5 mm radius lenses are supported by the small lens holder, shown in Figure 66. The perturbation effects of the small holder on the free-space radiation patterns are shown in Figure 71.

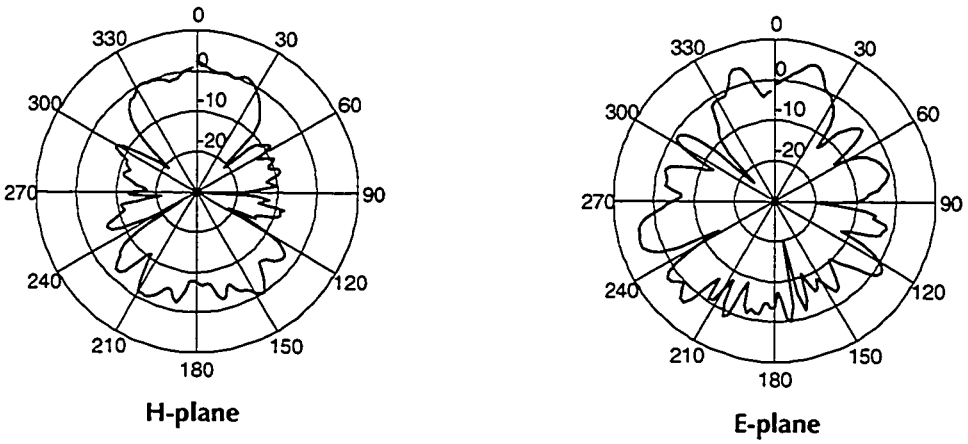

Figure 71: Small Lens Holder Perturbation Effects

The dominant perturbation effect of the small lens holder appears to be blockage between approximately 300° to 310° and 50° to 60°.

6.5 Substrate Lens Antenna Measurements

After loading the scaled slot antenna with the 90 mm radius hyperhemispherical lens, very little change in its input impedance was observed compared to its unloaded (free-space) impedance. Since this scaled slot is too short to radiate in free-space, its free-space impedance is expected to be negligible, i.e. $Z_S = 0$, resulting in an input impedance equal to that of an open-circuited microstrip transmission line. However, loading it with the largest lens should have resulted in a matched input impedance. The measured input impedance of the scaled slot antenna in free-space is compared to the measured input impedance when the slot is short-circuited in Figure 72, confirming the fact that this slot has a negligible impedance.

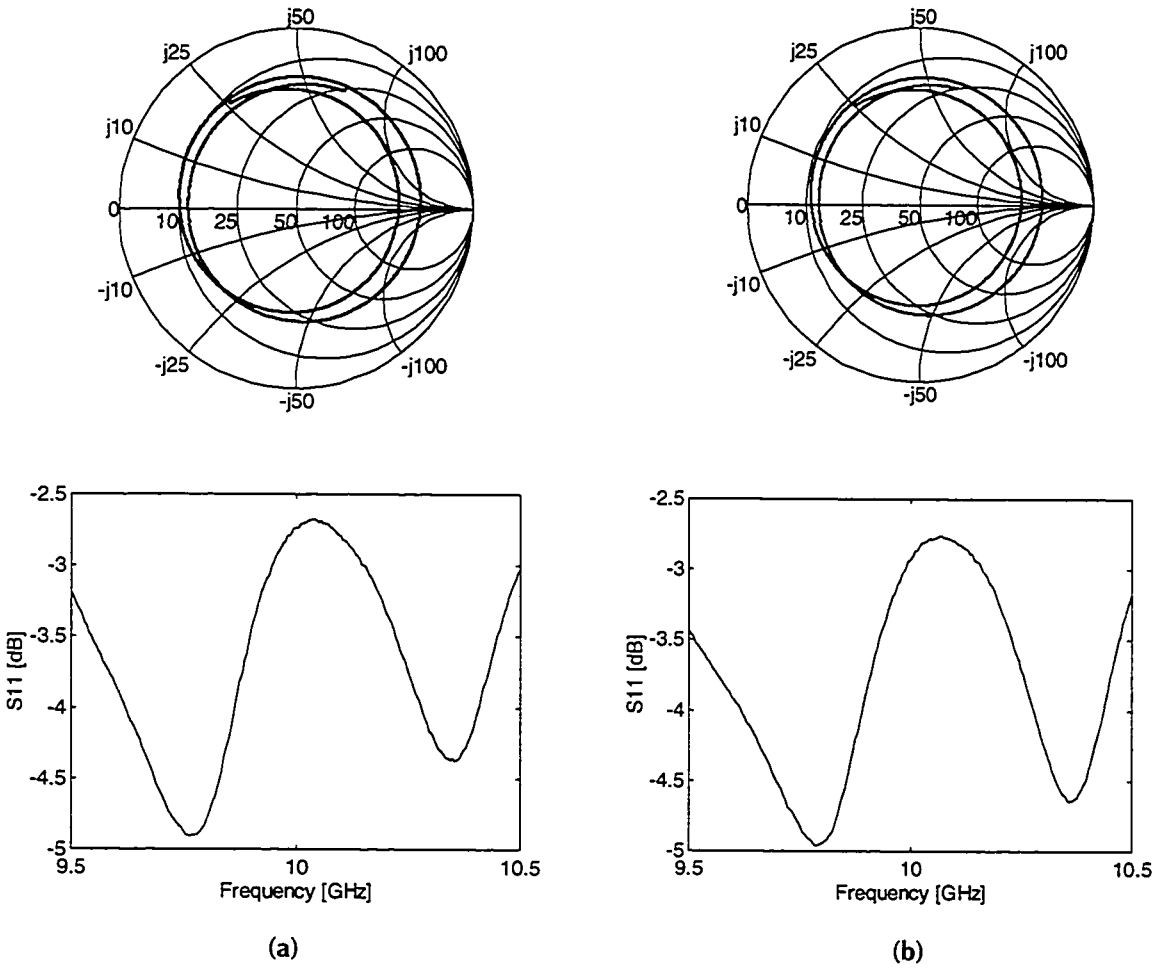

Figure 72: (a) Measured Scaled Slot Free-Space Impedance and (b) Short-Circuited Impedance

It has been also noted that the scaled slot does not radiate significantly, regardless if it is, or is not, loaded with a lens. The conclusion that is drawn from these observations is that the simple impedance scaling factor, which was described in detail in Section 6.1.2, does not seem to apply to the geometry at hand. To verify the lens' effects on the impedance, the free-space slot's self-impedance has been de-embedded with and without the lens. The details concerning this procedure are now examined.

6.5.1 Self-Impedance De-embedding of the Free-Space Slot (Reverse Modeling)

The input impedance that is experimentally measured using the network analyser does not correspond the slot's self-impedance that was calculated using Ensemble 4.1 . The self-impedance is embedded within the measurement, for the launch assembly perturbs and adds itself to the experimental measurement. Since the slot and the open-circuited stub can be regarded as a series connection, their impedances are lumped together. The measured input impedance is therefore regarded as being that of a cascaded two-port (representing the launch assembly) and one-port network (representing the slot and the stub), as illustrated in Figure 73.

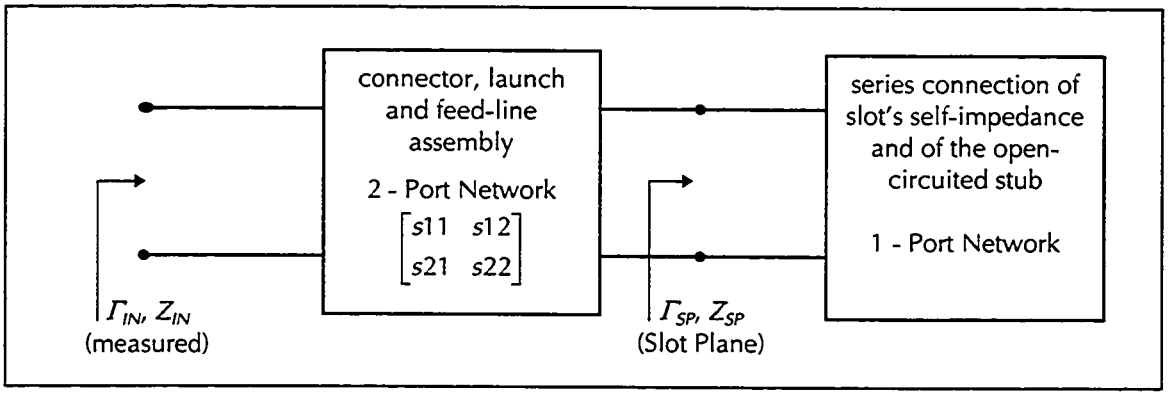

Figure 73: Measured Input Impedance Schematic

By isolating the scattering parameters of the 2-port network, the impedance reference plane can be shifted to the slot plane by using the following expression, which has been developed at length in Appendix D:

$$\Gamma_{SP} = \frac{\Gamma_{IN} - s_{11}}{s_{12}s_{21} + s_{22}\Gamma_{IN} - s_{11}s_{22}}. \qquad (6\text{-}6)$$

The 2-port network's scattering parameters are determined by first measuring the input impedance of the *shorted* free-space slot. Libra is then used to match this response to that of a reverse-modeled network that is composed of discrete elements. Once a satisfactory match to the shorted slot network is obtained, the length of the open-circuited stub is subtracted from the model and its two-port response is simulated, yielding the four required scattering parameters. An impedance

measurement with the slot *not* shorted is then taken and its impedance is de-embedded. The results of the de-embedding are shown in Figure 74.

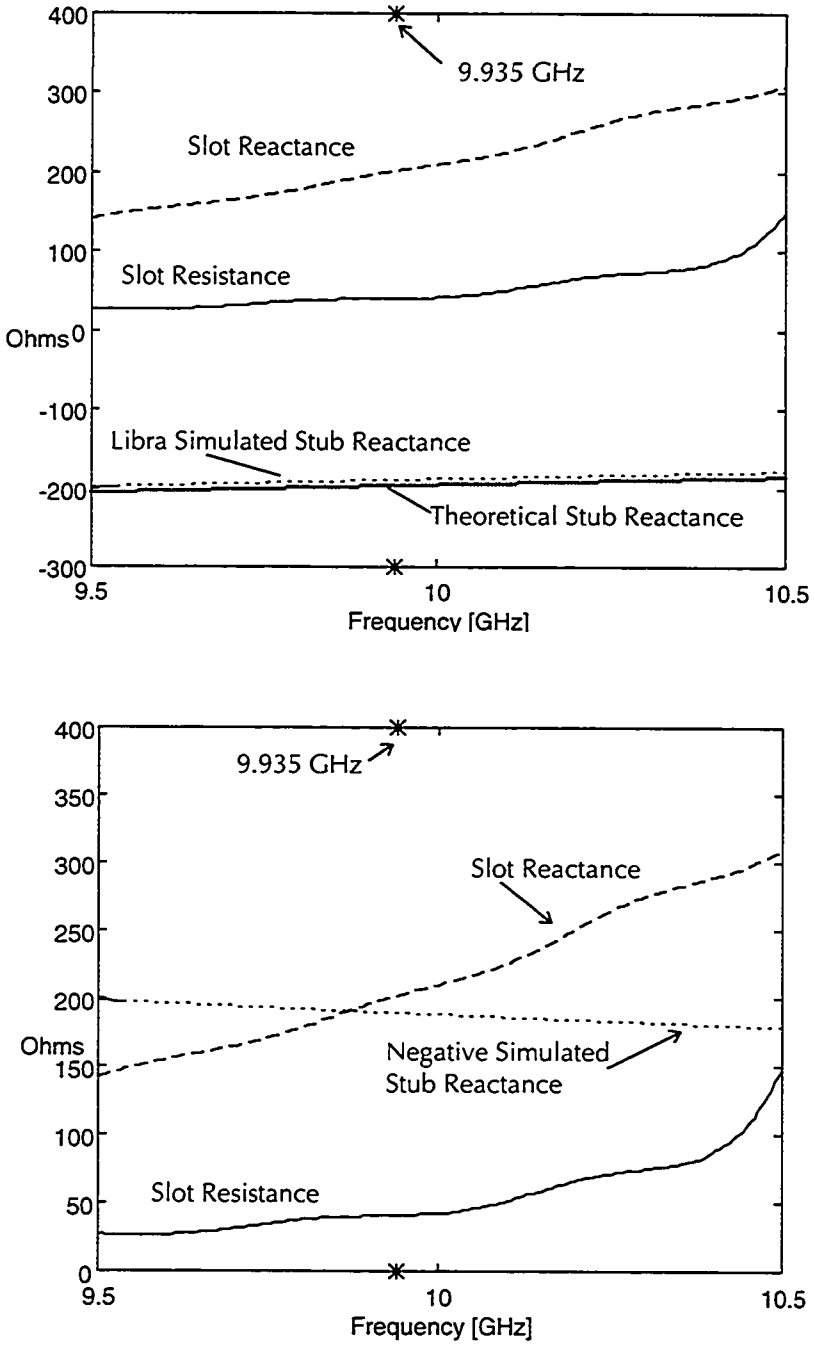

Figure 74: De-embedded Impedance of the Free-Space Slot

The upper graph indicates the de-embedded slot impedance, and the theoretical and simulated reactances of the open-circuited stub. The latter two curves are in close agreement. (Note that a capacitive length extension of 118 μm has been added to the physical length of the stub for the theoretical reactance calculation [83]). The asterisks on the horizontal axes indicate the frequency of 9.935 GHz, at which the minimum return loss was observed in Figure 67. The lower graph shows the negative simulated stub reactance superimposed on the de-embedded slot impedance, indicating that the stub reactance is very close to tuning out the slot's reactance. At 9.935 GHz, the impedances are the following:

- Slot Resistance: 40.62 Ω
- Slot Reactance: 201.17 Ω
- Theoretical Stub Reactance Including the Extension: -196.6 Ω
- Simulated Stub Reactance: -189.3 Ω.

The series connection of the slot and of the stub yields an impedance of:

$$Z_{SLOT} + Z_{STUB} = 40.62 + j11.87\ [\Omega],$$

which is reasonably close to the impedance of 44.6 - j23.6 Ω that was predicted at 9.9 GHz by Ensemble 4.1 . No simulated data is available at exactly 9.935 GHz.

This procedure has been repeated over a wider frequency band in order to observe the frequency shift that the loading of the lens produces. Reverse-modeling is very difficult and time-consuming when the frequency band is larger than approximately 1 GHz. Because of this, the frequency range was subdivided into smaller bands. Future work should investigate using a more rigorous de-embedding method, such as the TRL method. The results are displayed in Figure 75.

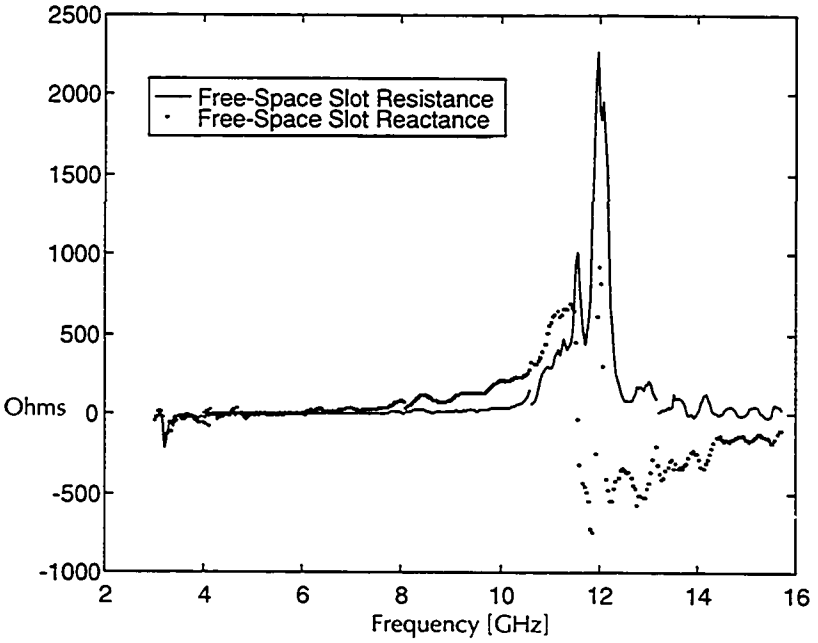

(a)

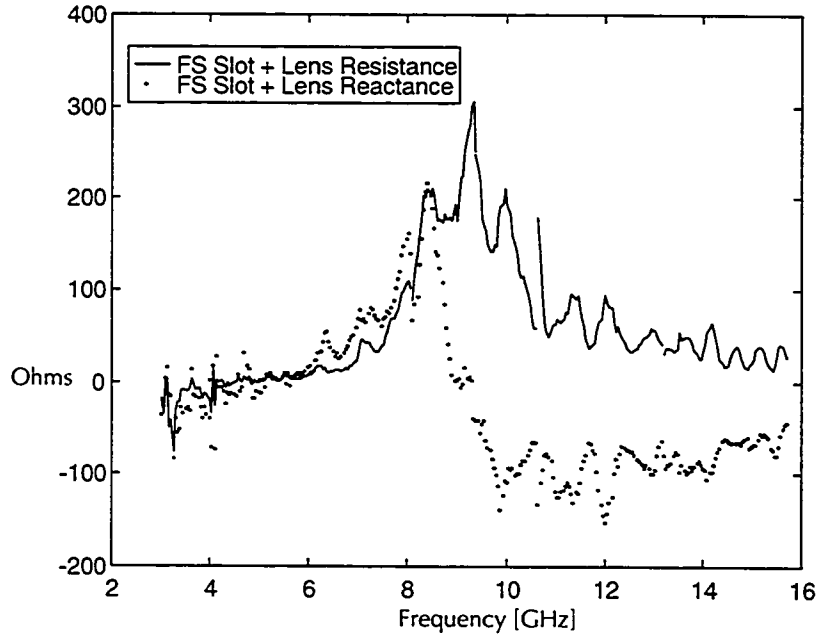

(b)

Figure 75: Wide-Band De-embedding of the Free-Space Slot

(a) With and (b) Without the 90 mm Radius Lens

The upper graph displays the free-space slot's de-embedded impedance, while the lower displays the de-embedded impedance when the 90 mm radius hyperhemispherical lens is applied to the free-space slot. Indeed, the limitations of the reverse-modeling technique are quite evident in these plots, appearing as noise errors and band-transition discontinuities. Nevertheless, the general impedance curves are clearly recognizable. A shift in the resonant frequency is evident, and a scaling factor of approximately 0.7 exists when the lens is added to the free-space slot. This does not correspond to the anticipated shift of $\frac{1}{\sqrt{\varepsilon_m}} = 0.426$. The scaled slot is therefore too short, confirming the cause of its negligible self-impedance. Judging by the peaks in the slot reactance, the self-impedance magnitude appears to be scaled by between 200/700 = 0.29 and -100/-500 = 0.2: which is smaller than the anticipated impedance scaling of 0.426. The slot's resistance is judged to be too choppy to offer an accurate scaling factor. These observations will be analysed in Chapter 7.

Due to the difficulty and time required to de-embed the slot impedance, it has not been done for other lens combinations.

6.5.2 Slot Lens Antenna Radiation Patterns

Since the scaled slot does not radiate, the experimental radiation patterns have been taken by applying the lenses to the free-space slot. It is understood that an impedance match is therefore not achieved. Furthermore, because of the impedance frequency shift factor of 0.7, this slot will appear to be too long electrically to produce a single-lobed radiation pattern. For this reason, the frequency was reduced to 6 GHz. In doing so, the lenses are now all electrically smaller than the 10 GHz simulations, and have been re-simulated at 6 GHz for comparison with the experimental data. The radiation patterns were measured in the University of Ottawa's anechoic chamber. Unfortunately, two lens extension mistakes were made during the manufacturing stage. The extension of the

22.5 mm radius lens is 7.75 mm long instead of 7.115 mm long and is therefore between the hyperhemispherical (7.115 mm) and the elliptical position (9.65 mm). The extension of the 15 mm radius lens is 3.175 mm long instead of 4.74 mm long and is therefore shorter than the hyperhemispherical position. The simulations have been altered to reflect these changes. The measured and simulated 6 GHz radiation patterns of the 90 mm ($5.69\lambda_d$ and $1.8\lambda_0$ @ 6 GHz) radius hyperhemispherical SLA are plotted in Figure 76. The E-plane scan is on the left, while the H-plane is on the right. The measured data are represented by the thicker of the two lines. Since this largest lens possesses the highest gain, all subsequent measurements have been normalised to its maximum level. Since absolute gain levels cannot be predicted by the simulator, the simulated pattern levels have been manually shifted to the measured pattern levels so that both will always coincide at boresight. Note that a thin layer of silicone grease was applied experimentally to fill the air gap between the slot antenna and the lenses.

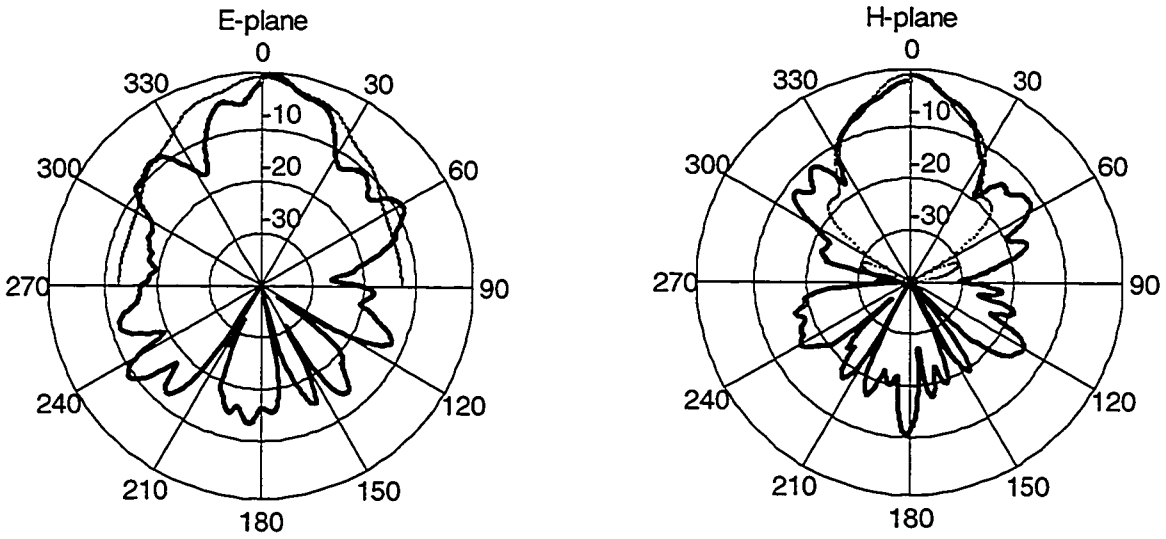

Figure 76: E- and H-plane Radiation Patterns, 90 mm Radius Hyperhemispherical SLA (Thick Line: Measured Data, Thin Line: Simulated Data)

Referring to Figure 76, the measured E-plane pattern displays a more complicated lobe structure than the simulated one. The H-plane pattern is more accurately predicted up to approximately ±40°; beyond this angle, the measured sidelobe levels exceed the simulated ones. The discrepancy

may be attributed to the lens holder, which has been shown to perturb the free-space antenna's pattern beyond ±60°. The front-to-back (F/B) ratio is slightly less than the F/B ratio of $\varepsilon_r^{3/2}$ = 15 dB that was predicted in Section 2.1 .

The patterns of the 30 mm ($1.90\lambda_d$, $0.6\lambda_0$) radius hyperhemispherical SLA are depicted in Figure 77. The patterns are in better agreement, but the F/B ratio in the E-plane is only approximately 10 dB.

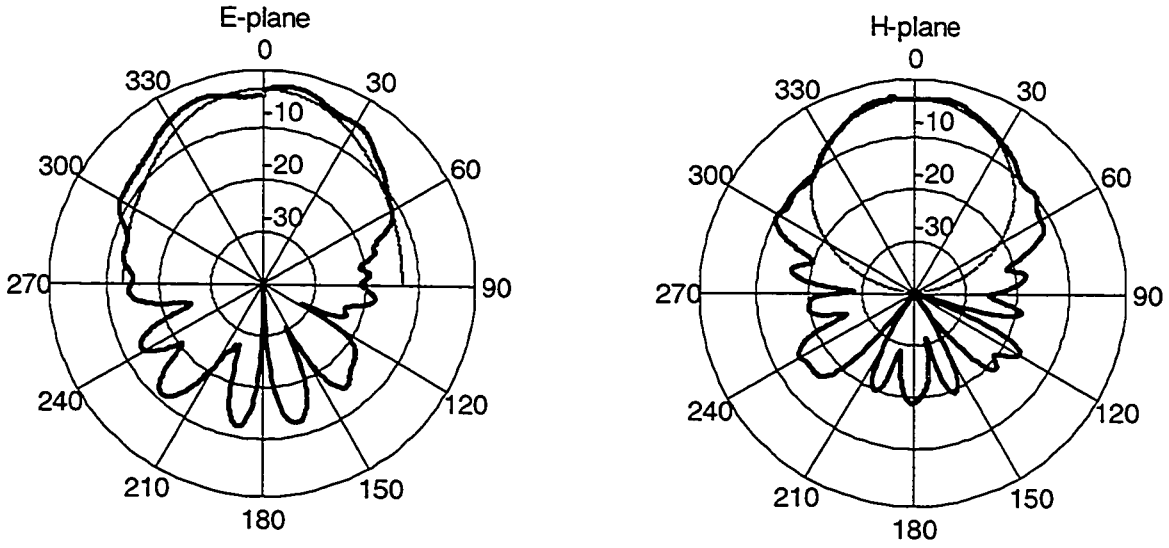

Figure 77: E- and H-plane Radiation Patterns, 30 mm Radius Hyperhemispherical SLA (Thick Line: Measured Data, Thin Line: Simulated Data)

The patterns of the 22.5 mm ($1.42\lambda_d$, $0.45\lambda_0$) radius, 7.75 mm extension length SLA are plotted in Figure 78. Although the H-plane pattern is in excellent agreement, the measured E-plane pattern again appears to be overly directive.

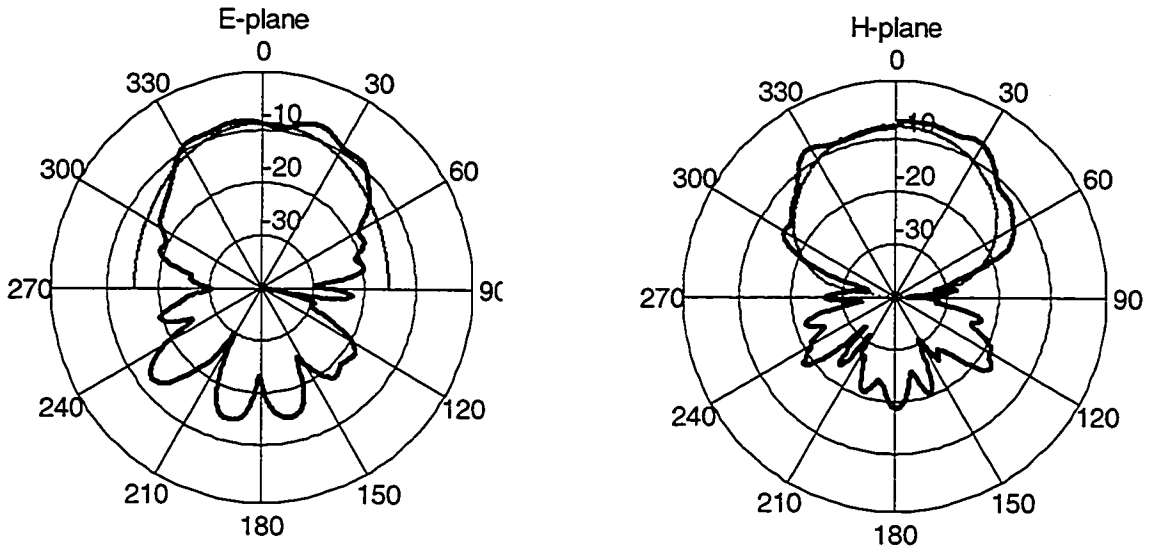

Figure 78: E- and H-plane Radiation Patterns, 22.5 mm Radius Lens, 7.75 mm Extension (Thick Line: Measured Data, Thin Line: Simulated Data)

The six preceding measurements have all had a lens holder positioned in front of the substrate. The three H-plane patterns have generally been more accurately predicted than the three E-plane patterns. This could be attributed to the theoretical E-plane pattern being more broad than the H-plane pattern. Because of this, more power is impinging upon the lens holders in the E-plane, possibly causing a more severe perturbation effect (reflection, diffraction and refraction). No lens holders are used in the measurements that follow. The remaining lenses are small enough to be temporarily bonded to the substrate using silicone grease.

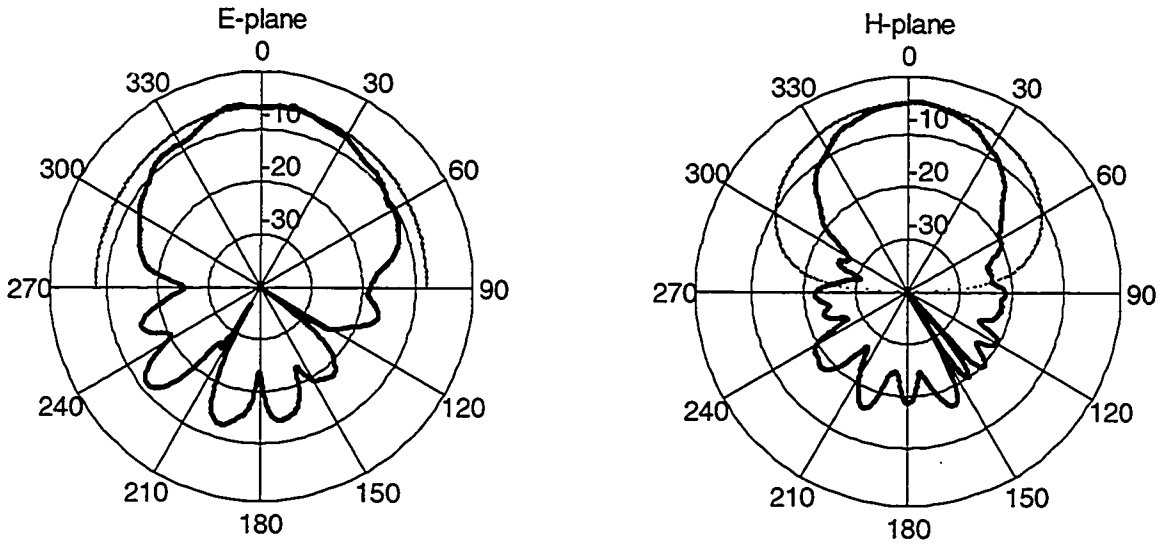

Figure 79: E- and H-plane Radiation Patterns, 15 mm Radius Lens, 3.175 mm Extension (Thick Line: Measured Data, Thin Line: Simulated Data)

The patterns of the 15 mm ($0.95\lambda_d$, $0.30\lambda_0$) radius, sub-hyperhemispherical 3.175 mm extension SLA are plotted in Figure 79. Surprisingly, even though the lens extension of 3.175 mm is far less than the hyperhemispherical position of 4.74 mm, this SLA displays significant pattern gain in the H-plane and moderately superior pattern gain in the E-plane. The measurements have been repeated for this lens and they confirm the results. The reason for the superior directivity of this particular lens has not been determined. The results are contrary to theory, which states that the directivity should decrease if the extension length is decreased.

The patterns of the 10 mm ($0.63\lambda_d$, $0.2\lambda_0$) radius hyperhemispherical SLA are displayed in Figure 80. The marginally asymmetric E-plane pattern is caused by the lens being positioned slightly off-axis.

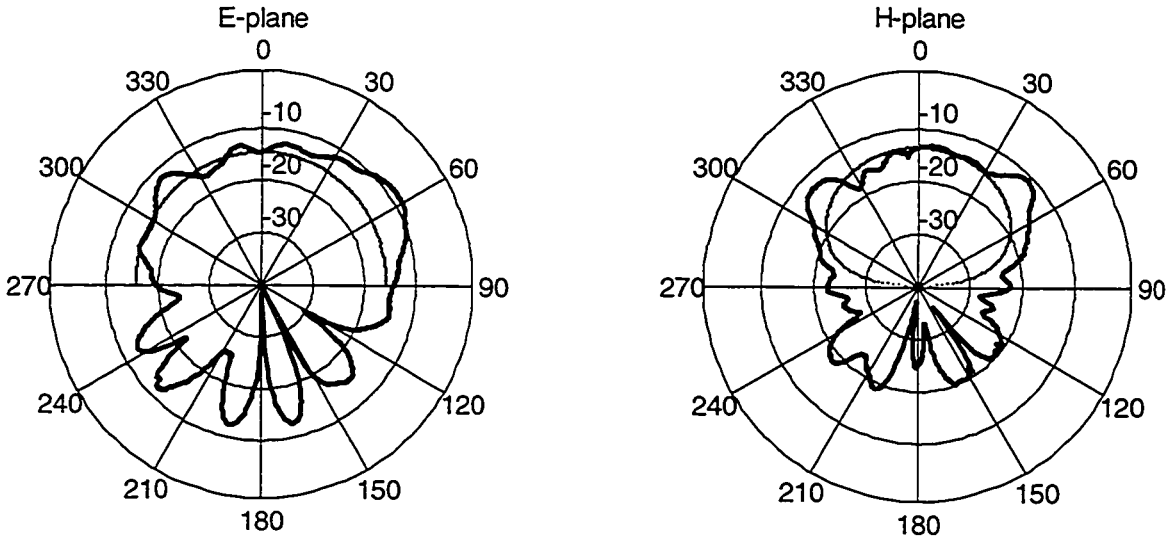

Figure 80: E- and H-plane Radiation Patterns, 10 mm Radius Hyperhemispherical SLA (Thick Line: Measured Data, Thin Line: Simulated Data)

The H-plane displays secondary lobes near ±45° that were not predicted. These lobes are also observed in the measurements that follow. These secondary lobes are similar to higher order patterns that have been observed in hemispherical DRAs [49]. It is thought that these secondary lobes could be predicted if subsequent ray tracing of internal reflections was pursued in the simulator, as explained in Section 5.6 .

The radiation pattern of the 7.5 mm ($0.47\lambda_d$, $0.15\lambda_0$) radius SLA are depicted in Figures 87 through 90 for extensions of: 3.8, 3.3, 2.9, and 2.3 mm. It is clear that the extensions do not affect the gain of the SLA, confirming the prediction of Section 5.5 .

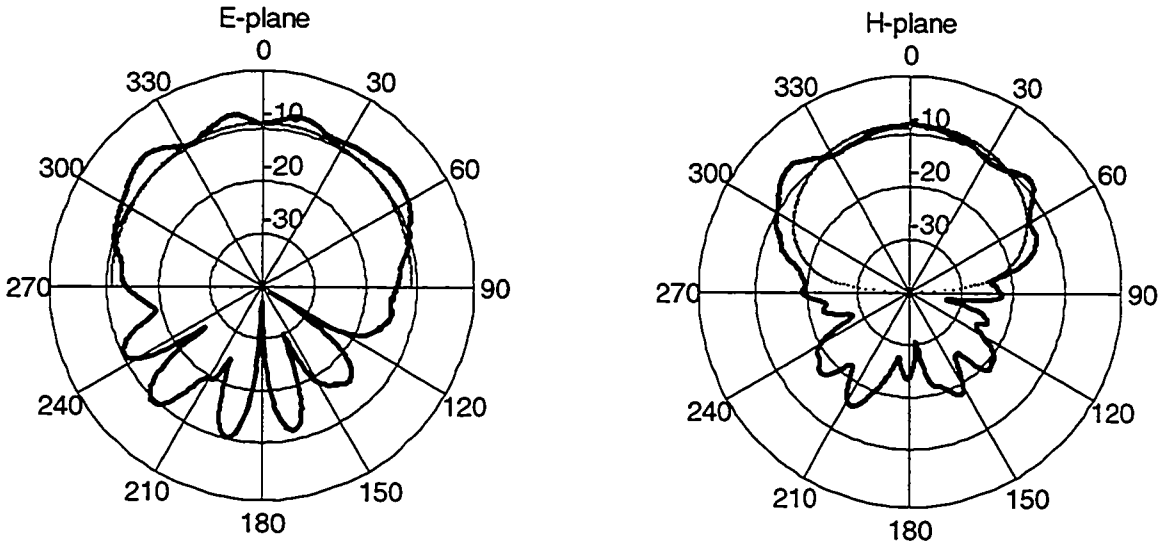

Figure 81: E- and H-plane Radiation Patterns, 7.5 mm Radius SLA, 3.8 mm Extension
(Thick Line: Measured Data, Thin Line: Simulated Data)

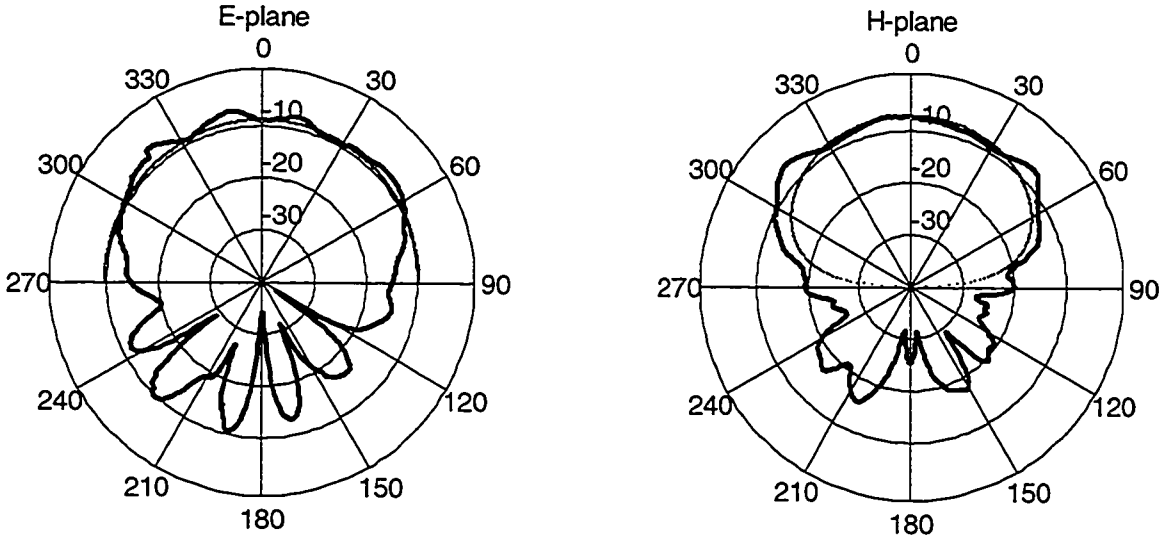

Figure 82: E- and H-plane Radiation Patterns, 7.5 mm Radius SLA, 3.3 mm Extension
(Thick Line: Measured Data, Thin Line: Simulated Data)

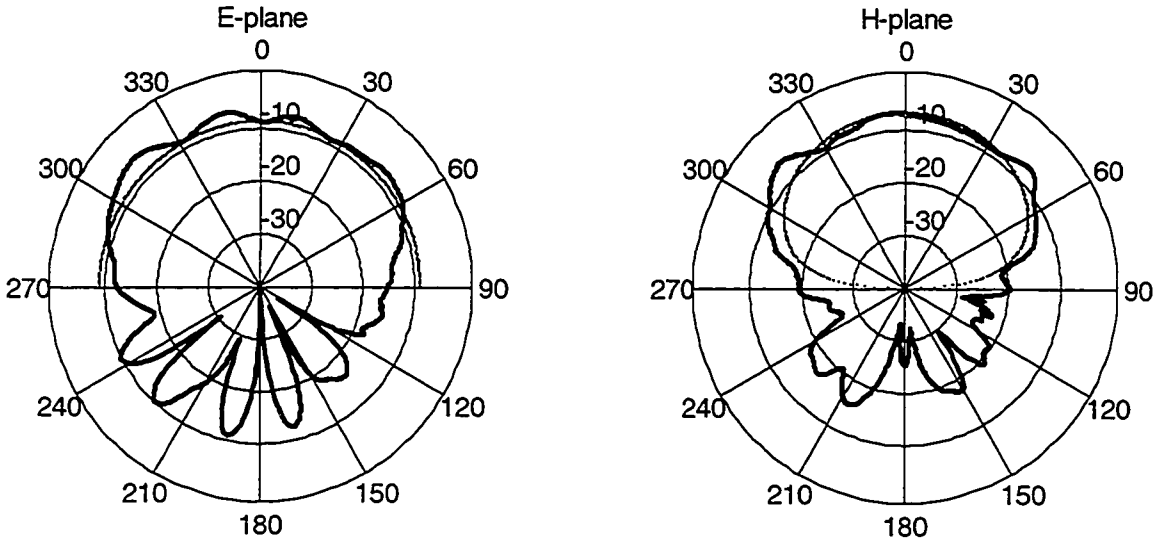

Figure 83: E- and H-plane Radiation Patterns, 7.5 mm Radius SLA, 2.9 mm Extension
(Thick Line: Measured Data, Thin Line: Simulated Data)

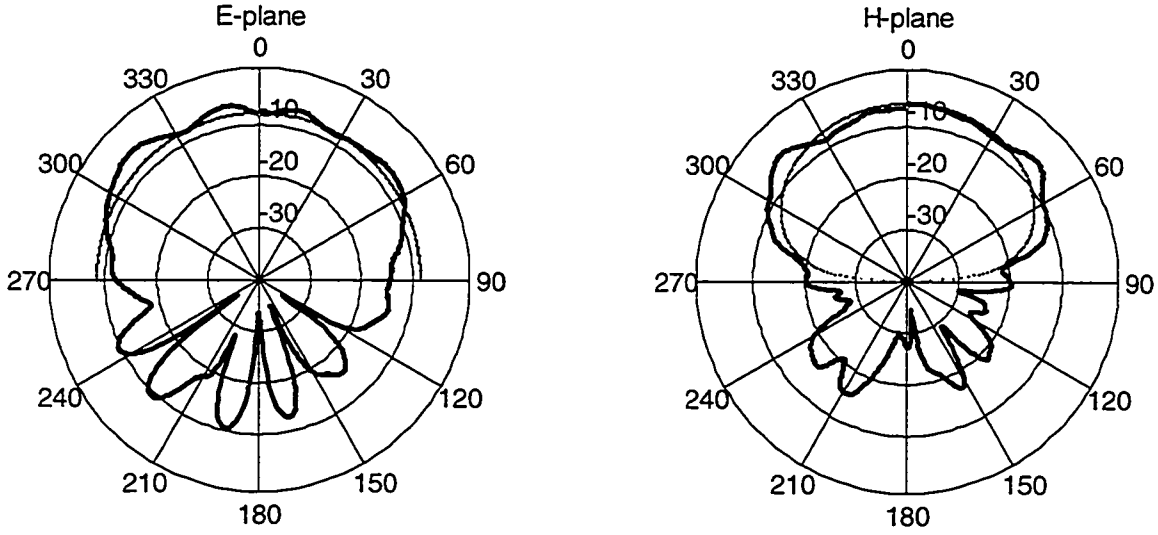

Figure 84: E- and H-plane Radiation Patterns, 7.5 mm Radius SLA, 2.3 mm Extension
(Thick Line: Measured Data, Thin Line: Simulated Data)

The measured cross-polarisation patterns of the largest (90 mm radius) hyperhemispherical lens have also been included in Figure 85. They show a significant improvement over the free-space slot's cross-polarisation patterns that were given in Figure 69.

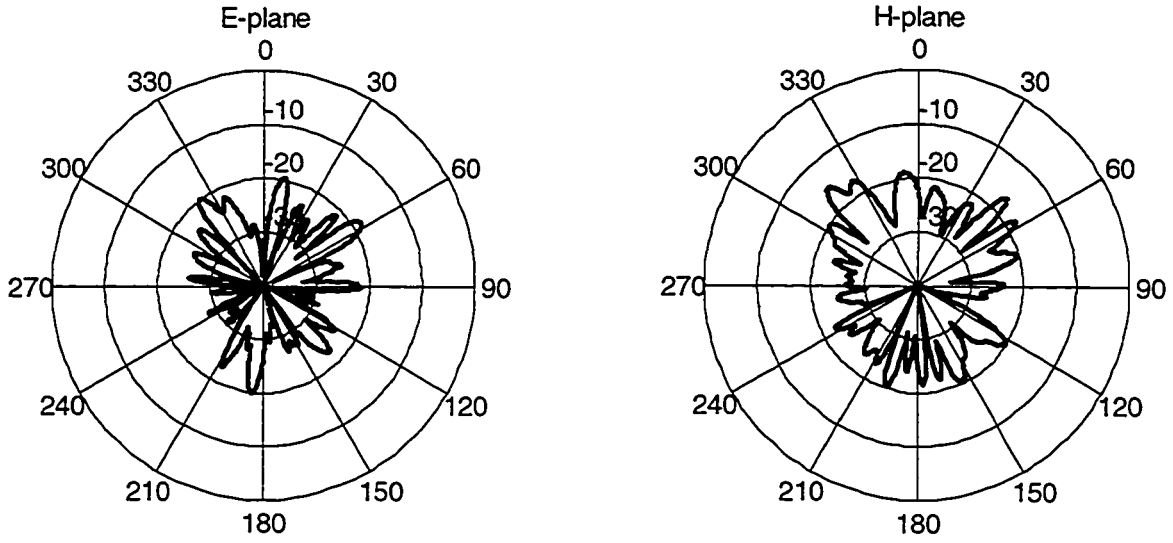

Figure 85: E- and H-plane Measured Cross-Polarisation Radiation Patterns, 90 mm Radius Hyperhemispherical SLA

6.6 SLA Measurements Conclusion

6.6.1 Impedance

In Section 6.1.2, the scaled slot (for use with the lenses) was designed using the closed form $\frac{1}{\sqrt{\varepsilon_m}}$ scaling factor for dielectric half spaces. However, the results of Section 6.5.1 indicated that this slot was very poorly matched: it appeared to be a short circuit. By placing the largest lens on the free-space slot, de-embedding indicated that this loaded free-space slot's impedance levels dropped by a factor of approximately 0.2 to 0.29 instead of dropping by a factor of 0.426 . Further, the anticipated resonant frequency shift of 0.426 was only 0.7 . Hence, the scaled slot was indeed too short electrically to be used as an antenna. The conclusion is that the substrate lens does not seem to mimic a dielectric half space. Many possible causes exist, including: internal reflections within the lens, the microstrip coupling mechanism, and the thin substrate on the other side of the slot.

More work is required to fully characterise the SLA impedance as the simple scaling equations clearly do not apply.

6.6.2 Front to Back Ratios (F/B)

Table 12 indicates the approximate F/B ratios that were observed in the measured radiation patterns of the SLAs (E- and H-plane only). Note that these are only approximations, for the substrate support jig was shown to interfere with the back-side measurement of the radiation patterns.

Lens Radius [mm]	Lens Radius [λ at 6 GHz]	F/B Ratio (approx.)
90	$1.8\lambda_0$, $5.69\lambda_d$	10 dB
30	$0.6\lambda_0$, $1.9\lambda_d$	10 dB
22.5	$0.45\lambda_0$, $1.42\lambda_d$	5 dB
15	$0.3\lambda_0$, $0.95\lambda_d$	5 dB
10	$0.2\lambda_0$, $0.63\lambda_d$	0 dB
7.5	$0.15\lambda_0$, $0.47\lambda_d$	0 dB

Table 12: Approximate F/B Ratios of the Measured SLAs

According to the theory pertaining to slot antennas on dielectric half-spaces, a F/B ratio of $\varepsilon_r^{3/2} = 15$ dB should be observed. Although the F/B ratio of the largest lens is close to this level, the ratio is seen to decrease as the lens size decreases and it is approximately nil for the smallest lenses. The conclusion that is drawn from these observations is that the SLAs that are smaller than approximately $0.3\lambda_0$ at 6 GHz do not provide significant improvement to the free-space slot's F/B ratio (of 0 dB).

6.6.3 Pattern Directivity

Assuming that the test jig perturbation effects did indeed interfere with the radiation pattern measurements, these measurements appear to conform to the predictions of the hybrid PO simulator, especially near boresight. The major exception is the 15 mm radius, 3.175 mm extension length SLA, which despite its sub-hyperhemispherical extension length, displayed a highly directive

pattern. Hence, the directivity graphs that were calculated in Section 5.5 for the front-side of the SLA are validated. It is interesting to note that the measured patterns are very closely simulated for lens radii that are as small as $0.15\lambda_0$ ($0.47\lambda_d$) at 6 GHz, which indicates that the predicted failure of the hybrid PO method at a radius of $0.5\lambda_0$ is a conservative estimate.

The addition of the 90 mm radius hyperhemispherical lens onto the free-space slot also showed that the cross-polarisation levels of this antenna were improved from approximately -10 dB, given in Figure 69, to -20 dB Figure 85. It is also seen that the SLA radiation patterns appear to be less susceptible to the size of the ground plane, for the ripples that were observed in the free-space slot pattern in Figure 67 are much less visible in the SLA patterns.

7. Thesis Summary and Future Work

In this thesis, electrically small extended hemispherical substrate lens antennas have been investigated. A Physical Optics radiation pattern simulation technique has been developed and its predictions have been compared to actual physical measurements.

An introduction to SLA and DRA technology was presented in Chapter 2. Planar antennas were shown to be desirable for low-cost integration at high microwave frequencies and beyond. This class of antennas was shown to exhibit undesirable characteristics, including substrate mode coupling and bi-directional radiation. The use of a substrate lens was proposed as a method to circumvent these problems. Various lens geometries and their properties were explored, and a synthesis method for manufacturing elliptical lenses was given. Finally, the hemispherical DRA was shown to possess a geometry that is almost identical to that of the SLA. In compliance with the fourth thesis objective, the chapter concluded by examining the differences that exist between SLAs and DRAs, including size and analysis methods, which suggested that a gray area exists between the two radiators and warranted further investigation.

The third chapter of this thesis was devoted to the study of analysis methods for simulating electrically small SLAs. The hybrid GO technique was shown to be adequate for predicting electrically large SLA radiation; however, this method was also proven to be inadequate for electrically small SLAs. An improved lens illumination technique was suggested that would incorporate any feed antenna geometry and that would accurately predict the radiated field values at any radial distance. Propagator candidates were explored and compared, including: Fourier Optics, Spectral Domain, Physical Optics, and DRA Moment Methods. Chapter 3 concluded by justifying the selection of PO as the propagator to be used for lens illumination.

In Chapter 4, the new PO hybrid simulation technique was thoroughly examined. A rigorous derivation of the free-space Green's function, which is required for PO, was presented. The PO hybrid method was then explained in detail, partially fulfilling the third objective of this thesis, which was to develop a simulation technique capable of analysing electrically small lenses. Limitations of this technique were shown to exist, including: the effects of internal reflections at the lens-to-air interface, slot current ambiguities, wavevector direction ambiguities, and the radial field components. Two test cases were investigated, one consisting of a double slot feed that had previously been published, the other consisting of the single slot feed that was to be used as the experimental feed for this thesis. The radial fields at the lens-to-air interface were shown to be the primary limitations. Chapter 4 concluded by specifying that the radial fields for the double slot feed and the single slot feed surpass 10% of the maximum transverse field components at radii of $0.5\lambda_0$ and $1.0\lambda_0$, respectively. If the radii of the lenses are smaller than these limits, the validity of the Fresnel equations at the interface, which do not account for a radial field component, is suspect.

Analyses that were performed using the PO hybrid simulator were presented in Chapter 5. In accordance with the third objective of this thesis, determining the failure of the existing GO hybrid analysis, a double and a single slot feed were simulated using both analysis methods. The results showed that although the PO method more accurately predicts the radiation patterns from the feed elements, the GO method suffices for these two simple feed geometries. In compliance with the second objective of this thesis, the radiation patterns of slot fed SLAs were calculated for various lens radii. For the first time, the directivities of elliptical and hyperhemispherical SLAs were calculated versus the radius of the lens. The directivity enhancement of an elliptical lens over that of a hyperhemispherical lens was shown to be negligible for radii that are less than approximately $3.2\lambda_d$. Also for the first time, a reflection loss analysis was performed for lenses that have no matching cap layer. Hyperhemispherical lenses were shown to be the least susceptible to internal reflections, while elliptical lenses were shown to suffer from significantly more reflection loss. Hence a compromise exists between directivity and reflection loss for SLAs with no matching layers. The

chapter concluded with an analysis of the first reflection effect, demonstrating the intractability of such analyses for subsequent reflections.

The analytical results were compared to actual measurements in Chapter 6, which opened by detailing the design procedure. The first thesis objective, verifying the validity of the impedance and length scaling equations, was fulfilled therein. It was shown that the addition of a large lens on a microstrip coupled slot does not satisfy the equations. The observed increase in the electrical length of the slot was less than anticipated, while the impedance levels were reduced more significantly than predicted by the equations. The second thesis objective was fulfilled by empirical measurements of the radiation patterns of hyperhemispherical SLAs of various radii. The PO simulator proved to yield acceptable predictions, especially for small radii, which was unexpected. Similarities between the observed pattern lobe structure of the smallest SLAs and higher order DRA mode patterns were examined, in fulfillment of the final thesis objective.

Although the objectives of this thesis and the goal of studying electrically small SLAs have been met, much work remains to be done. The following suggestions are made for furthering the work that has been initiated in this thesis.

The cause of the discrepancies between the analytical and the observed impedance levels merits further investigation. Internal reflections may be among the possible causes, therefore a suitable quarter-wave matching cap layer for the lenses should be investigated. The most difficult aspect to this work involves manufacturing a matching cap of uniform thickness and making it conform to the extended hemispherical surface. A matching layer could also be added to the simulator. Another possible cause to the impedance discrepancy might be the feed mechanism. Microstrip coupling may prove to impact the slot's impedance and electrical length. It would be worthwhile to manufacture another set of slot feed antennas that are directly excited by a ground via through the substrate. If these options are pursued, it is imperative that an improved impedance de-embedding

technique be implemented. The reverse-modeling technique that was used in Chapter 6 was time-consuming and inadequate. A TRL method would be beneficial.

Other suggested future work includes an investigation into a more rigorous numerical method for simulating SLAs. A moment method-style of analysis would be ideal but would require the derivation of exact Green's functions and resonant modes [38] for the extended hemispherical structure. Finally, an investigation into the 15 mm radius, 3.175 mm extension lens may also be warranted. In Chapter 6, this sub-hyperhemispherical SLA displayed a more directive pattern than was predicted. This work has the lowest priority for the predicted radiation pattern may have been perturbed by either internal reflections, or by a non-sinusoidal slot current distribution.

8. Appendix A: Fourier Optics Related to the Spectral Domain Method

The far-field Fourier Optics *scalar* propagator for an aperture in the $\xi\eta$-plane is the following [61, p.74]:

$$E(x,y)=\frac{e^{jkz}e^{j\frac{k}{2z}(x^2+y^2)}}{j\lambda z}\int_{-\infty}^{\infty}\int_{-\infty}^{\infty}E_a(\xi,\eta)e^{-j\frac{2\pi}{\lambda z}(x\xi+y\eta)}d\xi d\eta\,, \tag{A-1}$$

where E_a is the scalar aperture field, k is the wavenumber, and z is the perpendicular distance from the $\xi\eta$-plane. This double-integral is used to find the fields on a plane located in front of the aperture (also perpendicular to the z axis). The symbols ξ and η are the aperture plane equivalents to x and y, respectively. The latter pair is used exclusively in the observation (far-field) plane.

A far-field derivation of the Spectral Domain Method has been developed using the method of *Stationary Phase* [57, pp.625-629]. The resulting expression for the *vectorial* far-field is:

$$\bar{E}(r,\theta,\phi)=j\frac{ke^{-jkr}}{2\pi r}\left[\hat{\theta}\left(f_x\cos\phi+f_y\sin\phi\right)+\hat{\phi}\cos\theta\left(-f_x\sin\phi+f_y\cos\phi\right)\right], \tag{A-2}$$

where f_x and f_y are the x and y components of the wave amplitude vector described in Section 3.4.2:

$$\bar{f}\left(k_x,k_y\right)=\hat{x}f_x\left(k_x,k_y\right)+\hat{y}f_y\left(k_x,k_y\right)+\hat{z}f_z\left(k_x,k_y\right). \tag{A-3}$$

The f_x and f_y components are expressed as:

$$f_x=\int_{-\infty}^{\infty}\int_{-\infty}^{\infty}E_{a\xi}(\xi,\eta)\exp\left[jk(\xi\sin\theta\cos\phi+\eta\sin\theta\sin\phi)\right]d\xi d\eta \tag{A-4}$$

$$f_y=\int_{-\infty}^{\infty}\int_{-\infty}^{\infty}E_{a\eta}(\xi,\eta)\exp\left[jk(\xi\sin\theta\cos\phi+\eta\sin\theta\sin\phi)\right]d\xi d\eta\,, \tag{A-5}$$

where $E_{a\xi}$ and $E_{a\eta}$ are the ξ and η components of the aperture field, respectively. Converting the three preceding equations to cartesian coordinates, the following are obtained:

$$\bar{E}(x,y,z) = j\frac{e^{-jkR}}{2\pi r}\left[\hat{x}f_x\cos\theta + \hat{y}f_y\cos\theta - \hat{z}\sin\theta\left(f_x\cos\phi + f_y\sin\phi\right)\right] \tag{A-6}$$

$$\begin{aligned} f_x &= \int_{-\infty}^{\infty}\int_{-\infty}^{\infty} E_{a\xi}(\xi,\eta)e^{j\frac{k}{r}(x\xi+y\eta)}d\xi d\eta \\ f_y &= \int_{-\infty}^{\infty}\int_{-\infty}^{\infty} E_{a\eta}(\xi,\eta)e^{j\frac{k}{r}(x\xi+y\eta)}d\xi d\eta\,. \end{aligned} \tag{A-7}$$

Note that the z component of the far-field is coupled to both the ξ and η components of the aperture field, but that the x and y components are separable; that is, they only rely on the ξ and η aperture components, respectively.

Assuming that the observation point is close to boresight (small θ), the following approximations are made:

$$\cos\theta \approx 1 \qquad \text{and} \qquad \sin\theta \approx \theta\,.$$

As a result, the z component is neglected ($\sin\theta \approx 0$) because the others will dominate. Since the remaining x and y components are separable, only one scalar equation remains:

$$E(x,y,z) \approx j\frac{ke^{-jkr}}{2\pi r}\left[\int_{-\infty}^{\infty}\int_{-\infty}^{\infty} E_a(\xi,\eta)e^{j\frac{k}{r}(x\xi+y\eta)}d\xi d\eta\right], \tag{A-8}$$

where E_a now represents either the ξ or the η component of the aperture field. This equation predicts the far-fields on a spherical surface of radius r. The comparison between this result and Fourier Optics can only be made if the former is projected onto a plane that is perpendicular to the z axis. Near boresight, $r \approx z$ and by substituting k with $2\pi/\lambda$, the following is obtained :

$$E(x,y,z) \approx j\frac{e^{-jkz}}{\lambda z}\int_{-\infty}^{\infty}\int_{-\infty}^{\infty} E_a(\xi,\eta)e^{j\frac{2\pi}{\lambda z}(x\xi+y\eta)}d\xi d\eta\,. \tag{A-9}$$

Using the paraxial phase approximation (see Appendix C) to project from the spherical surface to the plane, the following equation results:

$$E(x,y,z) \approx j\frac{e^{-jkz}e^{-j\frac{k}{2z}(x^2+y^2)}}{\lambda z}\int_{-\infty}^{\infty}\int_{-\infty}^{\infty} E_a(\xi,\eta)e^{j\frac{2\pi}{\lambda z}(x\xi+y\eta)}d\xi d\eta\,. \tag{A-10}$$

The comparison of Equation (A-10) with the Fourier Optics Equation (A-1) shows that they are equivalent except for the sign of the phases. Goodman [61] uses a negative phase convention for the temporal dependence $e^{-j\omega t}$ (clockwise phasor), while Balanis [57] uses a positive phase $e^{j\omega t}$ (counter-clockwise phasor), and hence this discrepancy is easily explained. Therefore, the far-field Fourier Optics propagator is a special case of the far-field Spectral Domain Method. However, they are only equivalent near the far-field boresight, where the problem reduces to a scalar one.

9. Appendix B: Physical Optics Derivations

9.1 Appendix B.1

A more general form of equations (4-2) and (4-3) are given below:

$$\underline{G_2}(\bar{r},\bar{r}') = -\frac{1}{j\omega\mu}\bar{\nabla}\times\underline{G_1}(\bar{r},\bar{r}') \tag{B-1}$$

$$j\omega\varepsilon\underline{G_1}(\bar{r},\bar{r}') - \bar{\nabla}\times\underline{G_2}(\bar{r},\bar{r}') = \underline{1}\,\delta(\bar{r}-\bar{r}')\,. \tag{B-2}$$

By substituting Equation (B-1) into Equation (B-2), and by using the dyadic identity

$$\bar{\nabla}\times\bar{\nabla}\times\underline{A} = \bar{\nabla}\bar{\nabla}\cdot\underline{A} - \bar{\nabla}^2\underline{A}\,,$$

the following equation is obtained:

$$j\omega\varepsilon\underline{G_1}(\bar{r},\bar{r}') + \frac{1}{j\omega\mu}\left[\bar{\nabla}\bar{\nabla}\cdot\underline{G_1}(\bar{r},\bar{r}') - \bar{\nabla}^2\underline{G_1}(\bar{r},\bar{r}')\right] = \underline{1}\,\delta(\bar{r}-\bar{r}')\,. \tag{B-3}$$

The proof is completed by multiplying Equation (B-3) by $j\omega\varepsilon$ and by substituting $\omega^2\varepsilon\mu = k^2$:

$$\bar{\nabla}\bar{\nabla}\cdot\underline{G_1}(\bar{r},\bar{r}') - \bar{\nabla}^2\underline{G_1}(\bar{r},\bar{r}') - k^2\underline{G_1}(\bar{r},\bar{r}') = j\omega\mu\underline{1}\,\delta(\bar{r}-\bar{r}')\,.$$

Q.E.D. (B.1)

9.2 Appendix B.2

The four dyadic free-space Green's functions will now be derived. The electric-electric Green's function of Equation (4-10) is written below:

$$\underline{G_{EJ}}(\bar{R}) = -j\omega\mu\left(\underline{1} + \frac{\bar{\nabla}\bar{\nabla}}{k^2}\right)g(R)\,. \tag{B-4}$$

Note that the term $\left(\underline{1} + \frac{\bar{\nabla}\bar{\nabla}}{k^2}\right)$ is a dyadic, therefore $\bar{\nabla}\bar{\nabla}g(R)$ must also be a dyadic. The term $\bar{\nabla}g(R)$ is the gradient of the scalar function $g(R)$. Using spherical coordinates centered at the source point $\bar{r}'$, the gradient is:

$$\begin{aligned}
\bar{\nabla} g(R) &= \frac{\partial g(R)}{\partial R}\hat{R} + \frac{1}{R}\frac{\partial g(R)}{\partial \theta}\hat{\theta} + \frac{1}{R\sin\theta}\frac{\partial g(R)}{\partial \phi}\hat{\phi} \\
&= \frac{\partial g(R)}{\partial R}\hat{R} \\
&= \frac{-jke^{-jkR}(4\pi R) - 4\pi e^{-jkR}}{(4\pi R)^2}\hat{R} \\
&= -\hat{R}\left(jk + \frac{1}{R}\right)\frac{e^{-jkR}}{4\pi R} \\
&= -\hat{R}\left(jk + \frac{1}{R}\right)g(R) \\
&= -\left(jk + \frac{1}{R}\right)g(R)\begin{bmatrix} R_{ux} & R_{uy} & R_{uz} \end{bmatrix}
\end{aligned} \tag{B-5}$$

Where the unit radial vector from the source point to the observation point is $\hat{R} = \frac{\bar{R}}{|\bar{R}|} = \begin{bmatrix} R_{ux} & R_{uy} & R_{uz} \end{bmatrix}$. The directors of this unit vector are the following:

$$R_{ux} = \frac{x - x'}{R}, \quad R_{uy} = \frac{y - y'}{R}, \quad \text{and} \quad R_{uz} = \frac{z - z'}{R},$$

where the observation point is $\bar{r} = (x, y, z)$, the source point is $\bar{r}' = (x', y', z')$, and the distance between these two points is $R = |\bar{R}| = |\bar{r} - \bar{r}'| = \sqrt{(x - x')^2 + (y - y')^2 + (z - z')^2}$. Returning to the derivation, the dyadic $\bar{\nabla}\bar{\nabla} g(R)$ is expressed as:

$$\begin{aligned}
\bar{\nabla}\bar{\nabla} g(R) &= \begin{bmatrix} \partial/\partial x \\ \partial/\partial y \\ \partial/\partial z \end{bmatrix}\left(-\left(\frac{1}{R} + jk\right)g(R)\begin{bmatrix} R_{ux} & R_{uy} & R_{uz} \end{bmatrix}\right) \\
&= \begin{bmatrix} \frac{\partial}{\partial x}\left(-\frac{1}{R} - jk\right)g(R)R_{ux} & \frac{\partial}{\partial x}\left(-\frac{1}{R} - jk\right)g(R)R_{uy} & \frac{\partial}{\partial x}\left(-\frac{1}{R} - jk\right)g(R)R_{uz} \\ \frac{\partial}{\partial y}\left(-\frac{1}{R} - jk\right)g(R)R_{ux} & \frac{\partial}{\partial y}\left(-\frac{1}{R} - jk\right)g(R)R_{uy} & \frac{\partial}{\partial y}\left(-\frac{1}{R} - jk\right)g(R)R_{uz} \\ \frac{\partial}{\partial z}\left(-\frac{1}{R} - jk\right)g(R)R_{ux} & \frac{\partial}{\partial z}\left(-\frac{1}{R} - jk\right)g(R)R_{uy} & \frac{\partial}{\partial z}\left(-\frac{1}{R} - jk\right)g(R)R_{uz} \end{bmatrix}.
\end{aligned} \tag{B-6}$$

The (1,1) matrix element is expanded on the line below.

$$-\frac{\partial}{\partial x}\left\{\left(\tfrac{1}{R}+jk\right)g(R)R_{ux}\right\}=-\frac{\partial}{\partial x}\begin{Bmatrix}\left(\left[(x-x')^2+(y-y')^2+(z-z')^2\right]^{-\frac{1}{2}}+jk\right)\cdot\ (\ldots)\\ (\ldots)\ \dfrac{e^{-jk\left((x-x')^2+(y-y')^2+(z-z')^2\right)^{\frac{1}{2}}}(x-x')}{4\pi\left((x-x')^2+(y-y')^2+(z-z')^2\right)}\end{Bmatrix} \qquad \textbf{(B-7)}$$

Here the ellipsis (...) indicates that the multiplication continues on the line below. Note that a partial derivative of a sum of two terms is required. Taking the partial derivative of the first term then,

$$\frac{-1}{4\pi}\frac{\partial}{\partial x}\left\{\frac{e^{-jk\left((x-x')^2+(y-y')^2+(z-z')^2\right)^{\frac{1}{2}}}(x-x')}{\left((x-x')^2+(y-y')^2+(z-z')^2\right)^{\frac{1}{2}}}\right\}$$

$$=\frac{-1}{4\pi}\left\{\frac{\left[-jk\left(\frac{1}{2}\right)R^{-1}(2)(x-x')e^{-jkR}(x-x')+e^{-jkR}\right]R^3-(x-x')e^{-jkR}\left(\frac{3}{2}\right)R(2)(x-x')}{R^6}\right\}$$

$$=\frac{-e^{-jkR}}{4\pi R}\left\{\frac{-jkR^2(x-x')(x-x')+R^3-3R(x-x')(x-x')}{R^5}\right\}$$

$$=g(R)\left\{\frac{jkR_{ux}R_{ux}}{R^3}-\frac{1}{R^2}+\frac{3R_{ux}R_{ux}}{R^2}\right\}.$$

The partial derivative of the second term of Equation (B-7) is:

$$-\frac{\partial}{\partial x}\left\{\frac{jke^{-jk\left((x-x')^2+(y-y')^2+(z-z')^2\right)^{\frac{1}{2}}}(x-x')}{4\pi\left((x-x')^2+(y-y')^2+(z-z')^2\right)}\right\}$$

$$=\frac{-1}{4\pi}\left\{\frac{\left[k^2\left(\frac{1}{2}\right)R^{-1}e^{-jkR}(2)(x-x')(x-x')+jke^{-jkR}\right]R^2-(x-x')jke^{-jkR}(2)(x-x')}{R^4}\right\}$$

$$=\frac{e^{-jkR}}{4\pi R}\left\{\frac{-k^2R(x-x')(x-x')-jkR^2+2jk(x-x')(x-x')}{R^3}\right\}$$

$$=g(R)\left\{-k^2R_{ux}R_{ux}-\frac{jk}{R}+\frac{2jkR_{ux}R_{ux}}{R}\right\}.$$

The sum of these two partial derivatives yields the (1,1) element of the matrix in Equation (B-6):

$$
\begin{aligned}
(1,1) \quad &= g(R)\left\{\frac{jkR_{ux}R_{ux}}{R}-\frac{1}{R^2}+\frac{2R_{ux}R_{ux}}{R^2}-k^2R_{ux}R_{ux}-\frac{jk}{R}+\frac{2jkR_{ux}R_{ux}}{R}\right\} \\
&= -\left(\frac{1}{R}+jk\right)\frac{g(R)}{R}\left[1-R_{ux}{}^2\right]+g(R)\left\{\frac{2R_{ux}R_{ux}}{R^2}-k^2R_{ux}R_{ux}+\frac{2jkR_{ux}R_{ux}}{R}\right\} \\
&= -\left(\frac{1}{R}+jk\right)\frac{g(R)}{R}\left[1-R_{ux}{}^2\right]+g(R)R_{ux}R_{ux}\left\{\frac{2}{R^2}+\frac{2jk}{R}-k^2\right\} \\
&= -\left(\frac{1}{R}+jk\right)\frac{g(R)}{R}\left[1-R_{ux}{}^2\right]+g(R)R_{ux}R_{ux}\left\{\frac{1}{R^2}+\left(\frac{1}{R^2}+\frac{2jk}{R}-k^2\right)\right\} \\
&= -\left(\frac{1}{R}+jk\right)\frac{g(R)}{R}\left[1-R_{ux}{}^2\right]+g(R)R_{ux}R_{ux}\left\{\frac{1}{R^2}+\left(\frac{1}{R}+jk\right)^2\right\}.
\end{aligned}
$$

The remaining two diagonal elements of the matrix in Equation (B-6) reduce to the same equation, except that R_{ux} is replaced by either R_{uy} or R_{uz}. The other non-diagonal terms of the matrix in Equation (B-6) all share the same general form. Consider the (2,3) element:

$$
\begin{aligned}
-\frac{\partial}{\partial y}\left\{\left(\frac{1}{R}+jk\right)g(R)R_{uz}\right\} &= \frac{-1}{4\pi}\frac{\partial}{\partial y}\left(\frac{e^{-jk\left[(x-x')^2+(y-y')^2+(z-z')^2\right]^{\frac{1}{2}}}(z-z')}{\left[(x-x')^2+(y-y')^2+(z-z')^2\right]^{\frac{3}{2}}}\right)\cdots \\
&\cdots-\frac{-1}{4\pi}\frac{\partial}{\partial y}\left(\frac{jke^{-jk\left[(x-x')^2+(y-y')^2+(z-z')^2\right]^{\frac{1}{2}}}(z-z')}{\left[(x-x')^2+(y-y')^2+(z-z')^2\right]}\right) \\
&= \frac{-1}{4\pi}\left\{\frac{-jk(z-z')R^{-1}(y-y')e^{-jkR}R^3-(z-z')e^{-jkR}(3)(y-y')R}{R^6}\right\}\cdots \\
&\quad\cdots-\left(\frac{1}{4\pi}\right)\left\{\frac{k^2(z-z')(y-y')e^{-jkR}R^{-1}R^2-(z-z')jke^{-jkR}(2)(y-y')}{R^4}\right\} \\
&= \frac{e^{-jkR}}{4\pi R}\left\{\frac{jkR^2(y-y')(z-z')+3R(y-y')(z-z')}{R^5}\right\}\cdots \\
&\quad\cdots+\frac{e^{-jkR}}{4\pi R}\left\{\frac{-k^2R(y-y')(z-z')+2jk(y-y')(z-z')}{R^3}\right\}
\end{aligned}
$$

(cont...)

(cont...)

$$-\frac{\partial}{\partial y}\left\{\left(\frac{1}{R}+jk\right)g(R)R_{uz}\right\} = g(R)\left\{\frac{jkR_{uy}R_{uz}}{R}+\frac{3R_{uy}R_{uz}}{R^2}\right\}+g(R)\left\{-k^2R_{uy}R_{uz}+\frac{2jkR_{uy}R_{uz}}{R}\right\}$$
$$=-\left(\frac{1}{R}+jk\right)\frac{g(R)}{R}\left[-R_{uy}R_{uz}\right]+g(R)R_{uy}R_{uz}\left(\frac{2}{R^2}+\frac{2jk}{R}-k^2\right)$$
$$=-\left(\frac{1}{R}+jk\right)\frac{g(R)}{R}\left[-R_{uy}R_{uz}\right]+g(R)R_{uy}R_{uz}\left(\frac{1}{R^2}+\left(\frac{1}{R}+jk\right)^2\right).$$

All of the other non-diagonal elements reduce to similar expressions, differing only by the R_{mn} terms. Grouping all of the matrix elements of Equation (B-6), the following matrix equation results:

$$\bar{\nabla}\bar{\nabla}g(R) = g(R)\left(\frac{1}{R^2}+\left(\frac{1}{R}+jk\right)^2\right)\begin{bmatrix} R_{ux}\left[R_{ux} & R_{uy} & R_{uz}\right] \\ R_{uy}\left[R_{ux} & R_{uy} & R_{uz}\right] \\ R_{uz}\left[R_{ux} & R_{uy} & R_{uz}\right] \end{bmatrix}-\left(\frac{1}{R}+jk\right)\frac{g(R)}{R}\begin{bmatrix} 1-R_{ux}^2 & -R_{uy}R_{ux} & -R_{uz}R_{ux} \\ -R_{ux}R_{uy} & 1-R_{uy}^2 & -R_{uz}R_{uy} \\ -R_{ux}R_{uz} & -R_{uy}R_{uz} & 1-R_{uz}^2 \end{bmatrix}$$
$$=\frac{g(R)}{R^2}\underline{\hat{R}\hat{R}}+g(R)\left(\frac{1}{R}+jk\right)^2\underline{\hat{R}\hat{R}}-\frac{g(R)}{R}\left(\frac{1}{R}+jk\right)\left(\underline{1}-\underline{\hat{R}\hat{R}}\right)$$
$$=g(R)\underline{\hat{R}\hat{R}}\left(\frac{2}{R^2}+j\frac{2k}{R}-k^2\right)-g(R)\left(\underline{1}-\underline{\hat{R}\hat{R}}\right)\left(\frac{1}{R^2}+j\frac{k}{R}\right). \qquad \textbf{(B-8)}$$

The $\underline{\hat{R}\hat{R}}$ term is defined as:

$$\underline{\hat{R}\hat{R}}=\begin{bmatrix} R_{ux}^2 & R_{ux}R_{uy} & R_{ux}R_{uz} \\ R_{uy}R_{ux} & R_{uy}^2 & R_{uy}R_{uz} \\ R_{uz}R_{ux} & R_{uz}R_{uy} & R_{uz}^2 \end{bmatrix}. \qquad \textbf{(B-9)}$$

The differential operators in the term $\bar{\nabla}\bar{\nabla}g(R)$ have been eliminated, making it a purely analytical expression. By substituting the last line of Equation (B-8) into Equation (4-10), the complete electric-electric free-space Green's function is obtained:

$$\underline{G_{EJ}}(\bar{R}) = j\omega\mu\frac{e^{-jkR}}{4\pi R}\left[\underline{1}+\frac{\underline{\hat{R}\hat{R}}\left(\frac{2}{R^2}+j\frac{2k}{R}-k^2\right)-\left(\underline{1}-\underline{\hat{R}\hat{R}}\right)\left(\frac{1}{R^2}+j\frac{k}{R}\right)}{k^2}\right]$$
$$=j\omega\mu\frac{e^{-jkR}}{4\pi R}\left[\left(\underline{1}-\underline{\hat{R}\hat{R}}\right)\left(\underline{1}-\frac{1}{k^2R^2}-j\frac{1}{kR}\right)+\underline{\hat{R}\hat{R}}\left(\frac{2}{k^2R^2}+j\frac{2}{kR}\right)\right]$$

Q.E.D. (G_{EJ})

Equation (4-10) indicates that the magnetic-magnetic Green's function differs from the electric-electric Green's function by a constant, therefore:

$$\underline{G_{HM}}(\bar{R}) = j\omega\varepsilon\frac{e^{-jkR}}{4\pi R}\left[\left(\underline{1}-\underline{\hat{R}\hat{R}}\right)\left(\underline{1}-\frac{1}{k^2R^2}-j\frac{1}{kR}\right)+\underline{\hat{R}\hat{R}}\left(\frac{2}{k^2R^2}+j\frac{2}{kR}\right)\right].$$

Q.E.D. (G_{HM})

The magnetic-electric Green's function is found from its relation to the electric-electric Green's function, given in Equation (4-3):

$$\underline{G_{HJ}}(\bar{R}) = \frac{-1}{j\omega\mu}\bar{\nabla}\times\underline{G_{EJ}}(\bar{R})$$

$$= -\bar{\nabla}\times\left(\underline{1}\,g(R)+\frac{\bar{\nabla}\bar{\nabla}}{k^2}g(R)\right) \qquad \rightarrow \bar{\nabla}\times\bar{\nabla}\bar{\nabla}A \equiv 0, \text{ therefore,}$$

$$= -\bar{\nabla}\times\left(\underline{1}\,g(R)\right) \qquad \rightarrow \bar{\nabla}\times(\varphi\underline{A}) \equiv \bar{\nabla}\varphi\times\underline{A}+\varphi\bar{\nabla}\times\underline{A} \text{ for any scalar } \varphi, \text{ therefore,}$$

$$= -\left(\bar{\nabla}g(R)\right)\times\underline{1}-g(R)\bar{\nabla}\times\underline{1} \qquad \rightarrow \bar{\nabla}\times\underline{1} \equiv 0, \text{ therefore,}$$

$$= -\left(\bar{\nabla}g(R)\right)\times\underline{1} \qquad \rightarrow \left(\bar{\nabla}g(R)\right) \text{ was calculated in equation (B- 5); substituting,}$$

$$= \left(\frac{1}{R}+jk\right)\frac{e^{-jkR}}{4\pi R}\hat{R}\times\underline{1}\ .$$

Q.E.D. (G_{HJ})

The same development for the electric-magnetic Green's function yields the following expression:

$$\underline{G_{EM}}(\bar{R}) = -\left(\frac{1}{R}+jk\right)\frac{e^{-jkR}}{4\pi R}\hat{R}\times\underline{1}. \qquad \textbf{Q.E.D. } (G_{EM})$$

This concludes the derivations in Appendix B.

10. Appendix C: Paraxial Approximation of the Far-Field

The distance that is commonly quoted as the inner boundary of an antenna's far-field region is given by $2D^2/\lambda$, where D is the largest dimension of the antenna. This term originates from a Geometrical Optics paraxial approximation originally derived for aperture antennas. In the far-field, the spherical waves originating from a point source are approximated by plane waves. Theoretically, this requires the distance from the source to be infinite. However, a maximum phase-error along the length of the antenna of $\pi/8$ radians between the spherical and the plane wave approximation is generally accepted. The $2D^2/\lambda$ distance criterion is now derived.

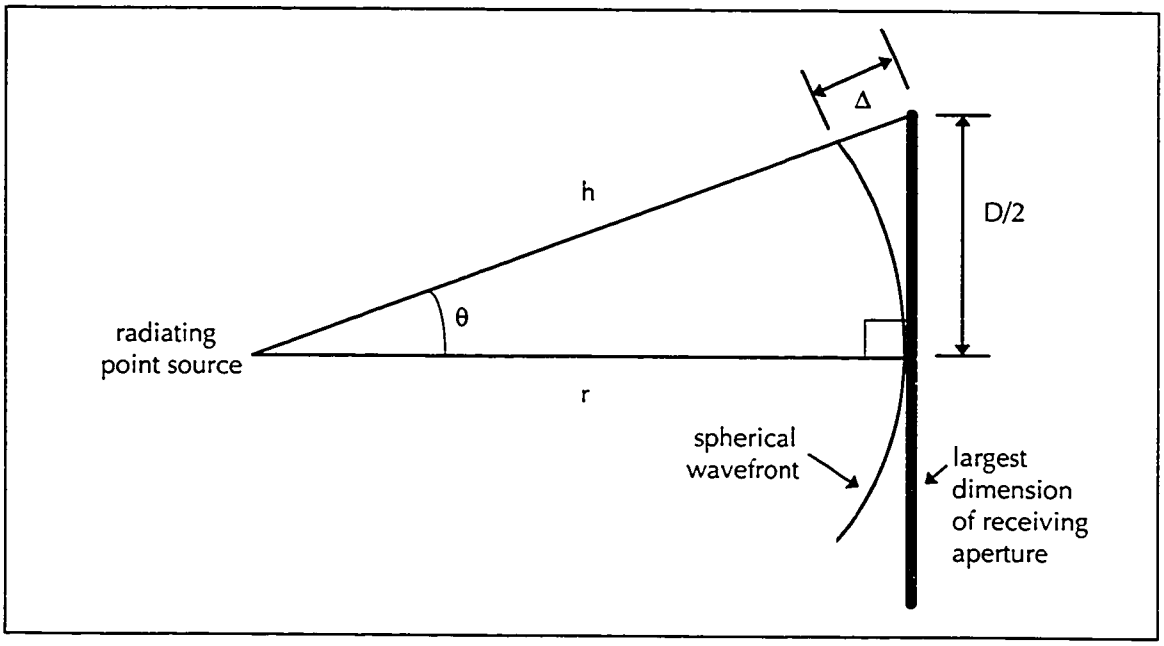

Figure 86: Far-field Approximation Geometry

A spherical wave obeying the scalar free-space Green's function can be expressed as $\varphi(r) = A\frac{e^{-jkr}}{r}$, where A is the amplitude, k is the phase constant and r is the radial distance away from the source point. Referring to Figure 86, the phase difference between a ray that is incident on the middle of the receiving antenna and a ray that is incident on the edge of the antenna is therefore $k\Delta = k(h-r)$, where h is the hypotenuse formed by the right-angled triangle with sides $D/2$ and r.

The length of the hypotenuse is:

$$h = \sqrt{r^2 + \frac{D^2}{4}} = r\sqrt{1 + \frac{D^2}{4r^2}}. \qquad \textbf{(C-1)}$$

The binomial expansion is used to evaluate the square root:

$$(1+x)^k = \sum_{n=0}^{\infty} \binom{k}{n} x^n = 1 + kx + \frac{k(k-1)}{2!}x^2 + \frac{k(k-1)(k-2)}{3!}x^3 + \ldots. \qquad \textbf{(C-2)}$$

Assuming that $D^2 << 4r^2$, which is equivalent to restricting the angle θ to being close to boresight, all of the terms of the expansion may be omitted except for the first two. The remaining expression is referred to as the *paraxial approximation*:

$$h \approx r\left(1 + \frac{1}{2}\frac{D^2}{4r^2}\right) = r + \frac{D^2}{8r}. \qquad \textbf{(C-3)}$$

The phase difference therefore becomes:

$$k\Delta = k(h - r) \approx k\left(r + \frac{D^2}{8r} - r\right) = \frac{kD^2}{8r} \quad [rads]. \qquad \textbf{(C-4)}$$

Enforcing the commonly accepted (yet arbitrary) error of $\pi/8$ radians yields the required distance to the far-field boundary:

$$\frac{kD^2}{8r} \le \frac{\pi}{8} \qquad \text{or} \qquad r \ge \frac{2D^2}{\lambda},$$

where k has been substituted by $2\pi/\lambda$.

The IEEE standard definition of the far-field states that the $2D^2/\lambda$ distance applies only if the antenna's maximum dimension D is large compared to a wavelength [84]. This has been verified experimentally in [85]. Indeed, diffraction effects become prominent when the antenna is not large compared to a wavelength, introducing additional phase errors that are not predicted by the simple spherical wave.

Therefore, defining the distance to the far-field becomes very difficult for slot antennas, since these apertures are typically much smaller than several wavelengths.

Regarding the application of this formula to non-aperture antennas [86]:

> *"Non-aperture antennas behave in a different way and no simple formulae can be derived to define the far-field distance. However, in practice the $2D^2/\lambda$ distance tends to give a conservative estimate of distance so this is widely used as a criteria for all antennas".*

As the distance to the antenna is reduced, the following near-field effects are observed [87]:

> *"Reducing the distance* [...] *tends to give broader radiation patterns, higher minor lobes and shallower nulls between lobes...".*

The IEEE standard definition of the far-field distance, in the strict sense, applies to very few antennas and even then should only be considered as a rule of thumb. As for its application to the slot antennas in this thesis, the formula cannot be confidently used to determine whether the dielectric-to-air interface of a lens is in the slot's far-field.

11. Appendix D: Shifting the Impedance Reference Plane

The signal flow graph of a cascaded two-port and of a one-port network is illustrated in Figure 87.

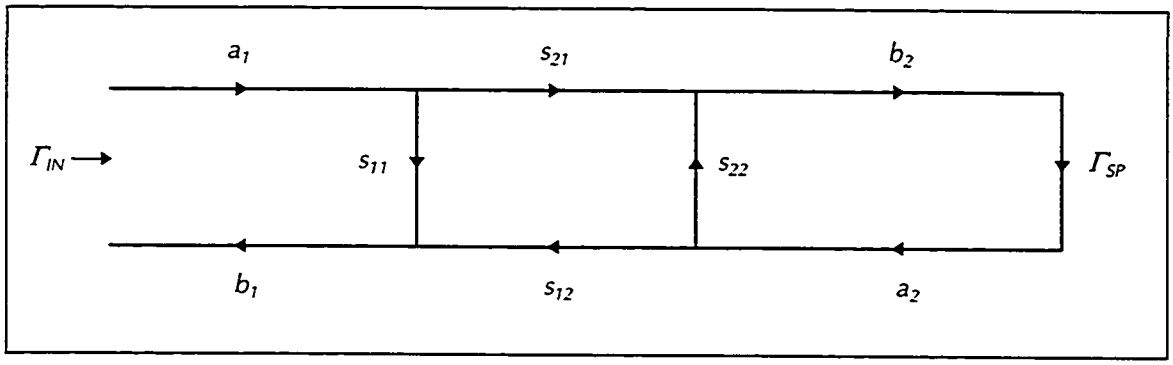

Figure 87: Cascaded Two-Port and One-Port

If all of the parameters except Γ_{SP} are known, the latter may be isolated by using the development below.

$$a_2 = \Gamma_{SP} b_2 \qquad \textbf{(E-1)}$$

$$b_2 = s_{21}a_1 + s_{22}a_2$$
$$b_2 = s_{21}a_1 + s_{22}\Gamma_{SP}b_2 \quad \text{(substitution of (E-1))}$$
$$\therefore b_2 = \frac{s_{21}a_1}{1 - s_{22}\Gamma_{SP}} \qquad \textbf{(E-2)}$$

$$\therefore a_2 = \frac{\Gamma_{SP}s_{21}a_1}{1 - s_{22}\Gamma_{SP}} \quad \text{(substitution of (E-2) into (E-1))} \qquad \textbf{(E-3)}$$

$$b_1 = s_{11}a_1 + s_{12}a_2$$
$$\therefore b_1 = s_{11}a_1 + s_{12}\left(\frac{\Gamma_{SP}s_{21}a_1}{1 - s_{22}\Gamma_{SP}}\right) \quad \text{(substitution of (E-3))} \qquad \textbf{(E-4)}$$

$$\Gamma_{IN} = \frac{b_1}{a_1} = s_{11} + \frac{\Gamma_{SP}s_{12}s_{21}}{1 - s_{22}\Gamma_{SP}} \quad \text{(substitution of (E-4))}$$
$$\therefore \Gamma_{SP} = \frac{\Gamma_{IN} - s_{11}}{s_{12}s_{21} + s_{22}\Gamma_{IN} - s_{11}s_{22}} \qquad \textbf{Q.E.D.}$$

12. References

1. G.M. Rebeiz, "Millimeter-Wave and Terahertz Integrated Circuit Antennas", *Proc. IEEE*, **80**, no. 11, November 1992, pp. 1748-1770.

2. D.B. Rutledge, D.P. Neikirk, and D.P. Kasilingam, "Integrated Circuit Antennas", Infrared and Millimeter Waves, **10**, chap. 1, K.J. Button (Ed.), New York: Academic Press, 1983, pp. 1-90.

3. M. Kominami, D.M. Pozar, and D.H. Schaubert, "Dipole and Slot Elements and Arrays on Semi-Infinite Substrates", *IEEE Trans. Antennas Propagat.*, **AP-33**, no. 6, June 1985, pp. 600-607.

4. N.G. Alexopoulos, P.B. Katehi, and D.B. Rutledge, "Substrate Optimization for Integrated Circuit Antennas", *IEEE Trans. Microwave Theory Tech.*, **MTT-31**, no. 7, July 1983, pp. 550-557.

5. D.M. Pozar, "Considerations for Millimeter Wave Printed Antennas", *IEEE Trans. Antennas Propagat.*, **AP-31**, no. 5, September 1983, pp. 740-747.

6. P.B. Katehi and N.G. Alexopoulos, "On the Effect of Substrate Thickness and Permittivity on Printed Circuit Dipole Properties", *IEEE Trans. Antennas Propagat.*, **AP-31**, no. 1, January 1983, pp. 34-39.

7. L.J.P. Roy, "Integrated Amplifier / Antenna Elements for GaAs Monolithic Phased Arrays", Ph.D. thesis, Ottawa Carleton Institute for Electrical Engineering, Carleton Univ., Ottawa, Canada, June 1993.

8. C.R. Brewitt-Taylor, D.J. Gunton, and H.D. Rees, "Planar Antennas on a Dielectric Surface", *Electron. Lett.*, **17**, no. 20, October 1981, pp. 729-731.

9. G.V. Eleftheriades and G.M. Rebeiz, "Self and Mutual Admittance of Slot Antennas on a Dielectric Half-Space", *Int. J. Infrared and Millimeter Waves*, **14**, no. 10, 1983, pp. 1925-1946.

10. T.M. Weller, L.P.B. Katehi, and G.M. Rebeiz, "Single and Double Folded-Slot Antennas on Semi-Infinite Substrates", *IEEE Trans. Antennas Propagat.*, **AP-43**, no. 12, December 1995, pp. 1423-1248.

11. M.N. Afsar and K.J. Button, "Millimeter-Wave Dielectric Properties of Materials", Infrared and Millimeter Waves, **12**, chap. 1, New York: Academic Press, 1983, pp. 1-42.

12. C. Zah and D.B. Rutledge, "A Polystyrene Cap for Matching a Silicon Lens at Millimeter Wavelengths", *Int. J. of Infrared and Millimeter Waves*, **6**, no. 9, 1985, pp. 909-917.

13. D.F. Filipovic, S.S. Gearhart, and G.M. Rebeiz, "Double-Slot Antennas on Extended Hemispherical and Elliptical Silicon Dielectric Lenses", *IEEE Trans. Microwave Theory Tech.*, **MTT-41**, no. 10, October 1993, pp. 1738-1749.

14. S.S. Gearhart and G.M. Rebeiz, "A Monolithic 250 GHz Schottky-Diode Receiver", *IEEE Trans. Microwave Theory Tech.*, **MTT-42**, no. 12, December 1994, pp. 2504-2511.

15. K. Mizuno *et al.*, "Yagi-Uda Array for Millimetre-Wave Imaging", *Electron. Lett.*, **27**, no. 2, January 1991, pp. 108-109.

16. K. Uehara *et al.*, "Lens-Coupled Imaging Arrays for the Millimeter- and Submillimeter-Wave Regions", *IEEE Trans. Microwave Theory Tech.*, **MTT-40**, no. 5, May 1992, pp. 806-811.

17. K. Watabe *et al.*, "Millimeter-Wave Imaging Using Neural Networks for Object Recognition", *IEEE-MTT Int. Microwave Symp. Dig.*, pp. 1135-1138.

18. S.K. Masarweh *et al.*, "Modeling of a Monolithic Slot Ring Quasi-Optical Mixer", *IEEE Trans. Microwave Theory Tech.*, **MTT-42**, no. 9, September 1994, pp. 1602-1609.

19. M.J. Wengler *et al.*, "A Low Noise Receiver for Millimeter and Submillimeter Wavelengths", *Int. J. Infrared and Millimeter Waves*, **6**, no. 8, 1985, pp. 697-706.

20. J. Zmuidzinas and H.G. LeDuc, "Quasi-Optical Slot Antenna SIS Mixers", *IEEE Trans. Microwave Theory Tech.*, **MTT-40**, no. 9, September 1992, pp. 1797-1804.

21. A. Skalare, T. de Graauw, and H. van de Stadt, "A Planar Dipole Array Antenna with an Elliptical Lens", *Microwave and Opt. Tech. Lett.*, **4**, no. 1, January 1991, John Wiley & Sons, Inc., pp. 9-12.

22. C.J. Alder *et al.*, "Microwave and Millimetre-Wave Receivers with Integral Antenna", *Proc. Inst. Elec. Eng.*, Pt. H, **138**, no. 3, June 1991, pp. 253-257.

23. T.H. Büttgenbach, "An Improved Solution for Integrated Array Optics in Quasi-Optical mm and Submm Receivers: the Hybrid Antenna", *IEEE Trans. Microwave Theory Tech.*, **MTT-41**, no. 10, October 1993, 1750-1761.

24. D.F. Filipovic *et al.*, "Off-Axis Properties of Silicon and Quartz Dielectric Lens Antennas", *IEEE Trans. Microwave Theory Tech.*, **MTT-45**, no. 5, May 1997, pp. 760-766.

25. S. Raman and G.M. Rebeiz, "Single- and Dual-Polarised Millimeter-Wave Slot-Ring Antennas", *IEEE Trans. Antennas Propagat.*, **AP-44**, no. 11, November 1996, pp. 1438-1444.

26. D.P. Neikirk *et al.*, "Far-Infrared Imaging Antenna Arrays", *Appl. Phys. Lett.*, **40**, no. 3, February 1982, pp. 203-205.

27. D.B. Rutledge and M.S. Muha, "Imaging Antenna Arrays", *IEEE Trans. Antennas Propagat.*, **AP-30**, no. 4, July 1982, pp. 535-540.

28. D.P. Neikirk *et al.*, "Imaging Antenna Array at 119μm", *Appl. Phys. Lett.*, **41**, no. 4, August 1982, pp. 329-331.

29. P.P. Tong *et al.*, "Tracking Antenna Arrays for Near-Millimeter Waves", *IEEE Trans. Antennas Propagat.*, **AP-31**, no. 3, May 1983, pp. 512-515.

30. P.P. Tong *et al.*, "Imaging Polarimeter Arrays for Near-Millimeter Waves", *IEEE Trans. Microwave Theory Tech.*, **MTT-32**, no. 5, May 1984, pp. 507-512.

31. C. Zah *et al.*, "Millimeter Wave Monolithic Schottky Diode Imaging Arrays", *Int. J. Infrared and Millimeter Waves*, **6**, no. 10, 1985, pp. 981-997.

32. G. Gauthier *et al.*, "A Low-Noise 86-90 GHz Uniplanar Schottky-Receiver", *1993 IEEE-MTT Int. Microwave Symp. Dig.*, pp. 325-328.

33. S.S. Gearhart *et al.*, "A Wide-Band 760-GHz Planar Integrated Schottky Receiver", *IEEE Microwave Guided Wave Lett.*, **3**, no. 7, July 1993, pp. 205-207.

34. S. Mollenkopf, L.P.B. Katehi, and G.M. Rebeiz, "A Low-Cost 20-22 GHz MIC Active Receiver/Radiometer", *IEEE Trans. Microwave Theory Tech.*, **MTT-43**, no. 4, April 1995, pp. 989-993.

35. G.V. Eleftheriades *et al.*, "ALPSS: A Millimetre-Wave Aperture-Coupled Patch Antenna on a Substrate Lens", *Electron. Lett.*, **33**, no. 3, January 1997, pp. 169-170.

36. E. Hecht, Optics, second ed., Reading, MA: Addison-Wesley, 1987, pp. 129-131.

37. R.E. Collin, Foundations for Microwave Engineering, second ed., New York: McGraw-Hill, Inc., 1992, pp. 508-517.

38. D. Kajfez and P. Guillon (Eds.), Dielectric Resonators, Dedham, MA: Artech House, Inc., 1986.

39. S.A. Long, M.W. McAllister, and L.C. Shen, "The Resonant Cylindrical Dielectric Cavity Antenna", *IEEE Trans. Antennas Propagat*, **AP-31**, no. 3, May 1983, pp. 406-412.

40. R.A. Kranenburg and S.A. Long, "Microstrip Transmission Line Excitation of Dielectric Resonator Antennas", *Electron. Lett.*, **24**, no. 18, September 1988, pp. 1156-1157.

41. G.P. Junker, "Input Impedance of Aperture-Coupled Dielectric Resonator Antennas", *IEEE Trans. Antennas Propagat.*, **AP-44**, no. 5, May 1996, pp. 600-606.

42. J.T.H. St. Martin *et al.*, "Dielectric Resonator Antenna Using Aperture Coupling", *Electron. Lett.*, no. 24, November 1990, pp. 2015-2016.

43. R.K. Mongia, A. Ittipiboon, and M. Cuhaci, "Measurement of Radiation Efficiency of Dielectric Resonator Antennas", *IEEE Microwave Guided Lett.*, **4**, no. 3, March 1994, pp. 80-82.

44. A.A. Kishk *et al.*, "Slot Excitation of the Dielectric Disk Radiator", *IEEE Trans. Antennas Propagat.*, **AP-43**, no. 2, February 1995, pp. 198-201.

45. M.W. McAllister, S.A. Long, and G.L. Conway, "Rectangular Dielectric Resonator Antenna", *Electron. Lett.*, **19**, pp. 218-219.

46. A. Petosa *et al.*, " Active Phased Array of Dielectric Resonator Antennas", *IEEE Antennas Propagat. Soc. Int. Symp. 1997 Dig.*, **2**, pp. 690-693.

47. M.W. McAllister and S.A. Long, "Resonant Hemispherical Dielectric Antenna", *Electron. Lett.*, no. 16, August 1984, pp. 657-659.

48. A.A. Kishk, G. Zhou, and A.W. Glisson, "Analysis of Dielectric-Resonator Antenna with Emphasis on Hemispherical Structures", *IEEE Antennas Propagat. Magazine*, **36**, no. 2, April 1994, pp. 20-31.

49. K.W. Leung *et al.*, "Theory and Experiment of a Coaxial Probe Fed Hemispherical Dielectric Resonator Antenna", *IEEE Trans. Antennas Propagat.*, **AP-41**, no. 10, October 1993, pp. 1390-1398.

50. K.W. Leung *et al.*, "Input Impedance of Hemispherical Dielectric Resonator Antenna", *Electron. Lett.*, **27**, 1991, pp. 2259-2260.

51. K.W. Leung *et al.*, "Input Impedance of Aperture Coupled Hemispherical Dielectric Resonator Antenna", *Electron. Lett.*, **29**, no. 13, June 1993, pp. 1165-1167.

52. G.P. Junker, A.A. Kishk, and A.W. Glisson, "Numerical Analysis of Dielectric Resonator Antennas Excited in Quasi-TE-Modes", *Electron. Lett.*, **29**, no. 21, October 1993, pp. 1810-1811.

53. R.K. Mongia *et al.*, "A Half-Split Cylindrical Dielectric Resonator Antenna Using Slot-Coupling", *IEEE Microwave Guided Wave Lett.*, **3**, no. 2, February 1993, pp. 38-39.

54. D.M. Pozar, "A Reciprocity Method of Analysis for Printed Slot and Slot-Coupled Microstrip Antennas", *IEEE Trans. Antennas Propagat.*, **AP-34**, no. 12, December 1986, pp. 1439-1446.

55. K.W. Leung and K.M. Luk, "Moment Method Solution of Aperture-Coupled Hemispherical Dielectric Resonator Antenna", *IEEE Antennas Propagat. Soc. Int. Symp.*, **2**, 1994, pp. 752-755.

56. D.K. Cheng, Field and Wave Electromagnetics, second ed., Reading, Massachusetts: Addison-Wesley Publishing Company, 1989, pp. 411-415.

57. C.A. Balanis, Antenna Theory - Analysis and Design, second ed., New York: John Wiley & Sons, Inc., 1997.

58. P.F. Goldsmith, "Quasioptical Techniques Offer Advantages at Millimeter Frequencies", *Microwave Systems News*, **13**, no. 13, December 1983, pp. 65-84.

59. P.F. Goldsmith, "Quasi-Optical Techniques", *Proc. IEEE*, **80**, no. 11, November 1992, pp. 1729-1747.

60. T. Sherer, "A Quasi-Optical Monopulse Radar Receiver Using Slot-Ring Mixers and a Hyper-hemispherical Lens", M.Sc. thesis, Univ. Massachusetts, Amherst, USA, February 1992.

61. J. W. Goodman, Introduction to Fourier Optics, second ed., New York: The McGraw-Hill Companies, Inc., 1996.

62. L. Diaz and T. Milligan, Antenna Engineering Using Physical Optics - Practical CAD Techniques and Software, Boston MA: Artech House, Inc., 1996.

63. R.E. Collin, Antennas and Radiowave Propagation, New York: McGraw-Hill, Inc., 1985, p.175.

64. C.A. Balanis, Advanced Engineering Electromagnetics, New York: John Wiley & Sons, Inc., pp. 970-911.

65. C.-T. Tai, Dyadic Green's Functions in Electromagnetic Theory, chap. 4, Scranton, PA: The Intext Monograph Series in Electrical Engineering, Intext Educational Publishers, 1971.

66. J. Van Bladel, Electromagnetic Fields, appendix 3, New York: McGraw-Hill, 1960, pp. 507-511.

67. R.F. Harrington, Field Computation by Moment Methods, second ed., New York: IEEE PRESS Series on Electromagnetic Waves, The Institute of Electrical and Electronics Engineers, Inc., 1993.

68. G.P. Junker, A.A. Kishk, and A.W. Glisson, "Input Impedance of Dielectric Resonator Antennas Excited by a Coaxial Probe", *IEEE Trans. Antennas and Propagat.*, **AP-42**, no. 7, July 1994, pp. 960-966.

69. G.P. Junker, A.A. Kishk, and A.W. Glisson, "Input Impedance of an Aperture Coupled Dielectric Resonator Antenna", *IEEE Antennas Propagat. Soc. Int. Symp. Dig.*, **2**, 1994, pp. 748-751.

70. A.A. Kishk, H.A. Auda, and B.C. Ahn, "Accurate Prediction of Radiation Patterns of Dielectric Resonator Antennas", *Electron. Lett.*, **23**, no. 25, December 1987, pp. 1374-1375.

71. A.A. Kishk, H.A. Auda, and B.C. Ahn, "Radiation Characteristics of Cylindrical Dielectric Resonator Antennas with New Applications", *IEEE Antennas Propagat. Soc. Newsletter*, **31**, no. 1, February 1989, pp. 7-16.

72. D. Kasilingam and D. Rutledge, "Focusing Properties of Small Lenses", *Int. J. Infrared and Millimeter Waves*, **7**, no. 10, 1986, pp. 1631-1647.

73. S. Silver (Ed.), Microwave Antenna Theory and Design, **12**, The Massachusetts Institute of Technology Radiation Laboratory Series, New York: McGraw-Hill Book Company, Inc., 1949, pp. 139-143.

74. R.E. Collin, Antennas and Radiowave Propagation, New York: McGraw-Hill, Inc., 1985, pp.190-194.

75. Y. Yoshimura, "A Microstripline Slot Antenna", *IEEE Trans. Microwave Theory Tech.*, **MTT-20**, no. 11, November 1972, pp. 760-762.

76. B.N. Das and K.K. Joshi, "Impedance of a Radiating Slot in the Ground Plane of a Microstripline", *IEEE Trans. Antennas Propagat.*, **AP-30**, no. 5, September 1982, pp. 922-926.

77. D.M. Pozar and N.K. Das, "Comments on 'Impedance of a Radiating Slot in the Ground Plane of a Microstripline'", *IEEE Trans. Antennas Propagat.*, **AP-34**, no. 7, July 1986, pp. 958-959.

78. H-Y Yang and N.G. Alexópoulos, "A Dynamic Model for Microstrip-Slotline Transition and Related Structures", *IEEE Trans. Microwave Theory Tech.*, **MTT-36**, no. 2, February 1988, pp. 286-293.

79. M. Kahrizi, T.K. Sarkar, and Z.A. Maricevic, "Analysis of a Wide Radiating Slot in the Ground Plane of a Microstrip Line", *IEEE Trans. Microwave Theory Tech.*, **MTT-41**, no. 1, January 1993, pp. 29-37.

80. I.J. Bahl, S.S. Stuchly, and M.A. Stuchly, "New Microstrip Slot Radiator for Medical Applications", *Electron. Lett.*, **16**, no. 19, September 1980, pp. 731-732.

81. P.L. Sullivan and D.H. Schaubert, "Analysis of an Aperture Coupled Microstrip Antenna", *IEEE Trans. Antennas Propagat.*, **AP-34**, no. 8, August 1986, pp. 977-984.

82. R. Oostlander *et al.*, "Aperture Coupled Microstrip Antenna Element Design", *Electron. Lett.*, **26**, no. 4, February 1990, pp. 224-225.

83. C. Edwards, Foundations for Microstrip Circuit Design, second ed., Chichester, England: Wiley, 1992, p. 132.

84. IEEE Std. 145-1983, "IEEE Standard Definitions of Terms for Antennas", *IEEE Trans. Antennas Propagat.*, **AP-31**, no. 6, part II, November 1983.

85. E.V. Jull, "An Investigation of Near-Field Radiation Patterns Measured with Large Antennas", *IRE Trans. Antennas Propagat.*, **AP-10**, July 1962, pp. 363-369.

86. A.W. Rudge *et al.* (Eds.), The Handbook of Antenna Design, **1**, London, UK: Peter Peregrinus Ltd., 1982, p. 14.

87. H. Jasik (Ed.), Antenna Engineering Handbook, chap. 1, New York: McGraw-Hill Book Company, 1961, p. 15.